POLITECNICO DI MILANO

Facoltà di Ingegneria Industriale

Corso di Laurea Magistrale in Ingegneria Aeronautica

Modelling of liquid film cooling in a GOX/Kerosene rocket combustion chamber

Relatore: Prof. Luigi T. DE LUCA

Co-relatore: Prof. Oskar HAIDN

Tesi di Laurea di:

Matteo TROTTI
Matr. 750001

Anno Accademico 2011 - 2012

Acknowledgments

First of all I want to thank my parents, Elisa and Mauro, who allowed me to get to this point, helping and supporting me unconditionally. Thanks also to my brother, Pai, the wildlife photographer, to my aunt and uncle, Anto and Edo, who constantly support me, and to my granparents Paola, Rosa and Gaetano, who learned to use Skype to keep in contact with me.

A very special thanks goes to my girlfriend, Vale, whom I have only spent some rare but wonderful days with and who stand and support me during the six month I was away from home; how can I forget your amazing surprise??

Thanks also to my friends Fabio, Miki and Masche for their support and confidence that I could make it. A special thanks also to Lorenz, inseparable mate of fun and study.

I owe a special thanks to my tutor Christoph, who assisted and constantly suggested me during my thesis work ("don't panic, Matteo, don't panic"); and Mariella and Simona, who welcome and constantly help me: grazie!

Thanks to my relator, professor Luigi De Luca, and to professor Oskar Haidn, who allow me to carry out abroad my thesis work as I have always wanted.

Last but not least, thanks to my flatmates Sebastian, Stefan, Marita and Kellie whom I spent these month with; I had a lot of funny moments to remember: vielen Dank für alle! Klugscheißer! Spoon!

Sono le scelte che facciamo che dimostrano quello che siamo veramente, molto più delle nostre capacità.

Albus Silente
Harry Potter e la camera dei segreti

Contents

List of Figures

List of Tables

List of symbols

Latin letters

Symbol	Description	Unit
a	Thermal diffusivity	$\left[m^2/s\right]$
A	Area	$\left[m^2\right]$
c_p	Specific heat capacity	$\left[kJ/kgK\right]$
$c^\star$	Characteristic velocity	$\left[m/s\right]$
D	Diameter	$[m]$
h	Enthalpy	$\left[J/kg\right]$
$L^\star$	Characteristic length	$[m]$
$\dot{m}$	Mass flux	$\left[kg/s\right]$
M	Blowing rate	$[-]$
OF or O/F	Mixture ratio	$[-]$
pp	Perimeter	$[m]$
P	Pressure	$[Pa]$
q	Heat flux	$\left[W/m^2\right]$
r	Radius	$[m]$
R	Empirical recovery factor	$[-]$
s	film coolant thickness	$[m]$
T	Temperature	$[K]$

Greek letters

Symbol	Description	Unit
α	Heat transfer coefficient (HTC)	$\left[W/m^2K\right]$
γ	Ratio of specific heat	$[-]$
ε	Emissivity	$[-]$
ε_m	Eddy diffusivity	$[-]$
η	Dynamic viscosity	$\left[kg/ms\right]$
$\eta_{c^\star}$	Combustion efficiency	$[-]$
Θ or η	Film cooling effectiveness	$[-]$
λ	Thermal conductivity	$\left[W/mK\right]$
μ	Film cooling mass flow rate	$[\%]$
ρ	Density	$\left[kg/m^3\right]$
σ	Surface tension	$\left[mN/m\right]$
σ_S	Stefan-Boltzmann constant	$\left[W/m^2K^4\right]$
ψ	Stability effectiveness	$[-]$

Adimensional number

Symbol	Description
M	Mach number
Nu	Nusselt number
Pe	Peclet number
Pr	Prandtl number
Re	Reynolds number

Subscripts

Symbol	Description
0	Stagnation point
$\star$ or th	Throat
ad	Adiabatic
aw	Adiabatic wall
b	Bulk
c	Coolant
cc	Combustion chamber
crit	Value at critical point
e or $main$	Core flux
eff	Effective
F	Fuel
HG	Hot gas
HW	Hot wall
i or inj	Injection point
if	Interface
l	Liquid coolant
s, liq	Saturated liquid
M	Mean value
max	Maximum
nom	Nominal
OX	Oxidizer
r	Recovery
rad	Radiative
sat	Saturation
sv	Saturated vapor
t	Turbulent
th	Theoretical
tot	Total
v	Vapor
vap	Vaporization

Sommario

La tecnica del film cooling è un metodo ampiamente usato nel raffreddamento dei motori a razzo, sia da solo che in combinazione con altri metodi. Consiste nell'iniezione di un fluido vicino alle pareti della camera di combustione attraverso fori, fessure, iniettori o speciali applicatori. La struttura è protetta dall'impatto con i gas caldi, quindi la temperatura dei gas vicino alle pareti si riduce e di conseguenza si riducono anche i flussi termici. Il lavoro di tesi analizza questa tecnica paragonando risultati numerici a quelli sperimentali. Questi ultimi sono stati condotti alla camera di prova in scala ridotta del TUM, Technische Universität München, di Monaco di Baviera.

La tesi si concentra sull'implementazione di nuovi modelli per il film cooling e per il coefficiente di scambio termico, per adattare e verificare le attuali predizioni del codice Matlab Thermtest, sviluppato al TUM.

Nuovi modelli di film cooling e per il calcolo del coefficiente di scambio termico saranno implementati e confrontati con i risultati sperimentali per trovare quello che meglio prevede i flussi termici alle pareti. Una volta scelto uno tra i modelli esaminati, è stata eseguita un'analisi di sensibilità variando lo spessore del film, il modello e il modo in cui il programma calcola la temperatura adiabatica di parete, in modo da osservarne il comportamento al variare di questi parametri.

Il modello scelto, infine, verrà utilizzato per simulare dei test con l'acqua, invece del kerosene, come refrigerante.

Parole chiave: film cooling, motore a razzo a propellente liquido, coefficiente di scambio termico, modello di film cooling, cherosene, acqua

Estratto del lavoro svolto

Questa tesi analizza la tecnica del film cooling paragonando i risultati numerici a quelli sperimentali ottenuti grazie alla camera di prova in scala ridotta del TUM, Technische Universität München, di Monaco di Baviera.

Film cooling

La tecnica del film cooling protegge le pareti della camera di combustione dal calore eccessivo con un sottile strato di refrigerante (che di solito è il carburante stesso) che è iniettato attraverso fori, fessure, iniettori o speciali applicatori.

L'effettivo spessore del film decresce nella direzione del flusso a causa dell'interazione tra refrigerante e gas caldi. Il refrigerante altera il profilo termico nello strato limite e riduce i flussi termici verso le pareti della camera di combustione.

Il refrigerante può essere liquido o gassoso. Nel film cooling liquido il calore è trasferito soprattutto per evaporazione; in quello gassoso lo scambio termico avviene per passaggio di stato.

Un raffreddamento inefficiente può risultare in un sovra-raffreddamento delle pareti nella regione di iniezione o in elevate sollecitazioni termiche causate da forti gradienti della temperatura di parete.

La tecnica del film cooling può essere efficacemente utilizzata per proteggere le pareti della camera di combustione e dell'ugello, per esmepio, in queste situazioni:

- riduzione della temperatura adiabatica di parete al di sotto del limite di resistenza del materiale;

- mantenere un gas non ossidante adiacente alle pareti che altrimenti non sarebbero in grado di sopportare le elevate temperature sprigionate dal processo di combustione.

Per poter descrivere e confrontare modelli e risultati relativi al film cooling diversi, un parametro ampiamente usato è l'efficienza η, definita come:

$$\eta = \frac{T_{ad} - T_{HG}}{T_c - T_{HG}} \tag{1}$$

In generale l'efficienza dipende da numerosi parametri: geometrici (angolo e altezza di iniezione, numero di fori di iniezione), fluidomeccanici (spessore di strato limite, blowing ratio, numero di Raynolds) e termodinamici (pressione, temperatura e proprietà del fluido refrigerante).

Se il fluido è un liquido ci sarà una regione dove il raffreddamento avverà per evaporazione e poi, una volta che tutto il liquido si sarà consumato, si passerà a un film cooling di tipo gassoso. Nel film cooling liquido, finchè il film liquido esiste, il calore trasferito per convezione alle pareti della camera di combustione è effettivamente zero e poi le pareti saranno comunque protette da un film gassoso.

Correlazioni di Nusselt semi-empiriche

Durante la progettazione delle camere di combustione, le formule semi-empiriche sono spesso utilizzate per stimare lo scambio termico tra i gas caldi e le pareti. La correlazione più comunemente utilizzata è quella di Nusselt, che ha la forma:

$$Nu = C\,Re^m Pr^n \tag{2}$$

In questa tesi verranno esaminate sette correlazioni di Nusselt ricavate da sette diversi autori.

Cinjarew

$$Nu = 0.0162 \cdot (Re \cdot Pr_{eff})^{0.82} \left(\frac{T_{HG}}{T_{HW}}\right)^{0.35} \tag{3}$$

Kays and Crawford

I due autori danno una stima del numero di Prandtl effettivo, da utilizzare in combinazione con una delle relazioni di Nusselt; in questa tesi si è usata quella ricavata da Cinjarew.

$$Pr_{eff} = \frac{1 + \left(\frac{\varepsilon_m}{\nu}\right)}{\frac{1}{Pr} + \left(\frac{\varepsilon_m}{\nu}\right)\frac{1}{Pr_t}} \tag{4}$$

$$Pr_t = \frac{1}{\frac{1}{2Pr_{t_\infty}} + 0.3Pe_t\sqrt{\frac{1}{Pr_{t_\infty}}} - (0.3Pe_t)^2 \left[1 - \exp\left(-\frac{1}{0.3Pe_t\sqrt{Pr_{t_\infty}}}\right)\right]} \tag{5}$$

Pavli

$$Nu = 0.023 \cdot Re_{film}^{0.8} Pr_{film}^{0.4} \left(\frac{T_{WG,ad}}{T_{film}}\right)^{0.8} \left(\frac{x_i}{x_\star}\right)^{-0.2} \tag{6}$$

Krueger

$$Nu = 0.0307 \cdot Re_{ref}^{0.8} Pr_{ref}^{0.333} \left(\frac{T_{HG}}{T_{ref}}\right)^{0.8} \left(\frac{x_i}{x_\star}\right)^{-0.2} \tag{7}$$

Bishop

$$Nu = 0.0069 \cdot Re^{0.9} Pr^{0.66} \left(\frac{\rho_{HW}}{\rho_M}\right)^{0.43} \left(1 + 2.4\frac{D}{x}\right) \tag{8}$$

Mokry

$$Nu = 0.0061 \cdot Re^{0.904} Pr^{0.684} \left(\frac{\rho_{HW}}{\rho_M}\right)^{0.564} \tag{9}$$

Swenson

$$Nu = 0.00459 \cdot Re_{HW}^{0.923} Pr_{HW}^{0.613} \left(\frac{\rho_{HW}}{\rho_M}\right)^{0.231} \tag{10}$$

Thermtest

La preparazione di prove su una nuova camera di combustione richiede la capacità di calcolare, prima di iniziare i test, i carichi termici sulla struttura. Per fare questo lo scambio termico convettivo è calcolato grazie a relazioni semi-empiriche di Nusselt. Il vantaggio di questo approccio è una soluzione abbastanza accurata ma veloce, in confronto a metodi più sofisticati come i codici CFD.
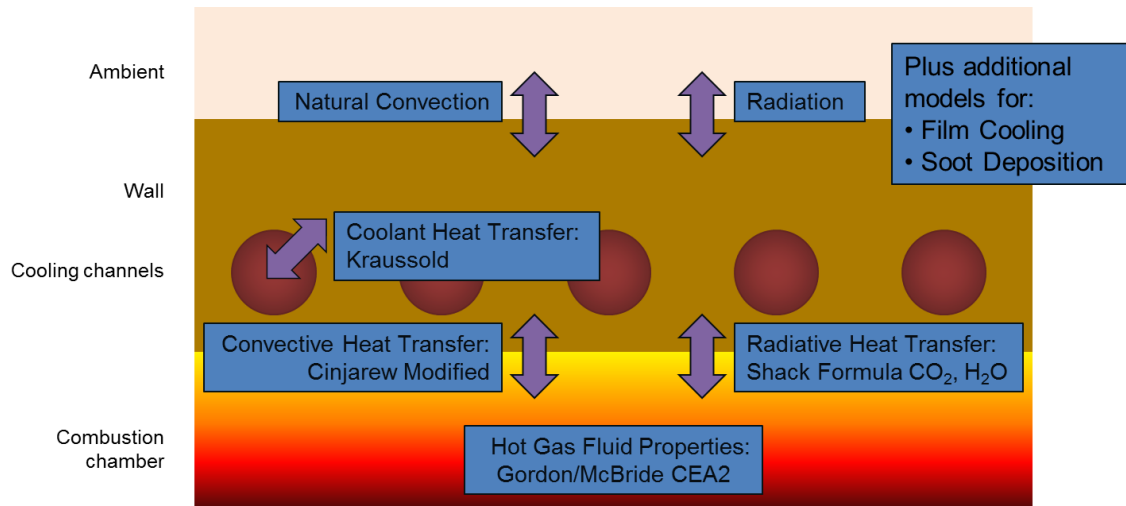
Figura 1: Modello dello scambio termico ("approccio comune")

L'"approccio comune" utilizza come proprietà dei gas caldi quelle calcolate attraverso il programma NASA CEA2. Nel programma CEA2 l'evoluzione della temperature causata dalle reazioni chimiche e l'atomizzazione dei reagenti sono trascurate e quindi lo sono anche in Thermtest. Come accennato in precedenza lo scambio termico convettivo dai gas caldi alle pareti e dalle pareti al refrigerante è modellate grazie a correlazioni semi-empiriche. Thermtest considera anche lo scambio termico radiativo.

I parametri in input che servono a Thermtest per calcolare i flussi termici sono riportati nella figura seguente:
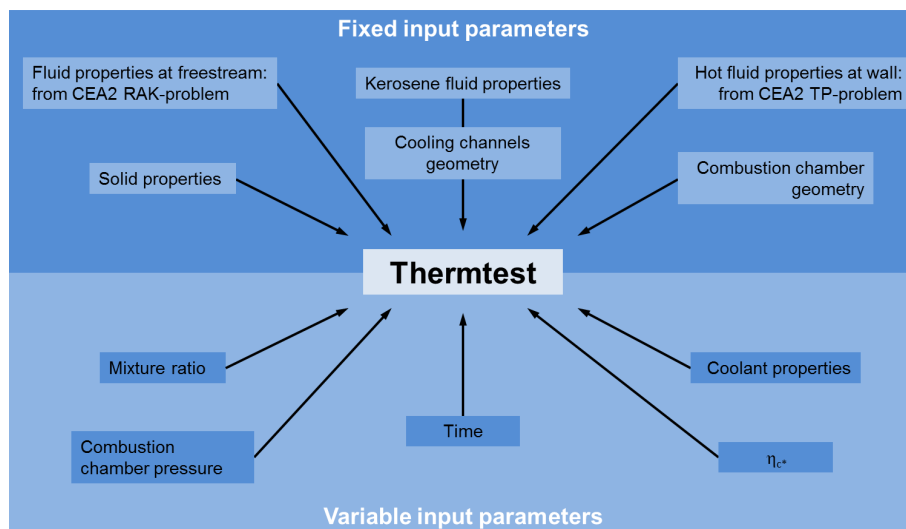
Figura 2: Parametri di input di Thermtest

In Thermtest sono implementati due differenti modelli per il film cooling: NASA A è utilizzato quando il refrigerante è un gas, NASA B quando è un liquido.

Risultati numerici e sperimentali

I punti di carico analizzati sono stati scelti per spaziare su differenti valori di pressione, rapporto di miscela e percentuale di refrigerante tra la moltitudine di dati sperimentali disponibili. Sono

state studiate pressioni di 20, 40, 60 e 80 bar.

Per confrontare i dati numerici con quelli sperimentali si sono calcolati i flussi termici integrali e li si sono presentati in istogrammi in modo da mostrare la differenza dei modelli dai risultati sperimentali.
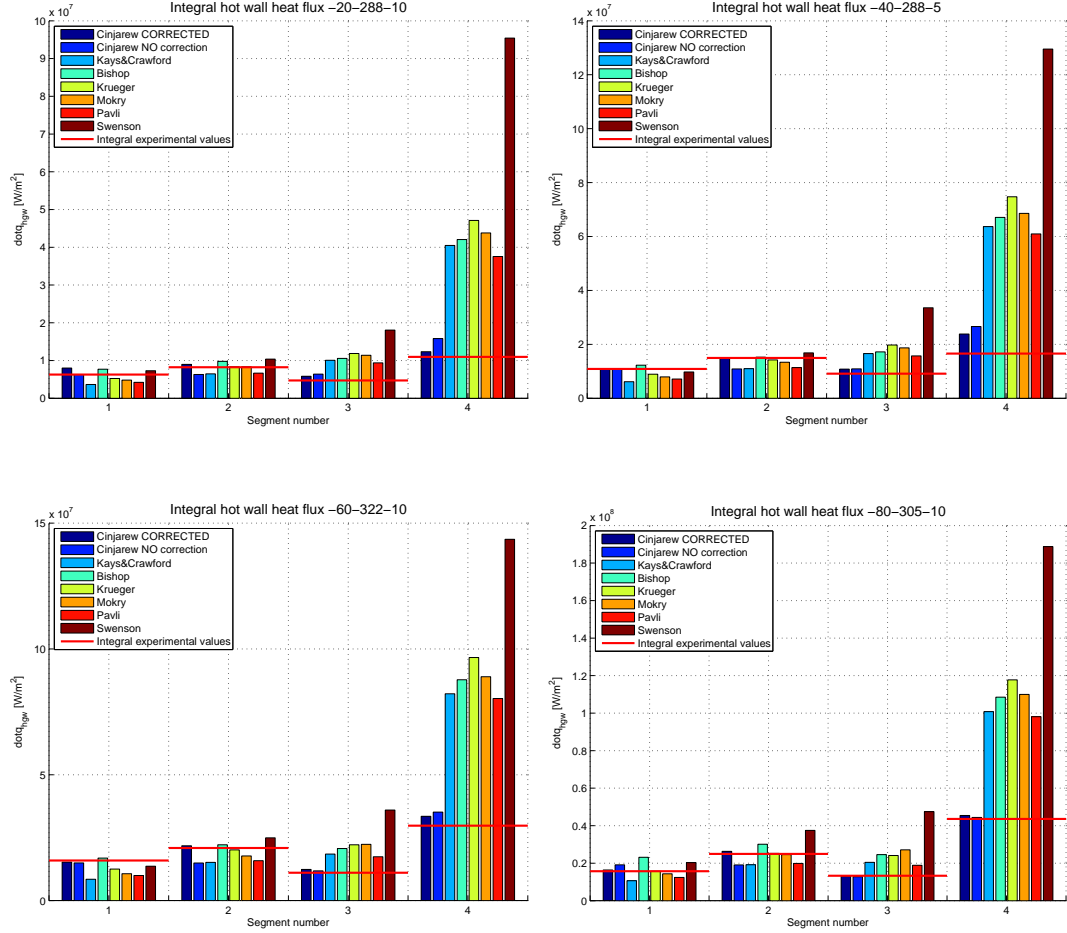
Figura 3: Flussi termici integrali

Dai grafici sono visibili due andamenti: nei primi due segmenti i modelli sotto-stimano i valori sperimentali, mentre negli altri due segmenti i nuovi modelli sovra-stimano i valori sperimentali per tutti i punti di carico considerati. In particolare è possibile notare che nei primi due segmenti i modelli di Bishop, Krueger e Mokry sono quelli che simulano meglio i dati sperimentali. Per questo motivo questi tre modelli sono quelli che verranno ottimizzati per la camera di combustione del TUM.

Ottimizzazione

Lo scopo dell'ottimizzazione è di descrivere i dati sperimentali con una correlazione di facile utilizzo in modo da ottenere un fattore di correzione da applicare in Thermtest. Per fare questo i dati sperimentali sono stati correlati dalla seguente relazione:

$$q_{correlation} = a \cdot OF^b \cdot PCC^c \tag{11}$$

I flussi termici sono descritti da tre parametri: a è un moltiplicatore, b descrive l'influenza del rapporto di miscela e c l'influenza della pressione in camera di combustione.

Fatto ciò viene definito un fattore di correzione che viene utilizzato per calcolare i flussi termici corretti:

$$\Delta q = \frac{q_{Thermtest} - q_{correlation}}{q_{correlation}} = x \cdot OF^y \cdot PCC^z \tag{12}$$

$$q_{corrected} = \Delta q \cdot q_{Thermtest} \tag{13}$$

Il calcolo delle costanti x, y e z è stato effettuato minimizzando l'errore:

$$error = \frac{|q_{corrected} - q_{correlation}|}{q_{correlation}} \cdot 100 \tag{14}$$

I valori delle costanti sono riportati nel capitolo 6 della parte in inglese di questa tesi di laurea.

Le figure seguenti riportano i risultati dell'applicazione della correzione appena calcolata ai tre modelli rimasti; si sono confrontati inoltre i modelli corretti con quelli originali.
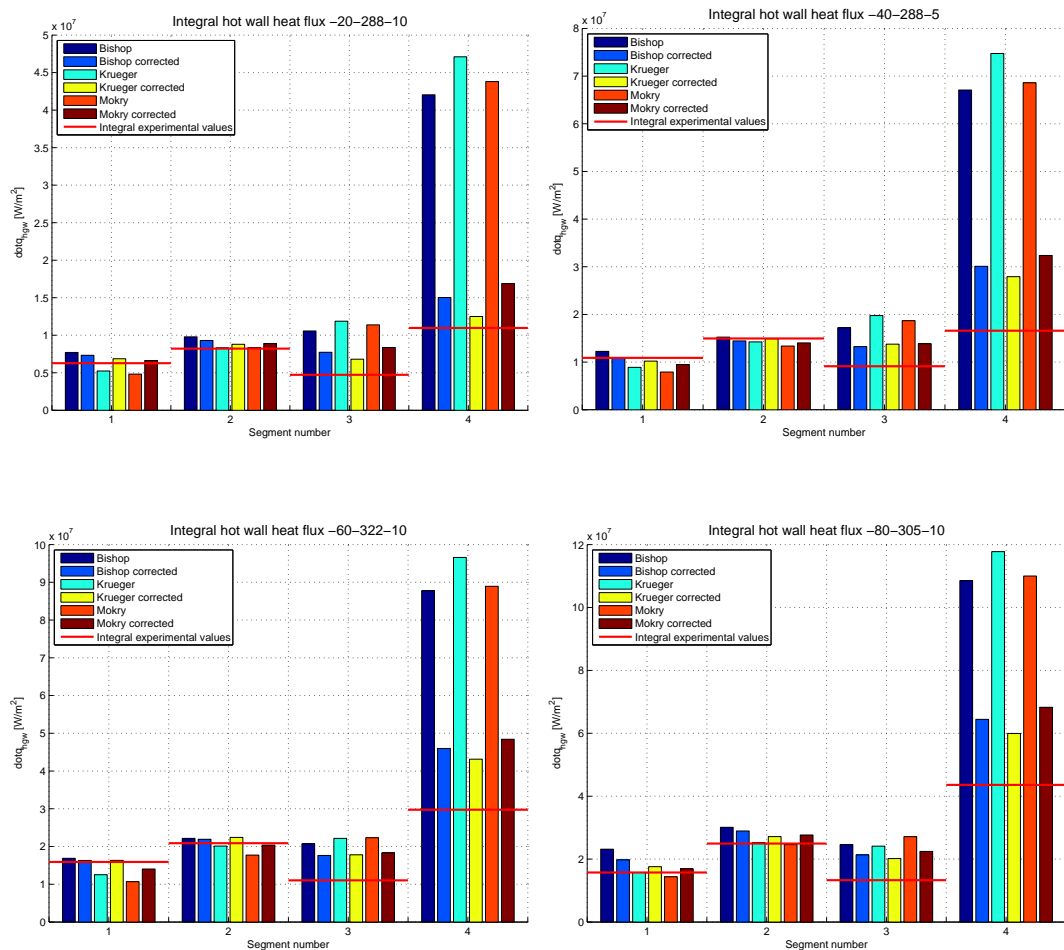
Figura 4: Flussi termici prima e dopo la correzione

Dalle figure si può notare che l'impatto della correzione sui flussi termici è chiaramente visibile: tutti i flussi termici in tutti i segmenti, infatti, sono più vicini ai risultati sperimentali che i modelli originali; nell'ugello però gli errori rimangono elevati. Il modello di Krueger è quello che mostra i risultati migliori.

Analisi di sensibilità

Dopo aver scelto come miglior modello approssimante quello di Krueger ottimizzato, si è effettuata un'analisi di sensibilità al modello di film cooling (NASA A vs NASA B), al modo di calcolare la temperatura adiabatica di parete e allo spessore di refrigerante.

Per quanto riguarda il modello di film cooling si sono ottenuti risultati contrastanti: a 20 e 40 bar NASA A fornisce risultati leggermente più vicini a quelli sperimentali mentre ad alte pressioni, 60 e 80 bar, è il modello NASA B che dà i risultati migliori.

La temperatura adiabatica di parete può essere calcolata in due modi:

$$T_{aw} = \frac{H_{aw} - \eta H_{c,sv} + \eta c_{p_v} T_{if} + (1 - \eta)\left(c_{p_e} T_{tot,e} - H_e\right)}{\eta c_{p_v} + (1 - \eta)\, c_{p_e}} \tag{15}$$

$$T_{aw} = T_{rec} - \eta\left(T_{rec} - T_{film}\right) \tag{16}$$

Dai risultati delle simulazioni si nota che la seconda formula (ricavata dall'inversione dell'espressione dell'efficienza del film cooling) fornisce risulati sensibilmente più accurati rispetto alla prima.

Raddoppiando e dimezzando lo spessore del refrigerante non si notano variazioni significative dei flussi termici, i modelli sono quindi poco influenzati da questo parametro.

Simulazione delle prove con acqua come refrigerante

Una volta scelto il modello di scambio termico migliore per simulare i test con cherosene, Thermtest è stato modificato per essere in grado di utilizzare l'acqua come refrigerante. In particolare si sono dovute inserire le formule per il calcolo di alcune proprietà come la temperatura di saturazione, l'entalpia di vaporizzazione e la tensione superficiale. Tutte queste quantità sono state ricavate grazie a equazioni sviluppate dall'International Association for the Properties of Water and Steam (IAPWS).
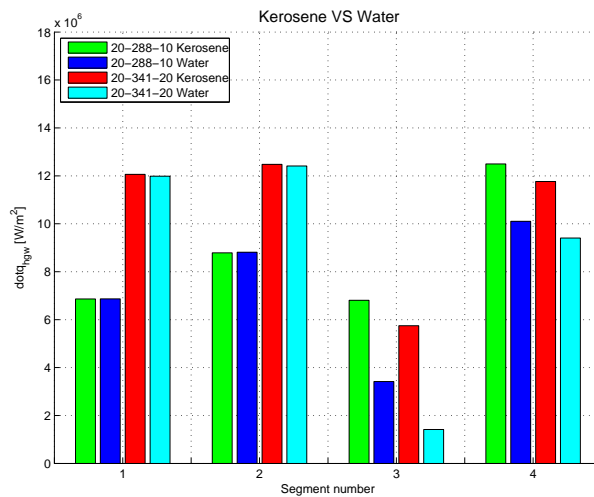
Figura 5: Flussi termici integrali - Cherosene vs acqua

Osservando la figura 5 si nota come i flussi termici quando il refrigerante è l'acqua siano sempre inferiori ai casi in cui si utilizza il cherosene; l'acqua infatti ha una capacità termica più elevata rispetto a quest'ultimo ed è quindi in grado di assorbire una quantità di calore più elevata prima di essere completamente vaporizzata.

Conclusioni

Durante questo lavoro di tesi è stata condotta un'analisi degli aspetti principali del film cooling, diversi articoli e lavori, sia sperimentali che teorici, riguardo questa tecnica sono stati analizzati.

Si sono studiati nuovi modelli per lo scambio termico per avere più di un modello che calcoli correttamente i flussi termici: le stime in questo modo sono più affidabili.

Nessuno dei modelli ha dato però risultati soddisfacenti specialmente nei segmenti dove il film cooling era presente. Nel terzo e nel quarto segmento i flussi termici sono costantemente sovra-stimati e gli errori sono molto elevati. Per questo è stata necessaria un'ottimizzazione del modello.

L'ottimizzazione è stata applicata ai tre modelli che davano risultati migliori nei primi due segmenti cioè Bishop, Krueger e Mokry. Dopo essere stato ottimizzato, attraverso una correzione che minimizza l'errore tra flussi termici sperimentali e calcolati, il modello sviluppato da Krueger si è rivelato essere il migliore per la stima dei flussi termici nella camera di combustione del TUM-LFA.

Questo modello è stato poi sottoposto ad un'analisi di sensibilità. Per quanto riguarda il modello di film cooling si sono riscontrati risultati contrastanti tra i due modelli presi in considerazione (NASA A gassoso e NASA B liquido): è possibile che un miglioramento della stima dei flussi termici si ottenga con un mix dei due modelli. Il calcolo della temperatura adiabatica di parete con l'inversione della definizione di efficienza del film cooling, ha dato risultati più vicini a quelli sperimentali per ogni punto di carico considerato. Lo spessore di refrigerante, infine, non comporta significative variazioni nel calcolo dei flussi termici.

La simulazione dei test con l'acqua come refrigerante ha messo in evidenza come quest'ultima abbia un potere refrigerante maggiore rispetto al cherosene.

Sviluppi futuri

Dal punto di vista numerico, l'implementazione di un modello affidabile di film cooling nell'ugello migliorerebbe la stima dei flussi termici nella camera di combustione. Anche l'implementazione delle reazioni chimiche favorirebbe la riduzione dell'errore tra risultati numerici e sperimentali.

Un altro miglioramento potrebbe essere quello di implementare un modello di film cooling che sia una via di mezzo tra uno liquido e uno gassoso: liquido fino alla "liquid film cooled length", cioè fino a quella distanza dal punto di iniezione dove il refrigerante è ancora liquido, e poi gassoso; in questo modo si simulerebbe veramente quello che accade nella camera di combustione.

Abstract

Film cooling is a widely used technique that permits to cool the rocket engines, either alone or in combination with other methods. It consists in the injection of a fluid near the combustion chamber walls through holes, slots, injector elements or special applicators. The structure is protected by the hot gases impact, thus the near-wall gas temperature is reduced and so the heat transfer. This thesis work analyses this technique comparing numerical and experimental results. Experiments were conducted at the subscale combustion chamber test facility of TUM, Technische Universität München, at the Lehrstuhl für Flugantriebe (LFA), the institute for flight propulsion.

This thesis work focus on the implementation of new heat transfer coefficient and on new film cooling models, in order to adjust and check the current predictions of the in-house Matlab written code Thermtest.

New heat transfer coefficient and film cooling models will be implemented and compared with experimental results to find out the best one to predict the hot wall heat fluxes. After choosing one out of the model investigated, a sensibility analysis has been done varying film cooling thickness and model and the way adiabatic wall temperature is calculated.

This model will be then used to simulate the tests with water, instead of kerosene, as film coolant.

Key words: film cooling, liquid rocket engines, heat transfer coefficient, film cooling model, kerosene, water

Chapter 1

Motivation and objectives

This thesis work analyses film cooling technique comparing numerical and experimental results. Experiments were conducted at the subscale combustion chamber test facility of TUM, Technische Universität München, at the Lehrstuhl für Flugantriebe (LFA), the institute for flight propulsion.

Film cooling is a method that helps combustion chamber walls to withstand the high temperatures of the core flow. Therefore studies on film cooling techniques, that involves analytical, numerical and experimental analysis about the heat transfer rates occurring in the chamber must be investigated.

Before starting with long and detailed calculations made with a commercial CFD code, a simulation tool has been developed to make predictions about the main parameters involved in film cooling such as temperatures, heat transfer rates and efficiency. For these reasons TUM-LFA developed the in-house Matlab written code Thermtest. This tool is used in this thesis to simulate heat fluxes and hot wall temperatures of the TUM-LFA subscale rocket combustion chamber.

The rocket combustion chamber works with gaseous oxygen as oxidizer and Kerosene JetA-1 as fuel and it is regeneratively cooled. It can withstand high pressure levels, up to 100 bar, and mixture ratios close to the stoichiometric value, that is 3.4 for the combination GOX/Kerosene.

The film cooling can be divided into two big categories: gaseous and liquid. In reality this definition is not so strict, because the conditions of the liquid injected as coolant are unknown: it is very often at supercritical conditions, moreover the liquid completely vaporizes after a certain tract, producing a gaseous film layer further downstream the injection point.

In the first part of the work an analysis of the film cooling fundamentals is performed, different works and papers have been studied, in order to have a clear idea about this cooling technique. The next step consists in the research of analytical models that can predict the main film cooling parameters and the hot wall heat transfer coefficient.

Then the selected heat transfer coefficient models were implemented in Matlab in order to adjust and check the current predictions of the in-house Matlab written code Thermtest. Having two or three different modelling approaches available which lead to comparable results, the overall confidence in the simulation is increased. On the other hand the implementation of new heat transfer and film cooling model will be useful in the future when switching from kerosene to methane as fuel. Moreover other fluid, as water or argon, are going to be used as film coolant instead of kerosene and Thermtest have been adjusted to simulate this change.

Comparison between numerical and experimental results will lead in finding the best model that predicts the hot wall heat fluxes. To improve the experimental heat fluxes prediction three models were optimized and, in the end, one was chosen as the best model to predict the heat fluxes.

This model than undergone a sensibility analysis varying film cooling thickness and film cooling model and the way adiabatic wall temperature is calculated, to see the behavior in relation to these parameters.

After that the model will be used to simulate tests with water, instead of kerosene, as film coolant. It is, in fact, in program to switch from kerosene to water as film coolant and is necessary to know which level of heat fluxes are to be expected during the experimental tests.

Chapter 2

Heat transfer and film cooling

This chapter, after a brief, general description of cooling method of liquid rocket engines, will focus on one of this, film cooling.

Why is it necessary? How does it work? What is the film cooling effectiveness? Which are the parameters that influence this cooling method? These are the questions that this chapter tries to answer.

After that some Nusselt correlation for the determination of the convective heat transfer coefficient are presented, focusing in particular on how these correlation were developed.

Finally there is the description of the new film cooling model implemented in Thermtest.

2.1 Thrust chamber cooling

Some of the primary objectives of a liquid rocket motor are engine reliability, improvement of the specific impulse I_{sp} and engine thrust level. Assuming constant engine dimensions, enhanced engine performance can only be realized with an increase of propellant mixture ratio O/F and/or chamber pressure P_{cc}. Both improvements mean an additional increase in structural as well as in thermal loads for the combustion chamber walls. A higher combustion chamber pressure, in fact, results in an almost linear increase of the heat flux level q from the hot gas to the liner material [3]:

$$q \propto P_{cc}^{0.8} \tag{2.1}$$

Therefore due to the high combustion temperature, that may exceed $3600\ K$, and the high heat transfer rates (peak may go beyond 100 MW/m^2) encountered in a combustion chamber, a cooling technique is required in order that the chamber walls can withstand these high loads.

One or a combination of the following chamber cooling methods can be used to successfully meet this challenge [8, 16]:

- *Regenerative cooling*: is the most widely used method of cooling a high performance combustion chamber and is accomplished by flowing high velocity coolant over the back side of the chamber hot gas wall to convectively cool the hot gas liner. The coolant, heated up by the hot liner, is then discharged into the injector and used as a propellant.
  The best regenerative cooling solution to date is the "channel wall" design where the hot gas wall cooling is accomplished by flowing coolant through rectangular or cylindrical channels, which are machined or formed into a hot gas liner fabricated from a high-conductivity material.
  Engines that have this kind of cooling are, for example, the H-1, J-2, F-1 and RS-27.

- *Ablative cooling*: this method uses a particular combustion gas-side wall material that is sacrified, by melting, vaporization and chemical changes, to dissipate heat. As a result, relatively cool gases flow over the wall surface, thus lowering the boundary-layer temperature and assisting the cooling process.
  Ablative cooling may be applied only to the nozzle throat or to the entire combustion chamber

liner and also to solid rockets.

Examples of engines with partially ablative cooled throat sections are the Viking and the RS-68.

- *Radiative cooling*: heat is radiated away from the surface of the outer chamber walls. Usually this method is applied when thermal stresses are low, such as monopropellant rocket, gas generator or nozzle extension. In high performance liquid rockets, radiative cooling is used generally in nozzle extensions and regenerative cooling in the combustion chamber; low thrust liquid rockets are, instead, cooled with a combination of film and ratiative cooling.
  An example of entirely radiation cooled thruster is the RS-21 Mariner/Viking Orbiter spacecraft.

- *Transpiration cooling*: it is accomplished by introducing a coolant (gaseous or liquid) through porous chamber walls at a rate sufficient to maintain the desired combustion gas side chamber wall temperature.
  This technique was applied to cool the injector faces of the J-2, RS-44 and SSME.

- *Film cooling*: the chamber walls are protected from excessive heat with a thin film of coolant (which usually is the propellant itself) which is injected through orifices near the injector or near the throat with special slots.
  This method has been widely used, in particular for high heat fluxes, alone or in combination with regenerative cooling.
  Sample engines were film cooling is applied are the SSME, F-1, J-2, RS-27, Vulcain 2, RD-171 and RD-180.

2.2   Film cooling

As stated before, as a result of the high heat fluxes, to protect the integrity of the combustion chamber, it is necessary an active cooling of the structure from the impact of the hot combustion gases. Film cooling is one of the most used cooling methods in rocket engines, not only at the position of the film injection but also further downstream the combustion chamber.

The injection of the coolant, either gaseous or liquid, is provided by slots, holes or special film applicator (as in TUM combustion chamber, see chapter 3) or by the injector itself.

The effective thickness of the coolant film decreases in the direction of the flow, because of the interaction between coolant film and combustion gases, as a result of heat and mass transfer. Sometimes it is therefore necessary to inject additional coolant downstream of the first injection slot.

The coolant alters the temperature profile through the thermal boundary layer and decreases the heat fluxes to the chamber walls. If a combustion chamber of short length is used, film coolant injection can be provided at the injector face and the film cooling effect will persist till the throat region. Otherwise more film cooling injection point must be used and could be located at incremental distances along the chamber walls.

In liquid film cooling, heat is transferred principally by means of evaporation; in gaseous film cooling, heat transfer occurs by means of sensible heat exchange.

Film cooling may be used effectively to protect the combustion chamber and nozzle walls for example in these ways:

- reduction of the adiabatic wall temperature to a value below the material limit;

- maintaining a non-oxidizing gas adjacent to refractory surfaces otherwise not capable of withstanding full combustion gas temperature.

With film cooling there are no limitation on cooling capacity (as with regenerative cooling), time (as with ablative cooling) or chamber pressure (as with radiation cooling). However a disadvantage to film-cooled design is when one of the propellants (usually the fuel) or an inert fluid is used as a coolant: there is a specific impulse loss due to gas and temperature stratification. An additional

specific impulse loss may be incurred due to the operation at propellant mixture ratios other than optimum in order to insure sufficient propellant as film coolant. Other problems, in particular for liquid film cooling, could be surface film stability under high turbulence, phase changes along the cooled length and endothermic and exothermic decomposition.

Although heat protection exclusively by film cooling has not been applied in the past for main/core stage only, it is significant that in practice regenerative cooling is nearly always supplemented by some form of cooling. In most cases a fuel-rich gas boundary layer is created by the injection of fuel from the outermost circle of injector orifices, toward the chamber walls. An important advantage of film cooling is the fact that it reduces heat transfer to the walls and consequently thermal stresses become less critical. This is an important consideration, as thermal stresses may establish the feasibility limits of conventional regenerative cooling [19].

In literature there are many analytical and experimental works on film cooling model for liquid rocket engines. Here, for completeness, there is a list of the most important published models:

- film cooling model by Ziebland and Parkinson [52],

- film cooling model by Hatch and Papell [17],

- film cooling model by Klein and Tribus [29],

- gaseous and liquid film cooling model by Ewen and Evensen (NASA SP-8124) [10],

- gaseous and liquid film cooling model by Terry and Caras [48],

- liquid film cooling model by Yu, Schuff and Anderson [51],

- liquid film cooling model by Huzel and Huang (NASA SP-125) [19],

- liquid film cooling model by Gater and L'Ecuyer [11],

- liquid film cooling model by Grissom [14],

- liquid film cooling model by Shembharkar and Pai [44],

- liquid film cooling model by Stechman [46, 47],

- DLR experiments on film cooling [3, 4],

- TUM experiments on film cooling [26, 27, 28, 41],

- film cooling effectiveness by Goldstein and Haji-Sheikh [12],

- film cooling model for a RP1-GOX motor by Haberlen, Greisen and Anderson [15].

2.2.1   Film coolant injection

Efficient methods of injecting liquid film coolant are required to provide uniform coverage and to minimize liquid entrainment by the combustion products. The combination of film-coolant orifice diameter and spacing affects circumferential distribution of heat fluxes. A small orifice spacing is desirable but sometimes is difficult to achieve with reasonably sized orifices. Orifices with a diameter less than 0.25 mm are difficult to machine accurately and are susceptible to plugging problems, although orifices with a diameter of 0.25 mm have been used. Experience has shown that a maximum center-to-center orifices spacing of 6 to 12 mm will provide a sufficiently uniform film-coolant coverage [10].

Larger spacing with improved circumferential distribution can be accommodated by swirling the film coolant: however swirling, for example, cannot be used in presence of injector baffles.

Another method used is the impingement of pairs of film cooling streams to provide tangential fan patterns. The angle at which liquid film coolant impinges on the chamber wall is important in providing good coverage and in minimizing droplet formation and entrainment from the liquid film.

2.2.2   Film cooling effectiveness

For describing and comparing different film cooling results and models, adiabatic film cooling effectiveness η is a widely used parameter. The difference between adiabatic wall temperature (T_{ad}) and hot gas temperature (T_{HG}) is referred to the maximum difference between coolant temperature at the point of injection (T_c) and hot gas temperature:

$$\eta = \frac{T_{ad} - T_{HG}}{T_c - T_{HG}} \tag{2.2}$$

There are two possible approaches for correlating film cooling data: assume that the film does not mix with the core flow and the heat is transferred only to the film, or assume that mixing phenomena take place and effectiveness is lowered by the influence of the hot gas.

The first approach is the one by Hatch and Papell [17], in which the film is assumed to be of uniform average temperature at any position downstream of the point of injection and heat is conducted into the film at the same rate as to the wall in the absence of the cooling film.

The second approach is the one by Stollery and El-Ehwany [52]. It assumes that far enough downstream the film will tend to have similar velocity profile and mixing characteristics to a simple boundary layer. The Hatch and Papell method tend to give better correlations close to the injector slot, and the model of Stollery and El-Ehwany further downstream.

Film cooling layers will be sensitive to turbulence generated above the coolant layer. Additionally turbulence generated by the bluntness of the slot-lip or by velocity gradients between film and main stream, will dissipate the coolant film faster than it would be otherwise. Viceversa if the coolant Reynolds number is sufficiently low, laminar flow may exist and effectiveness will be increased.

However, the definition of effectiveness shown in equation 2.2 cannot be applied in a typical high performance rocket combustion chamber due to the extreme high temperatures of the combustion gases and therefore extreme wall heat fluxes. Adiabatic wall temperatures would exceed safe operating temperatures of all known combustor materials. Hence, for a high-pressure combustion chamber, regenerative and film cooling will be used in combination.

It is, therefore, imperative to establish a different temperature ratio to describe film cooling effectiveness for a regenerative and film-cooled rocket combustion chamber. This new temperature ratio can be used as a measure of effectiveness for film cooling processes.

The local temperature difference due to the application of film cooling will be compared with the maximum achievable temperature difference, where $T_{W,0}$ designates the wall temperature without and $T_{W,f}$ the wall temperature with film cooling:

$$\Theta\left(x\right) = \frac{T_{W,0} - T_{W,f}}{T_{W,0} - T_c} \tag{2.3}$$

In general, film cooling effectiveness is dependent on a multitude of geometrical (injection angle, slot height, slot width and number of slots), fluidmechanical (blowing rate, ratios of momentum flux, boundary layer thickness, turbulence levels and Reynolds number) and thermodynamical parameters (pressure, temperature and fluid properties).

The blowing rate M is a main parameter to characterize film cooling and describes the ratio of the mass velocity of the coolant to the hot gas stream mass velocity:

$$M = \frac{\rho_c u_c}{\rho_{cc} u_{cc}} \tag{2.4}$$

An increase of the blowing rate M up to $M \approx 3$ indicates a better film cooling effectiveness for tangential slot injection. This also apply for foreign gas injection in place of the well-examined test case of air injected into air [1, 2, 3, 4].

2.2.3   Liquid film cooling

If the fluid injected as coolant along the walls is a liquid and not a gas, there will be an initial region in which the cooling takes place by the evaporation of the liquid film and only after that, with the liquid completely vaporized, the process will behave as gaseous film cooling.

In liquid film cooling the vaporized film coolant does not diffuse rapidly into the main gas stream but persist as a protective mass of vapor adjacent to the walls for an appreciable distance downstream of the terminus of the liquid film.

Liquid film cooling has an advantage over gaseous film cooling because the density storage requirements are less and the utilization of the latent heat of vaporization of a liquid significantly improves the cooling method. Liquids, in fact, have generally higher specific heat than gases, even if hydrogen and helium are exceptions.

Liquid film is very attractive because, as long as the liquid film exists, the heat transferred to the walls by convection will be effectively zero and, even when the liquid film will not exist anymore, the walls will be protected by the vapor film. In the case where a real liquid film layer exists, the effectiveness would be equal to unity and the temperature of the wall would be at maximum equal to the vapor saturation temperature of the coolant. Therefore a liquid film cooled length could be defined, that is the length beyond which the film no longer exists.

Liquid film cooling shares the simplicity of gaseous film cooling and does not require massive structural difficulties; additionally the presence of a phase change significantly increases the cooling capability as compared to gaseous film cooling. However, this cool layer near the chamber walls reduces the derivable kinetic energy of the propellants which leads to performance losses.

Figure 2.1 illustrates the liquid film cooling process. A liquid coolant is injected onto the wall surface and establishes a continuous protective layer. Heat energy from the hot gases increases the sensible enthalpy of the film by radiation, convection and conduction. After that the saturation temperature is reached, heat is used to vaporized the coolant.
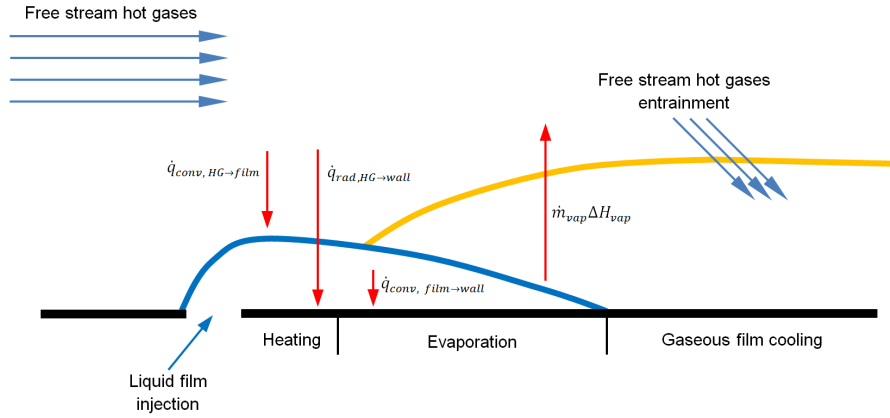
Figure 2.1: Model of film cooling process

The liquid film terminates at some point downstream of the injector as a result of evaporation and its entrainment into the core gas stream. Downstream of the liquid termination point, the vapor provides thermal blockage through gaseous film cooling [11, 14, 51].

Assuming that the liquid film coolant is stable and non-reacting, it is possible to write the heat balance at the gas-liquid interface:

$$\int_{x_0}^{x_1} (\dot{q}_{cond,l} + \dot{q}_{rad,l})\, dx = \int_{x_0}^{x_1} [(\dot{m}_{HG} c_{p_l} T_l - \dot{m}_s h_v) + (\dot{q}_{cond,g} + \dot{q}_{rad,g})]\, dx \qquad (2.5)$$

Left hand side of equation 2.5 stands for the heat energy transferred into the liquid film from the gas-liquid interface. The right hand side represents the energy transferred to the gas-liquid interface from the hot temperature gas and the first two terms account for the energy change due to mass loss from entrainment and evaporation.

2.3   Semi-empirical Nusselt correlations for heat transfer

In rocket engine combustion chamber design, semi-empirical correlations are often used for first design and to guess loads. Heat transfer depends on parameters such as:

- density ρ,

- flow velocity u,

- combustion chamber diameter d,

- viscosity η,

- thermal conductivity λ,

- specific heat c_p.

The dimensionless quantities involved in convective heat transfer are:

- Nusselt number:

$$Nu = \frac{\alpha d}{\lambda} \tag{2.6}$$

- Reynolds number:

$$Re = \frac{ud}{\eta} \tag{2.7}$$

- Prandtl number:

$$Pr = \frac{c_p \eta}{\lambda} \tag{2.8}$$

- Stanton number:

$$St = \frac{\alpha}{\rho u c_p} \tag{2.9}$$

It is also useful to note that this identity subsists:

$$St = \frac{Nu}{RePr} \tag{2.10}$$

Nusselt number can be considered the ratio of actual heat transfer rate (α) and the heat transfer of a conduction process (d/λ). Reynolds number is the ratio of inertia force ($\rho u d$) and viscous force (η). Prandtl number denotes the ratio between frictional dissipation ($c_p \eta$) and thermal conduction (λ). Stanton number, finally, is the ratio of heat transfer (α) and mass heat transfer ($\rho u c_p$).

Now, if there exists a relation that measures the heat transfer directly and can be written with these quantities, the effect of those on the heat transfer would not be as hard to determine as for all the properties separately.

The numerical solution of the Blasius equation in incompressible flat plate flow [45] yields for the friction coefficient:

$$\frac{c_f}{2} = \frac{0.664}{\sqrt{Re_x}} \tag{2.11}$$

where x is the distance from the leading edge. For a turbulent boundary layer flow, a similar result has been found:

$$\frac{c_f}{2} = \frac{0.029}{Re_x^{1/5}} \tag{2.12}$$

So it can be noted a general form for the friction coefficient:

$$\frac{c_f}{2} = \frac{C}{Re^p} \tag{2.13}$$

where C and p depend on the specific assumptions for the boundary layer.

It is also possible to derive, for an incompressible flow between a moving plate and a fixed surface a relation between the Stanton number and the friction coefficient:

$$St = \frac{c_f/2}{Pr^q} \tag{2.14}$$

where q depends whether the properties are considered constant or not.

Now combining equations 2.13 and 2.14, the desired relation between the dimensionless quantities, that allow to calculate heat transfer, is found:

$$St = \frac{C}{Re^p Pr^q} \tag{2.15}$$

Or, remembering the identity 2.10, the most commonly used equation for heat transfer, the Nusselt correlation, is found:

$$Nu = C\,Re^m Pr^n \tag{2.16}$$

From the definition of Nusselt number it is now possible to determine the heat transfer coefficient α. The heat transfer coefficient then directly yields the heat flux through equation 2.17:

$$q = \alpha\,(T_{HG} - T_{HW}) \tag{2.17}$$

In Nusselt type correlations, C is a constant which is determined for each specific case and the exponents m and n follows from boundary layer assumptions; however C, m and n can be manually modified to match the experiments.

In addition to the Cinjarew model already implemented in Thermtest (see Chapter 4), six other semi-empirical models by the following authors will be investigated:

1. Kays and Crawford,

2. Pavli,

3. Krueger,

4. Bishop,

5. Mokry,

6. Swenson.

Most of these semi-empirical models were published in the nineteen sixties and seventies and are still used today. To calculate the heat transfer, the models require some gas properties to be determined; the temperature at which these properties are determined is peculiar for every model investigated and will be therefore defined for each semi-empirical model in its relative subsection.

2.3.1 Kays and Crawford

Kays and Crawford model [24, 50] gives an expression for the calculation of the turbulent Prandtl number. It was in principle developed for theoretical predictions of turbulent heat transfer in boundary layers and in duct flows for fluids with low molecular Prandtl numbers (liquid metals). The authors, however, assert that this model can be used also for gaseous and liquid flows.

Turbulent Prandtl number model is given by:

$$Pr_t = \frac{1}{\frac{1}{2Pr_{t_\infty}} + 0.3Pe_t\sqrt{\frac{1}{Pr_{t_\infty}}} - (0.3Pe_t)^2 \left[1 - \exp\left(-\frac{1}{0.3Pe_t\sqrt{Pr_{t_\infty}}}\right)\right]} \tag{2.18}$$

Where:

$$Pe_t = Pr \frac{\varepsilon_m}{\nu} \tag{2.19a}$$

$$\frac{\varepsilon_m}{\nu} = \frac{2 \left(K \cdot y^+ \right)^2}{1 + \sqrt{1 + 4 \left(K \cdot y^+ \right)^2}} \tag{2.19b}$$

$$K = 0.4 \left[1 - \exp \left(-\frac{y^+}{26} \right) \right] \tag{2.19c}$$

$$y^+ = \rho \frac{(R - r) \sqrt{\frac{\tau_w}{\rho}}}{\eta} \tag{2.19d}$$

$$\tau_w = C_f \cdot \frac{1}{2} \rho u^2 \tag{2.19e}$$

$$u = \frac{\dot{m}}{\rho A_t} \tag{2.19f}$$

$$C_f = \left[2 \log \left(Re_x \right) - 0.65 \right]^{-2.3} \tag{2.19g}$$

$$Pr_{t_\infty} = \frac{100}{Pr \cdot Re^{0.888}} + 0.85 \tag{2.19h}$$

Once turbulent Prandtl number is calculated, following [7], it is possible to calculate an effective Prandtl number as a kind of weighted average between molecular and turbulent Prandtl number:

$$Pr_{eff} = \frac{1 + \left(\frac{\varepsilon_m}{\nu} \right)}{\frac{1}{Pr} + \left(\frac{\varepsilon_m}{\nu} \right) \frac{1}{Pr_t}} \tag{2.20}$$

This effective Prandtl number is now used in one of the semi-empirical Nusselt correlation, for example Cinjarew, that is given in equation 2.21:

$$Nu = 0.0162 \cdot \left(Re \cdot Pr_{eff} \right)^{0.82} \left(\frac{T_{HG}}{T_{HW}} \right)^{0.35} \tag{2.21}$$

2.3.2   Pavli

In [35] Pavli developed a Nusselt number correlation that is used as a tool to design cooling passages. This correlation was obtained from data from a 8 *bar* combustion chamber feed with liquid oxygen and gaseous hydrogen. The correlation is as follows:

$$Nu = 0.023 \cdot Re_{film}^{0.8} Pr_{film}^{0.4} \left(\frac{T_{WG,ad}}{T_{film}} \right)^{0.8} \left(\frac{x_i}{x_\star} \right)^{-0.2} \tag{2.22}$$

The first and second term between brackets are respectively a temperature correction factor and a streamwise correction factor [45]; in this one x_i is the local axial coordinate and $x_\star$ is the axial position of the throat.

The other quantities in equation 2.22 are determined at a *film* temperature which is defined as the average of the adiabatic wall temperature ($T_{WG,ad}$) and the actual hot wall temperature. The adiabatic wall temperature is found via the static gas temperature and a recovery factor.

$$T_{film} = \frac{1}{2} \left(T_{WG,ad} + T_{HW} \right) \tag{2.23a}$$

$$T_{WG,ad} = T_{HG} \left(1 + \delta \frac{\gamma - 1}{2} M_\infty^2 \right) \tag{2.23b}$$

where δ is the recovery factor which will, in turbulent flow, rise with Prandtl number to approximately 0.9 [35]. Here, a value of 0.88 was selected, due to the range of Reynolds numbers.

2.3.3 Krueger

In Krueger model [30], heat transfer coefficient is found via the following empirical relation:

$$Nu = 0.0307 \cdot Re_{ref}^{0.8} Pr_{ref}^{0.333} \left(\frac{T_{HG}}{T_{ref}} \right)^{0.8} \left(\frac{x_i}{x_\star} \right)^{-0.2} \tag{2.24}$$

In this equation the *ref* subscript denotes that the relevant gas properties are determined at a reference temperature, that is the Eckert temperature:

$$T_{ref} = \frac{1}{2} \left(T_{HG} + T_{HW} \right) + 0.22 \sqrt[3]{Pr_{ref}} \left(T_0 - T_{HG} \right) \tag{2.25}$$

The reference temperature in turn depends on the reference Prandtl number; therefore an iteration is required. As in Pavli model, last term between brackets is a streamwise correction factor [45].

This correlation was found by data coming from a 4 *bar* combustion chamber operated with F_2 and H_2.

2.3.4 Bishop

Bishop [36] developed his correlation from data coming from experiments with supercritical water flowing upward inside bare tubes with a pressure range of $22.8 \div 27.6 \ MPa$, $T_b = 282 \div 527$°C and $q = 0.31 \div 3.46 \ MW/m^2$.

$$Nu = 0.0069 \cdot Re^{0.9} Pr^{0.66} \left(\frac{\rho_{HW}}{\rho_M} \right)^{0.43} \left(1 + 2.4 \frac{D}{x} \right) \tag{2.26}$$

Last term takes into account an entry region effect that, during the implementation in Thermtest (chapter 4), was considered only till the film cooling applicator. All the relevant fluid properties are calculated at the average temperature between hot wall and hot gas temperature.

2.3.5 Mokry

In 2009 Mokry [34, 36] proposed the correlation of equation 2.27, developed from data of supercritical water, $P = 24 \ MPa$, $T_b = 320 \div 350$°C and $q = 1250 \ KW/m^2$.

$$Nu = 0.0061 \cdot Re^{0.904} Pr^{0.684} \left(\frac{\rho_{HW}}{\rho_M} \right)^{0.564} \tag{2.27}$$

Thermophysical properties are calculated at the average temperature between hot wall and hot gas temperature.

2.3.6 Swenson

In 1965 Swenson [36] suggested the following correlation in which the majority of thermophysical properties are based on hot wall temperature:

$$Nu = 0.00459 \cdot Re_{HW}^{0.923} Pr_{HW}^{0.613} \left(\frac{\rho_{HW}}{\rho_M} \right)^{0.231} \tag{2.28}$$

This equation was obtained from data from experiments with supercritical water, $P = 22.8 \div 27.6 \ MPa$ and $T_b = 75 \div 576$°C.

2.4   New film cooling model

2.4.1   Stechman, Oberstone and Howell

Stechman, Oberstone and Howell [46, 47] film cooling model was developed in the late sixties in order to predict film cooling efficiency in small liquid rockets. For this reason this model was chosen among the others presented in 2.2 to be implemented in Thermtest.

This model was determined applicable for film cooling in rocket engines in the 40 to 4000 N thrust range using earth-storable, space-storable, and cryogenic propellant combination. The model was verified with test data using the propellant combination of nitrogen tetroxide and monomethylhydrazine (N_2O_4/MMH) and fluorine and monomethylhydrazine (F_2/MMH). Fuel was used as film coolant.

In this studies, T_{aw} at any particular film cooling rate is redefined and is called the *effective gas temperature* for non-adiabatic walls and is used in the equation to determine heat transfer due to convection between the combustion gases and the wall:

$$\frac{Q}{A} = \alpha_g \left(T_{eff} - T_{HW} \right) \tag{2.29}$$

To determine film cooling requirements, it was necessary to develop heat transfer equations coupling the combustion gases to the coolant.

The liquid film cooled length is:

$$L = \frac{\psi \dot{m}_l c_{p_l} \left(T_{sat} - T_{inj} \right)}{pp \cdot \alpha_g \left(T_r - T_{sat} \right)} + \frac{\psi \dot{m}_l H_v}{pp \cdot \alpha_g \left(T_r - T_{sat} \right)} \tag{2.30}$$

First term on the right of equation 2.30 represents the distance from the injection point required to increase the effective gas temperature from its initial injection temperature to its saturated liquid temperature. The second term represent the distance needed to completely vaporized the liquid film, that is the length over which the effective gas temperature is constant and equal to the coolant's saturation temperature.

Because of the liquid-film instability, the liquid coolant flow is not completely ideal [13]. Therefore the authors introduced an efficiency factor that is defined as a function of the coolant Reynolds number. Stability efficiency factor has the form shown in figure 2.2.
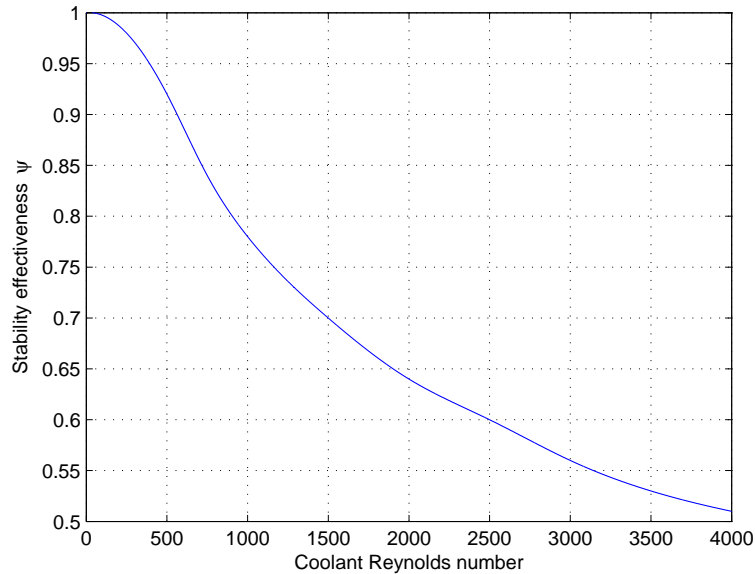
Figure 2.2: Liquid film stability factor

Coolant Reynolds number is defined as:

$$Re_l = \frac{\dot{m}_l}{\pi D \eta_l} \tag{2.31}$$

The equation used to predict the effective gas temperature, in the gaseous coolant region downstream of the liquid film region, is the equation developed by Hatch and Papell in [17].

$$\frac{T_r - T_{eff}}{T_r - T_{sat}} = \exp\left(-\frac{\alpha_{HG} A}{\phi c_{p_c} \dot{m}_c}\right) \tag{2.32}$$

Where:

$$\frac{1}{\phi} = \left(\frac{s \cdot u_{HG}}{a_c}\right)^{0.125} f(\beta) \tag{2.33a}$$

$$\beta = \frac{u_{HG}}{u_c} \tag{2.33b}$$

$$f(\beta) = \begin{cases} (1/\beta)^{-1.5(\beta^{-1}-1)} & \beta \le 1 \\ 1 + 0.4 \tan^{-1}(\beta - 1) & \beta > 1 \end{cases} \tag{2.33c}$$

These equations were derived with the following assumptions:

1. the coolant film exhibits no mixing or chemical reaction with the main core gas,

2. the coolant film temperature profile does not change rapidly as the coolant moves downstream,

3. the gradients across the coolant film are small,

4. no heat transfer occurs in the chamber walls.

Turbulent heat transfer coefficient α_{HG}, present in equation 2.32, from the combustion gases to the film coolant, was calculated using equation 2.34, firstly developed by Bartz [5, 6].

$$\alpha_{HG} = \sigma \cdot \frac{0.026 \cdot \lambda_c}{D} \cdot Re_c^{0.8} \cdot Pr_c^{0.4} \cdot \left(\frac{D_\star}{D}\right)^{0.1} \tag{2.34}$$

Where:

$$\sigma = \frac{1}{\left[\frac{1}{2}\frac{T_{HW}}{T_0}\left(1 + \frac{\gamma-1}{2}M^2\right)\right]^{-0.68}\left(1 + \frac{\gamma-1}{2}M^2\right)^{-0.12}} \tag{2.35}$$

This model was implemented in Thermtest (see chapter 4). Results are presented in chapter 5.

Chapter 3

Subscale liquid rocket combustion chamber

In this chapter the high pressure combustion chamber test facility located at the Institute for Flight Propulsion of TUM will be presented. There will be a general description of the hardware component: the setup for film cooling tests with some geometric main features and operating conditions and also a close-up on the film applicator.

Finally the instrumentation for data collection is presented.

3.1 Combustion chamber

A general sketch of the combustion chamber is given in Figure 3.1.
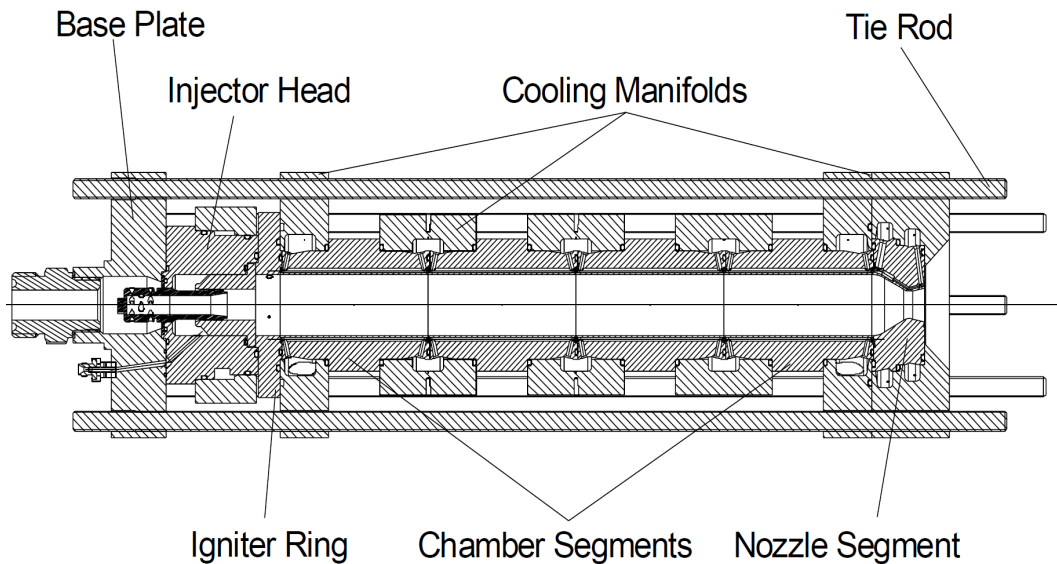
Figure 3.1: Sketch of the sub-scale combustion chamber [40]

The combustion chamber design features a modular setup, that consist in segments of different length, which allows for an easy change of single modules. Alternatively to the four short cylindrical chamber segments, a configuration featuring double length of a short segment is available. By the combination of short and long chamber segments, different values of axial and characteristic length can be realized. The typical setup for film cooling tests feature two short segments and one long

segment and is shown in Figure 3.2. A close-up of the short and long segments is showed in
Figure 3.3.
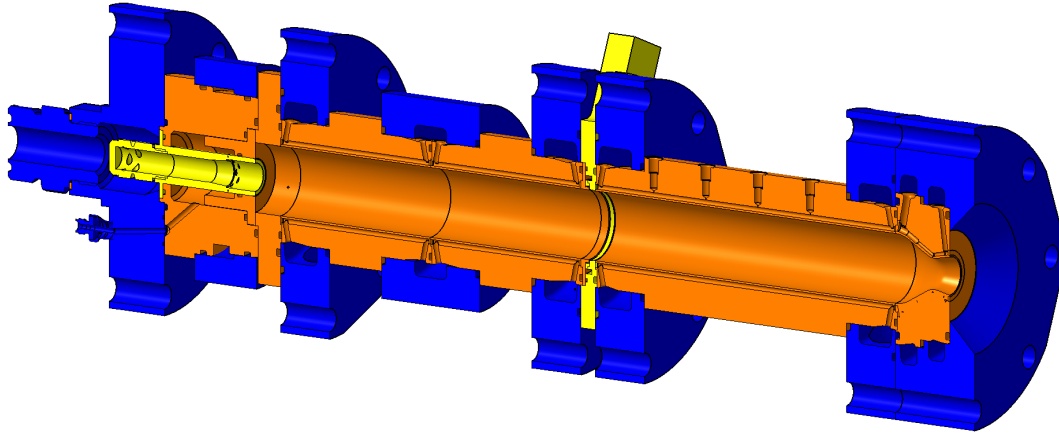
Figure 3.2: Combustion chamber set-up for film cooling tests [39]
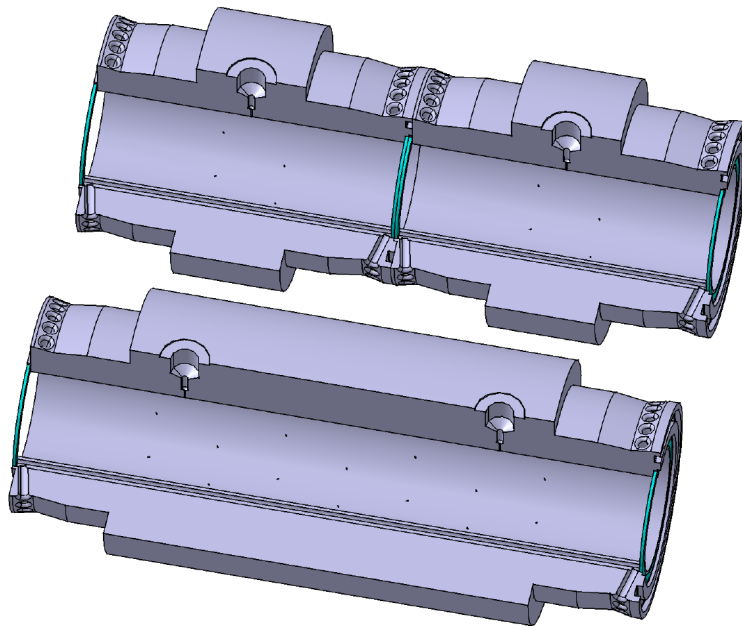
Figure 3.3: Combustion chamber short and long segments close-up [40]

The main geometric parameters of the combustion chamber are shown in Table 3.1. Table 3.2
gives an overview over the nominal operating points and the maximum operating conditions.

Description	Symbol	Value	Unit
Chamber diameter	D_{cc}	37.00	$[mm]$
Throat diameter	D_{th}	16.53	$[mm]$
Contraction ratio	ε_c	5.0	$[-]$
Expansion ratio	ε_e	1.5	$[-]$
Segment length	L_{short}	95.0	$[mm]$
	L_{long}	190.0	$[mm]$
Characteristic length	$L^{\star}$	$0.59 - 1.93$	$[m]$

Table 3.1: Combustion chamber geometric main features

Description	Symbol	Value	Unit
Chamber pressure	$P_{cc,\,nom}$	8.0	$[MPa]$
	$P_{cc,\,max}$	10.0	$[MPa]$
Maximum oxidizer mass flow (GOX)	$\dot{m}_{OX}$	1.00	$\left[\frac{kg}{s}\right]$
Maximum fuel mass flow (JetA-1)	$\dot{m}_F$	0.6	$\left[\frac{kg}{s}\right]$
Mixture ratio	O/F	$1.4 - 3.5$	$[-]$
Combustion temperature	T_{cc}	$2300 - 3800$	$[K]$

Table 3.2: Combustion chamber main operating conditions

Each module can be cooled in two different ways: water-cooled or capacitively-cooled. In the water cooled case and in the the long segment configuration, cooling system is divided into two different cooling cycles:

1. in the first one water flows from the second to the first segment counter-flow and then reaches the nozzle segment where it co-flows with the combustion gases;

2. the second cycle is dedicated in cooling the long segment of the combustion chamber; even in this case water co-flows with combustion gases.

The cooled combustion chamber and nozzle segments are fabricated from oxygen-free copper, which has a certified yield strength of 289.0 MPa; the manifolds are made of high-temperature stainless steel.

3.1.1 Film applicator

The design of the film applicator is derived from a film cooling applicator used in the Russian RD170 engines [39]. Film applicator used in film cooling tests is shown in Figure 3.4. The main advantage is the simple and flexible deployment.

The set-up consists of three parts:

1. an outer ring (base plate), comprising the manifold and feeding system;

2. a ring in the middle (spacer ring), which defines the minimum cross section by number, height and width of the slots;

3. a counter-part (spacer ring), comprising the film lip and space for sealing;

Since the spacer ring is changeable quite easily, the minimum cross section and thus the mass flow rate through the film applicator can be varied by a simple variation of the middle ring. This film cooling applicator provides a radial inflow in the combustion chamber so that the coolant has a swirl motion on the walls.
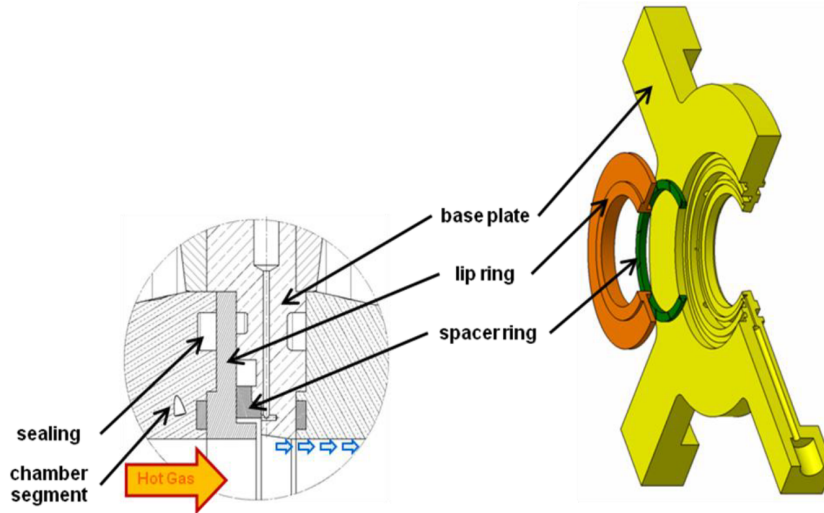
Figure 3.4: Film applicator (sketch and 3D) [40]

The design of the film applicator allows the integration of the tests with a heat sink as well as with the water cooled combustion chamber segments. The two working fluids that are planned to be injected as film coolant are kerosene JetA-1 and water.

3.2   Instrumentation
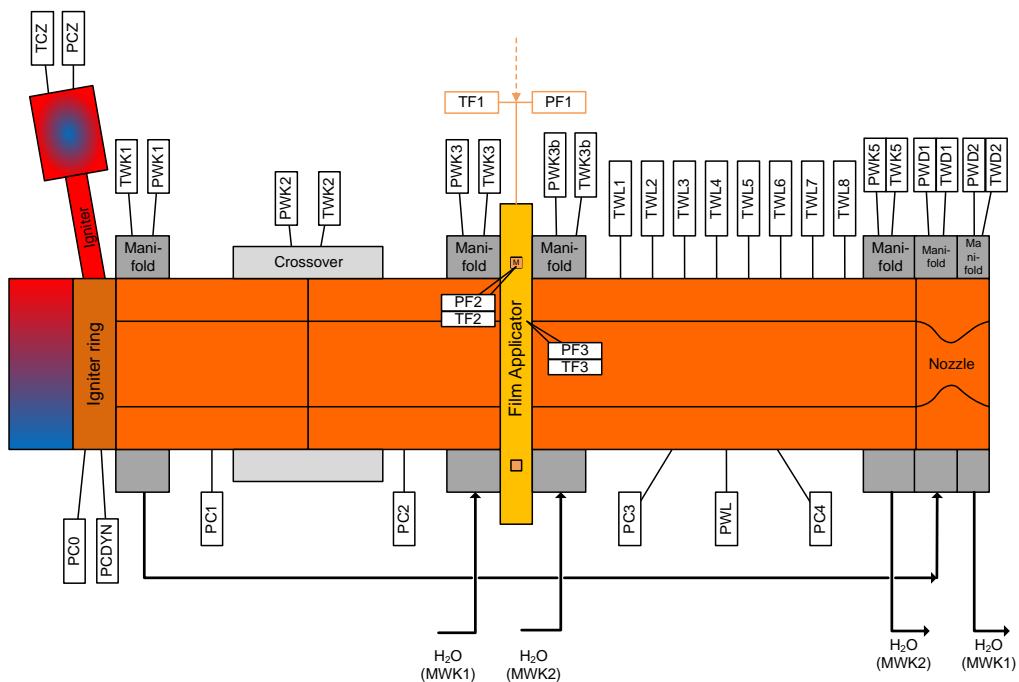
Figure 3.5: Schematic of sensors location [40]

The hot wall temperature measurements featured a higher spatial resolution compared to the heat flux measurements, which integrate heat flux over the length of a whole segment. In the long

segment, for example, there are eight 0.25 *mm* type *K* thermocouples in two adjacent cooling channels as well as three pressure transducers. The limitation to four sensor per channel and to adjacent channels was chosen to avoid a too high blockage and different local heat-ups due to latent circumferential inhomogeneities of the double swirl injector and film applicator respectively.

In addition the experimental set-up is equipped with the standard instrumentation required to characterize the operation of the chamber. A schematic of the combustion chamber and the associated sensors location is given in figure 3.5. Mass flow is recorded by Coriolis mass flow meter in the oxidizer (MO) and in the fuel (MK) feed line. Dynamic pressure transducer (PxxDYN) are also mounted in the oxidizer feed line, the fuel injector manifold, and the combustion chamber wall near the face plate in order to characterize combustion chamber pressure oscillations.

The heat flux to the water-cooled copper chamber segments and the nozzle is calculated by the balance of enthalpy from inlet to outlet of each segment. Coolant temperature (TWKxx) and pressure (PWKxx) are measured after each segment. The coolant mass flow is determined by the differential pressure over a metering orifice.

In order to characterize the injection conditions of the cooling film, pressure and temperature transducers are installed in the film applicator and in the long segment. Coolant mass flow rate is measured with a Coriolis mass flow meter (MF1) calibrated in order to cover the full range of coolant mass flow rates. Pressure and temperature of the coolant fluid are measured upstream of the film applicator inlet (PF1, TF1). In the film applicator pressure and temperature measurements are located in the coolant manifold (PF2, TF2) as well as in the cavity where the film enters the combustion chamber (PF3, TF3).

In figure 3.6 there is a schematic of the combustion chamber, with sensor location, for the tests without film cooling; it is possible to note, in fact, that the film applicator has been replaced by a dummy disk.
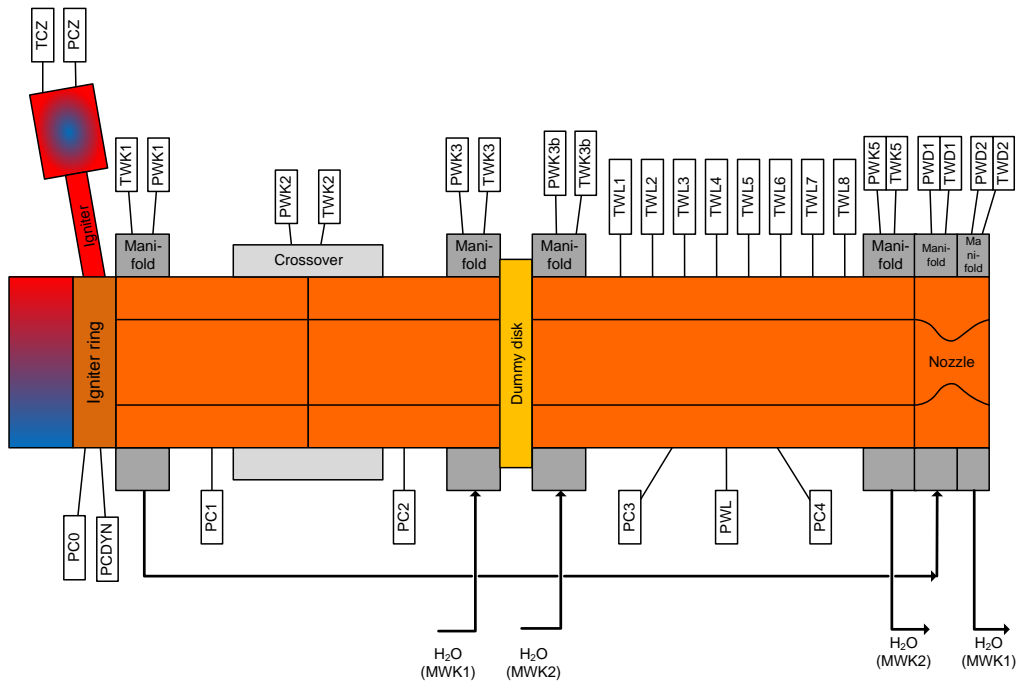
Figure 3.6: Schematic of sensors location for tests without film cooling [40]

3.3   Combustion chamber pictures

In this paragraph a selection of picture illustrating the test bench and some real part of the combustion chamber are presented.
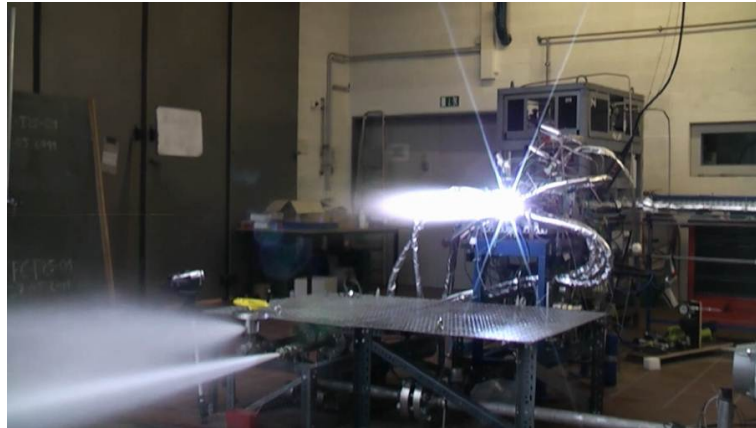
Figure 3.7: TUM test bench during a hot fire test
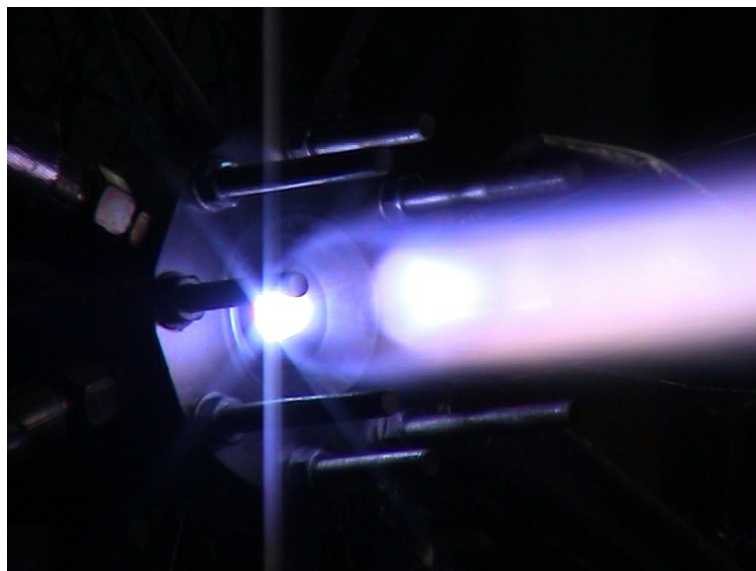
Figure 3.8: Hot fire test example

Figure 3.9: Short segment and injector element

Chapter 4

Thermtest

The knowledge on the mechanism of heat transfer is a very important aspect when designing an experiment for a rocket combustion chamber. Therefore TUM developed a computer program in order to predict and analyze the heat transfer. Thus, in this chapter, Thermtest will be presented. Thermtest is the in-house Matlab written code that predicts the heat transfer of the water-cooled metallic combustion chamber at TUM test facility. This program is mainly used for test preparation and analysis when there is the need of a fast, but also accurate, computation.

4.1 Description

The preparation of the tests on a new cooled combustion chamber requires the capability of computing, before starting the tests, the expected thermal loads on the structure. To do so the convective heat transfer is calculated by semi-empirical Nusselt correlations. The advantage of this approach is a fast solution and prediction of the most important parameters compared to more sophisticated simulation tools, like CFD codes.
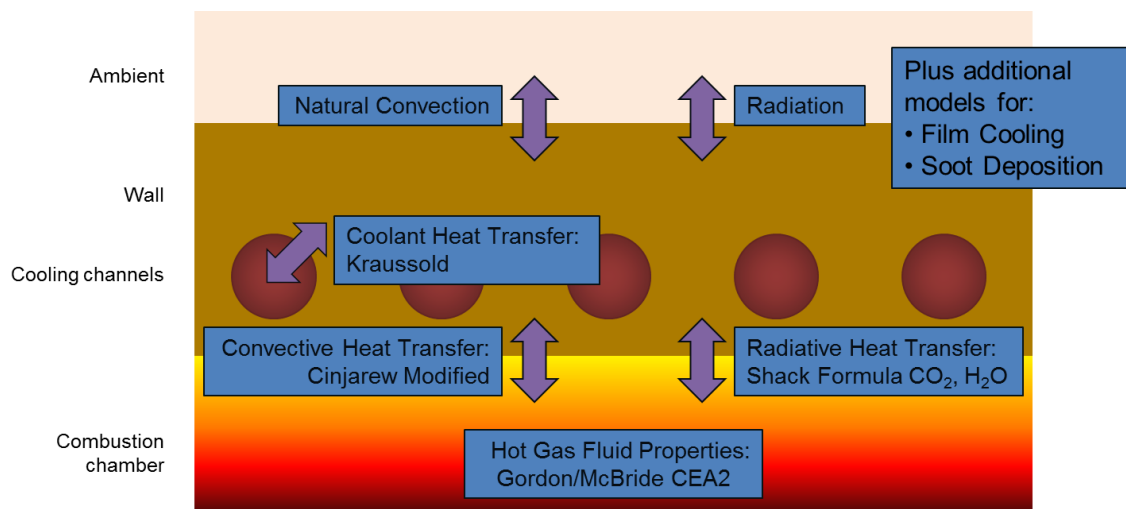
Figure 4.1: Thermtest's heat transfer model ("Common approach")

The heat transfer within the cooled structure of the combustion chamber (see figure 4.1) can be subdivided into these subproblems [28]:

- determination of temperature, pressure, fluid properties and gas composition of the combustion and the hot gas inside the combustion chamber;

- evaluation of the heat transfer, so the heat transfer coefficient at the hot inner chamber wall and at the cold wall. This takes also into account fractions driven by radiation as well as convection;

- calculation of heat conduction in the chamber walls. Effects caused by curvature of walls, fins, holes and cavities, different chamber materials and local heat soak have been considered;

- evaluation of the heat transfer into the coolant. The knowledge of the fluid properties especially in the case of unstable and decomposing coolants might be of great importance;

- evaluation of the heat transfer from the chamber walls to the external ambient.

Other aspects like film and transpiration cooling or soot deposition might be represented likewise within the calculation of the hot gas side heat transfer coefficient.

Furthermore Thermtest features an unsteady thermal transfer model using a FV or FD-like formulation on an arbitrary structured mesh, a fully-3D description of the rocket chamber, which might consist of an arbitrary set of metallic and ceramic materials, and an implicit discretization in time and space, for high robustness.

The "Common approach" utilizes one-dimensional hot gas properties acquired from NASA computer program CEA2 of S. Gordon and B. McBride [33]; the temperature of the fluid and the ideal characteristic velocity are calculated using the built-in rocket problem. In CEA2 the evolution along z-axis is taken into account, but there are not reaction kinetics (that is time for a reaction to happen) so also in Thermtest these aspects are not taken into account. The fluid properties needed for heat transfer calculations near the wall are calculated assuming an aequilibrium composition for the temperature-pressure problem.

As stated before, the convective heat transfer from the hot gas to the inner wall and from the wall to the coolant is modeled using Nusselt correlations.

The hot wall heat transfer coefficient is calculated from a modified formulation proposed by Cinjarew:

$$Nu = 0.0162 \cdot (Re \cdot Pr)^{0.82} \cdot \left(\frac{T_{HG}}{T_W} \right)^{0.35} \tag{4.1a}$$

$$\alpha_{HG,\,conv} = 0.01975 \cdot \frac{\lambda^{0.18} \left(\dot{m} c_p \right)^{0.82}}{D^{1.82}} \cdot \left(\frac{T_{HG}}{T_W} \right)^{0.35} \tag{4.1b}$$

Where values of viscosity, specific heat and conductivity are computed at the mean temperature $T_{mean} = 0.5 \cdot (T_{HG} + T_W)$ rather than hot wall temperature T_W as in the original formula.

The temperature of the hot gas is the so called recovery temperature that takes into account imperfect combustion and incomplete heat recovery:

$$T_{HG} = T_{HG,static} + \delta \left(T_{th,\,combustion} \cdot \eta_{c*}^2 - T_{HG,static} \right) \tag{4.2}$$

Where δ is the empirical recovery factor varying from 0.7 to 0.9 depending on the gas Prandtl number and the boundary layer type. The value used in Thermtest is 0.8, which was found to be conservative but realistic.

The throat heat transfer coefficient is corrected with an empirical factor to take into account local overspeed and turbulence effects.

Thermtest also takes into account heat transfer by radiation especially because the wall temperature is high. Assuming that the effective outer diameter of the imaginary cylinder filled up with hot gas is virtually equal to the inner chamber diameter a heat transfer coefficient for radiation can be defined in the following way:

$$\alpha_{HG,\,rad} = \frac{\sigma_S}{\left(\frac{1}{\varepsilon_W} + \frac{1}{\varepsilon_{HG}} - 1 \right)} \left(T_W + T_{HG} \right) \left(T_W^2 + T_{HG}^2 \right) \tag{4.3}$$

Where $\sigma_S = 5.67 \cdot 10^{-8} \frac{W}{m^2 K^4}$.

For the determination of the emissivity of the hot gas a convenient approach is the empirical formulation by Shack [32]. For water and carbon dioxide following equations are given for the thermal heat flux:

$$q_{rad, H_2O} = 5.74 \cdot (P_{cc} \cdot r_{cc})^{0.3} \left(\frac{T_{gas}}{100} \right)^{3.5} \tag{4.4}$$

$$q_{rad, CO_2} = 4 \cdot (\mu_{CO_2} P_{cc} \cdot r_{cc})^{0.3} \left(\frac{T_{gas}}{100} \right)^{3.5} \tag{4.5}$$

In order to calculate heat transfer from the chamber wall into the cooling channel one of the available formulation for the fluid in pipes can be used. In Thermtest a model by Kraussold [33] is implemented:

$$\alpha_{CF} = 0.024 \cdot \frac{c_p^{0.37} \lambda^{0.63}}{\eta^{0.43} D^{0.2}} \cdot \left(\frac{\dot{m}}{\frac{\pi}{4} D^2} \right)^{0.8} \tag{4.6}$$

4.1.1 Geometry
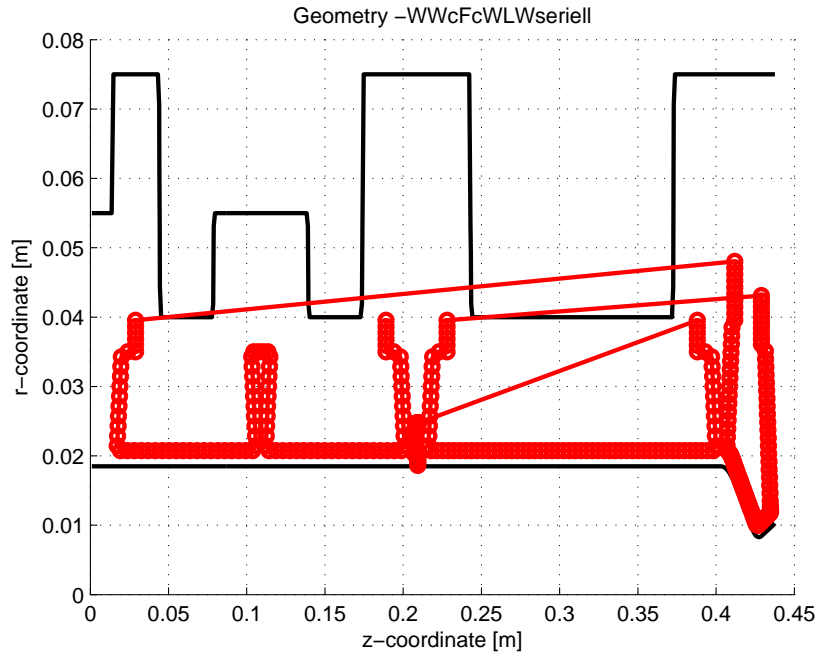
Figure 4.2: Example of 2D Thermtest geometry with cooling circuit

The geometry of the combustion chamber implemented in Thermtest is three-dimensional; the cooling mesh is instead two-dimensional. The mesh is created by a dedicated script and is highly modifiable. The entire geometry includes the manifolds and the water cooling system (the red lines in figure 4.2). Different materials properties are implemented in Thermtest, so it is possible to modify the material of every single region.

4.1.2 Solid and fluid properties

The main properties of the materials and of the working fluids are implemented in Matlab files. The stored properties are density, specific heat and conductivity. JetA-1 and gaseous oxygen are characterized by properties for many pressures and temperatures, in order to get the desired property at the desired pressure and temperature through an interpolation. In particular the kerosene fluid properties are derived from Rachner [37].

The one-dimensional hot gas properties, as stated before, have been acquired from the NASA CEA2 computer program [33].

4.1.3   Solving method

Thermtest solves the various differential equation with a sort of finite difference method creating a sparse coefficients matrix that is solved with an optimized Matlab numerical method.
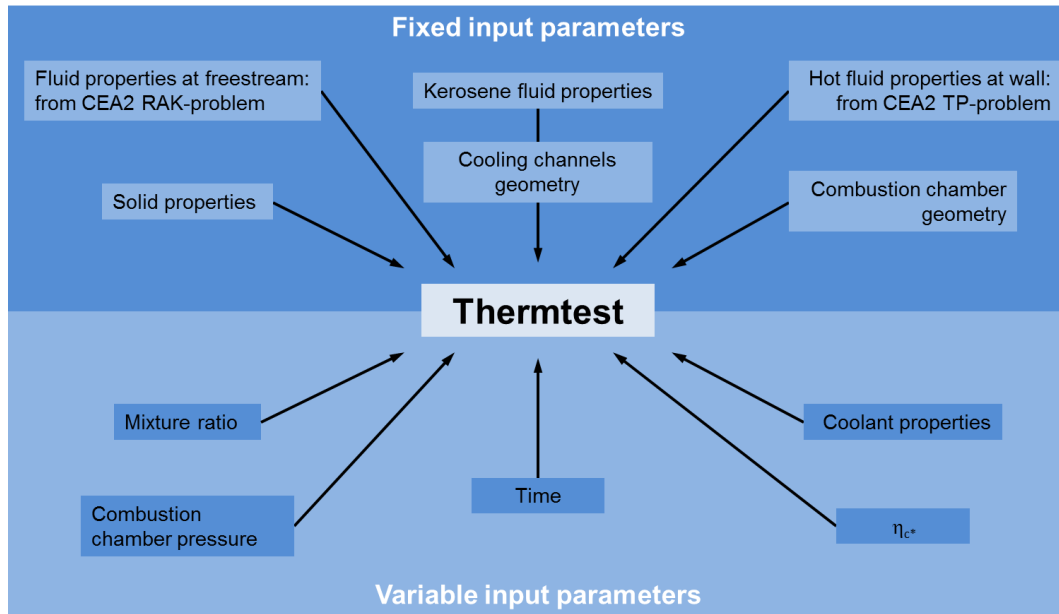
Figure 4.3: Thermtest input parameters

The input parameters for Thermtest are summarized in figure 4.3. It is possible to divide this inputs in fixed and variable. The fixed parameters, common to several simulations, are:

- combustion chamber geometry and materials,

- cooling channels geometry,

- coolant properties (water for the regenerative cycle),

- freestream fluid properties, that are acquired from the solution of the RAK-problem with CEA2,

- hot wall fluid properties, calculated with the CEA2 TP-problem.

The variable input parameters, instead, are defined by the user according to which test has to be simulated, they could be different between each test and are:

- mixture ratio $^O/_F$,

- combustion chamber pressure P_{CC},

- type of film coolant and therefore its properties,

- combustion efficiency η_{c^*},

- duration of the simulation and length of the timesteps.

Once that these parameters are given, Thermtest enters a solving loop that is given in figure 4.4.
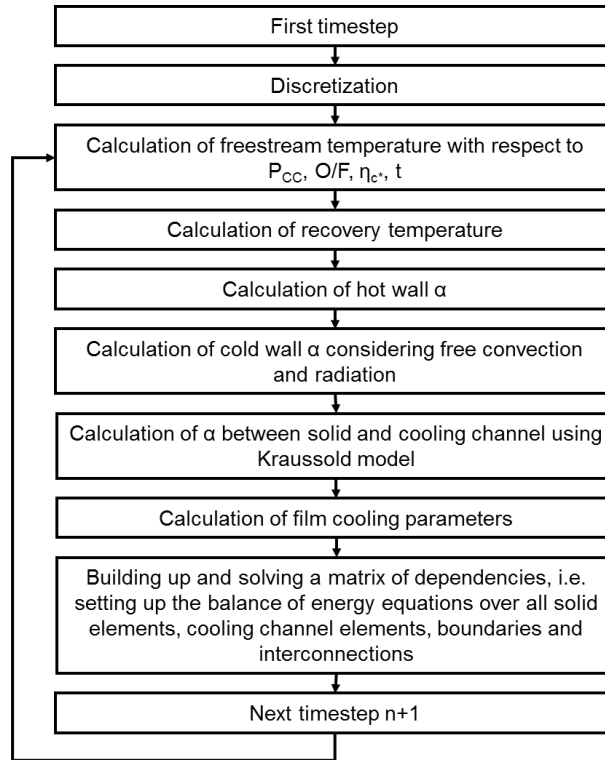
Figure 4.4: Thermtest solving procedure

After loading all the important parameters like mesh file for the geometry, gas, coolant and solid property tables, Thermtest enters the solving loop. After that it begins the discretization and, using the combustion chamber pressure, the mixture ratio and the combustion efficiency, calculates the freestream temperature. Then the recovery temperature and the static hot gas temperature are calculated. Now, using one of the models described in chapter 2.3, the hot wall heat transfer coefficient (α) is calculated; then considering free convection and radiation Thermtest calculates the cold wall α and using the Kraussold model (see equation 4.6) the heat transfer coefficient between solid and cooling channels is obtained. If film cooling is considered, Thermtest calculates now the important parameters of film cooling, like the effectiveness or the film cooled length, with one of the models implemented (see section 4.2 or 2.4.1 for the descriptions of the models). Finally the program generates and solves a matrix of dependencies, calculating the energy balance for example, and prepares itself for the next timestep.

The Thermtest output parameters are:

- combustion chamber temperature, function of time, radial, angular and axial coordinates,

- cooling fluid temperature, function of time and axial coordinate,

- cooling fluid pressure,

- hot and cold wall heat flux, function of time and axial coordinate,

- maximum wall temperature.

4.2 Actual film cooling model: NASA A & B

A film cooling model gives an assessment of the main film cooling process parameters, such as effectiveness, entrainment ratio or film cooled length.

The actual film cooling models implemented in Thermtest are described in Appendix A (for gaseous film cooling) and B (for liquid film cooling) of NASA SP-8124 [10]. In both models the entrainment flux of core flow into a mixing layer containing all the film coolant is equal to the product of the core axial mass velocity and an entrainment fraction. The coolant effectiveness is defined in terms of total enthalpy and it is a function of the entrained flow, coolant flow and a shape factor for the mixing layer profile. Adiabatic wall temperatures may be obtained with a reactive or a non-reactive model.

4.2.1   NASA A - Analytical model for gaseous film cooling

The first value that has to be calculated with this model is the entrained flow ratio $\frac{W_e}{W_c}$. The entrainment is a phenomenon occurring when one fluid in motion pushes or pulls another fluid along with it. In this model the entrained ratio is defined as the ratio between entrained flow and film coolant mass flow rate.

$$\frac{W_e}{W_c} = \frac{W - W_c}{W_c} \left[2\frac{\psi_r \cdot \overline{z}}{r_i - s_i} - \left(\frac{\psi_r \cdot \overline{z}}{r_i - s_i} \right)^2 \right] \tag{4.7}$$

where:

- W_e is the entrained flow rate,

- W_c is the coolant flow rate,

- W is the total combustion chamber flow rate,

- $\overline{z}$ is the effective contour distance

$$\overline{z} = \int_{z_1}^{z} \frac{r_c}{r_{c_i}} \frac{(\rho_e u_e)_{2D}}{(\rho_e u_e)_{1D}} \psi_m dz \tag{4.8}$$

- ψ_r is the reference entrainment factor

$$\psi_r = \frac{0.1\frac{u_c}{u_e}}{\left(\frac{\rho_c}{\rho_e} \right)^{0.15} \left(\frac{\rho_c u_c s_i}{\eta_c} \right)^{0.25} f\left(\frac{u_c}{u_e} \right)} \tag{4.9}$$

- s is the mixing layer length

- ψ_m is the empirical entrainment factor multiplier, that takes into account rocket turbulence levels, coolant injection configuration, flow turning and acceleration. Reference [43] suggests a value of $\psi_m = 3 \div 4$ at the injection point, decaying linearly with axial distance to 1.75 at the throat.

- $f\left(\frac{u_c}{u_e} \right)$ from figure 4.5

It could be seen that the entrainment ratio is a function of the total flow rate in the combustion chamber, of the film coolant flow rate, of the mixing layer length and of a reference entrainment factor.

After the entrained flow ratio calculation the film cooling effectiveness, that is a function of the entrained flow ratio, can be found thanks to the figure 4.6.

$$\eta = \eta \left(\frac{W_e}{W_c} \right) \tag{4.10}$$

This function could be approximated as:

$$\eta = \frac{1.32}{1 + W_e/W_c} \qquad if \qquad \frac{W_e}{W_c} > 1.4$$

$$\eta = 1 \qquad if \qquad \frac{W_e}{W_c} > 0.06 \tag{4.11}$$
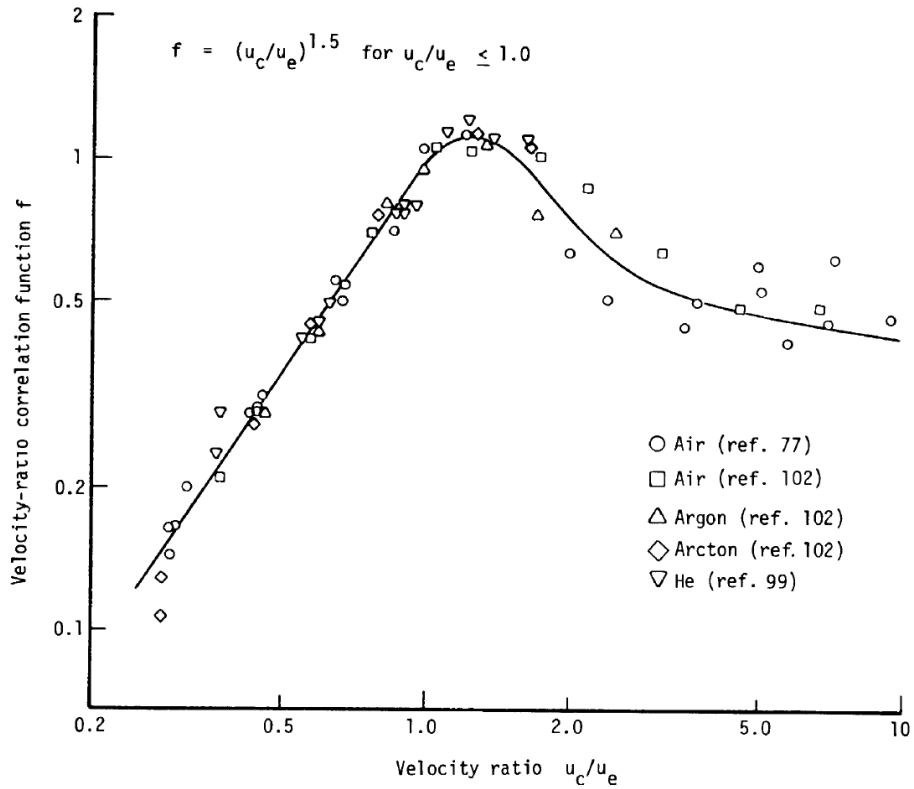
Figure 4.5: Velocity ratio correlation function $f\left(\frac{u_c}{u_e}\right)$ [10]
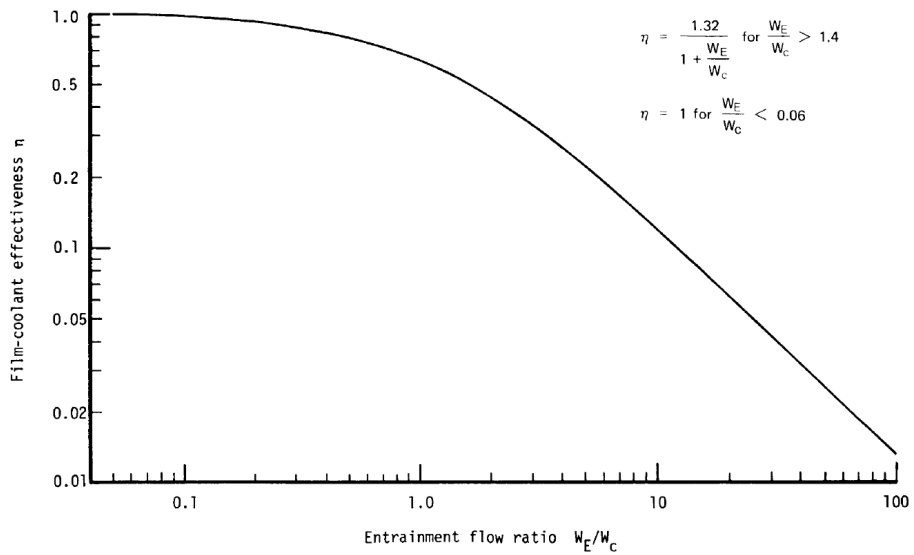
Figure 4.6: Film cooling effectiveness η [10]

The adiabatic wall enthalpy is a function of the total and static core flow enthalpy, the coolant static enthalpy, the effectiveness and the Prandtl number.

$$h_{aw} = h_{tot,e} - \eta\left(h_{tot,e} - h_c\right) - \left(1 - Pr_w^{0.333}\right) \cdot \left(h_{tot,e} - h_e\right) \tag{4.12}$$

NASA A model also calculates the mixture ratio in the wall's proximity:

$$(O/F)_w = \frac{1 + (O/F)_e}{1 + \eta \left(\frac{1 + (O/F)_e}{1 + (O/F)_c} - 1 \right)} - 1 \tag{4.13}$$

Finally, regarding the calculation of the adiabatic wall temperature, the model gives two different possibilities: one consider a reactive model, the other a non reactive one.

For the reactive model the adiabatic wall temperature can be obtained from a reactive thermochemical analysis like the one in [33].

$$T_{aw} = T\left((O/F)_w, \ H_{aw} \right) \tag{4.14}$$

The non reactive model, instead, does not take into account the real thermochemical process:

$$T_{aw} = T_{tot,e} - \frac{\eta c_{p_c} (T_{tot,e} - T_c) + \left(1 - Pr_w^{0.333}\right) \cdot (h_{tot,e} - h_e)}{\eta c_{p_c} + (1 - \eta) c_{p_e}} \tag{4.15}$$

4.2.2 NASA B - Analytical model for liquid film cooling

In this model for liquid film cooling the first quantity that is calculated is the liquid film cooled length (L). This length is defined as the distance beyond which the film ceases to exist.

$$L = \frac{1}{A} \ln \left(1 + \frac{A \cdot W_c}{V} \right) \tag{4.16}$$

where:

- $A = A(X_e)$ is the liquid entrainment parameter (expressed in $\left[in^{-1} \right]$) from figure 4.7,
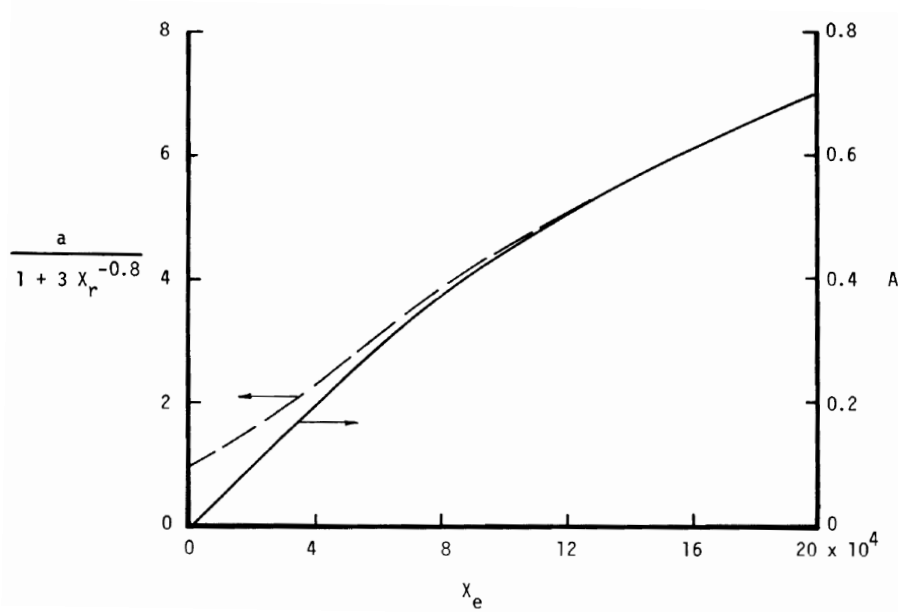
Figure 4.7: Liquid entrainment parameter A [10]

- X_e is the liquid entrainment correlation parameter; it is a function of the ratio between the core flow (T_e) and the liquid interface temperature (T_{if}), of an empirical entrainment augmentation factor (δ), to account for coolant injection effects in rocket applications, of the core flow density (ρ_e) and velocity (u_e) and of the surface tension (σ); all this quantities must

be expressed in the american units system:

$$X_e = \frac{\delta \left(\rho_e/g\right)^{0.5} u_e \left(T_e/T_{if}\right)^{0.25}}{\sigma}$$ (4.17)

- W_c is the film coolant flow rate in $^{lbm}/_s$,

- D is the combustion chamber diameter in in

- V is the vaporization rate of the liquid surface:

$$V = \pi \frac{\rho_e u_e}{144} D \cdot St \cdot B \cdot a$$ (4.18)

- B is a parameter defined as the ratio between the total and static core flow enthalpy difference and the difference between the static enthalpy of the coolant saturated vapor and the static enthalpy of the coolant:

$$B = \frac{h_{tot,e} - h_e}{h_{c,sat\,vap} - h_c}$$ (4.19)

- a is an heat transfer augmentation factor for liquid surface roughness (from figure 4.7),

- $X_r = \sigma \cdot X_e$ is the liquid film surface roughness parameter,

- $St = 0.318 \cdot Re_w^{-0.5} \cdot Pr_w^{-0.6}$,

After calculating the film cooled length, NASA B model gives an expression for the calculation of the film cooling effectiveness:

$$\eta = \frac{1}{\theta \left(1 + \frac{W_e}{W_c}\sqrt{1 - \frac{W_{eL}}{W - W_c}} - \left(\psi_r \frac{\bar{z}}{r_i}\right)^2\right)}$$ (4.20)

The film cooling effectiveness is then a function of the mass flows of both the main core and of the coolant flow, of the entrainment factor for plane, unaccelerated flow with continuous slot injection (ψ_r) and of the parameter $\bar{z}$ defined in equation 4.8 (this time the integration starts when $z = L$).

To achieve the film cooling effectiveness calculation it is necessary to determine the entrainment flow ratio ($^{W_e}/_{W_c}$) and the shape factor for the mixing layer profile (θ).

The expression for the entrainment flow ratio is:

$$\frac{W_e}{W_c} = \frac{W - W_c}{W_c}\left(2\psi_r \frac{\bar{z}}{r_i}\right) + \frac{W_{eL}}{W_c}$$ (4.21)

where:

- for ψ_r, the entrainment factor for plane, unaccelerated flow with continuous slot injection, rocket data analysis suggest a value between 0.025 and 0.06,

- $\frac{W_{eL}}{W_c} = \frac{1}{0.6\eta_L} - 1$,

- $\eta_L = \frac{B}{1+B}$.

The shape factor θ, instead, is a function of the core and coolant mass flows:

$$\theta = 0.6 + 0.263\frac{W_e - W_{eL}}{W_c} \qquad for \qquad W_e < W_{eL} + 0.6W_c$$

$$\theta = 0.758 \qquad for \qquad W_e \geq W_{eL} + 0.6W_c$$ (4.22)

NASA B model also proposes a formula to calculate the adiabatic wall temperature that is determined by a mixing layer entrainment model similar to that for gaseous film cooling, so in this formula there is not a thermochemical analysis.

$$T_{aw} = \frac{H_{aw} - \eta H_{c,sv} + \eta c_{p_v} T_{if} + (1 - \eta)\left(c_{p_e} T_{tot,e} - h_e\right)}{\eta c_{p_v} + (1 - \eta)\,c_{p_e}} \tag{4.23}$$

c_{p_v} is the specific heat of the vapor and for its assessment it is possible to use the model from CEA2 [33]:

$$\frac{c_{p_v}}{R} = a_1 T_c^{-2} + a_2 T_c^{-1} + a_3 + a_4 T_c + a_5 T_c^2 + a_6 T_c^3 + a_7 T_c^4 \tag{4.24}$$

where:

- R is the universal gas constant,
- $a_1 = -4.22 \cdot 10^5$,
- $a_2 = -5.58 \cdot 10^3$,
- $a_3 = 1.52 \cdot 10^2$,

- $a_4 = -8.61 \cdot 10^{-1}$,
- $a_5 = 3.07 \cdot 10^{-3}$,
- $a_6 = -4.70 \cdot 10^{-6}$,
- $a_7 = 2.74 \cdot 10^{-9}$.

The last value that we need to calculate for the determination of the adiabatic wall temperature is the adiabatic wall enthalpy:

$$h_{aw} = h_{tot,e} - \eta\left(h_{tot,e} - h_c\right) - \left(1 - Pr_w^{0.333}\right)\left(h_{tot,e} - h_e\right) \tag{4.25}$$

It could be seen that is a function of the core flow and coolant enthalpies and of the wall Prandtl number.

Chapter 5

Experimental and numerical results

In this chapter the experimental results from the subscale combustion chamber of TUM-LFA, described in chapter 3, will be presented. Focusing on peculiar load points, a comparison between experimental and numerical results will be presented. Implementation of different heat transfer coefficient and film cooling models (chapter 2.3 and 4) will be compared in order to find out which one gives the best approximation of the experimental heat fluxes for specific load points.

5.1 Experimental results

5.1.1 Analyzed load points

The analyzed load points were chosen in order to range over different values of pressure, mixture ratio and film cooling flow rate between the huge amount of experimental data available. In the experimental results the studied pressures are 20, 40, 60 and 80 bar. For each of these pressures four values of mixture ratio and film cooling flow rate were considered. Three out of four are "real" experimental load points, first one without film cooling and the other two with a variable amount of film cooling, the last one is an "artificial" load point with all the characteristics and values of one of the two film cooled load points but with a mixture ratio reduced by 10%. It could be possible in fact, that the combustion chamber injector does not provide a constant mixture ratio for cross section of the combustion chamber. With this 10% reduction we simulate that the injector provides a reduced, but constant, mixture ratio in each section.

In the next tables, for every combustion chamber pressure (PCC), mixture ratio (OF), film coolant mass flow (μ, see equation 5.1), as a percentage of the total kerosene mass flow injected in the chamber, combustion chamber temperature (T_{HG}), calculated with CEA 2 computer program [33], and blowing ratio, from equation 5.2, will be presented. In the last column of these tables there is the identification of that particular load point. This ID will be used from now on.

$$\mu = \frac{\dot{m}_{film}}{\dot{m}_{film} + \dot{m}_{fuel}} \tag{5.1}$$

$$F = \frac{M_f}{M_{tot}} \cdot \frac{A_{ref_{CC}}}{A_{ref,\,cooling\,channels}} \tag{5.2}$$

where:

- M_f is the film coolant mass flow,

- M_{tot} is the total kerosene mass flow injected in the chamber (fuel and film coolant),

- $A_{ref_{CC}}$ is the combustion chamber reference area:

$$A_{ref_{CC}} = \pi \left(\frac{D_{CC}}{2} \right)^2 = \pi \left(\frac{37\,mm}{2} \right)^2 = 0.001075\,m^2$$

- $A_{ref_{cooling\,channels}}$ is the reference area of the cooling channels:

$$A_{ref_{cooling\,channels}} = \pi \cdot D_{CC} \cdot s_{FA} = \pi \cdot 37\,mm \cdot 0.5\,mm = 5.8119 \cdot 10^{-5}\,m^2$$

- $s_{FA} = 0.5\,mm$ is the film applicator gap.

Obviously blowing parameter F is not defined for the load points without film cooling.

PCC [bar]	OF [$-$]	μ [%]	T_{HG} [K]	F [$-$]	ID
	3.22	0	3398	-	20-322-0
20	2.88	10	3460	0.3975	20-288-10
	3.41	20	3438	1.1322	20-341-20
	3.07	20	3438	1.1322	20-307-20

Table 5.1: 20 bar load points

PCC [bar]	OF [$-$]	μ [%]	T_{HG} [K]	F [$-$]	ID
	3.22	0	3523	-	40-322-0
40	2.88	5	3566	0.2685	40-288-5
	3.22	15	3561	0.7437	40-322-15
	2.90	15	3561	0.7437	40-290-15

Table 5.2: 40 bar load points

PCC [bar]	OF [$-$]	μ [%]	T_{HG} [K]	F [$-$]	ID
	2.88	0	3601	-	60-288-0
60	3.22	10	3628	0.5200	60-322-10
	3.22	15	3634	0.7730	60-322-15
	2.90	10	3628	0.5200	60-290-10

Table 5.3: 60 bar load points

PCC [bar]	OF [$-$]	μ [%]	T_{HG} [K]	F [$-$]	ID
	2.88	0	3663	-	80-288-0
80	3.05	10	3685	0.5240	80-305-10
	3.22	15	3679	0.7854	80-322-15
	2.75	10	3685	0.5240	80-275-10

Table 5.4: 80 bar load points

5.1.2   Experimental heat fluxes

The test apparatus for obtaining the experimental heat fluxes data was structured in this way:

- injector and igniter ring (from 0 to 16 mm), two short segments (95 mm each, from 16 mm to 206 mm), then the film applicator (from 206 mm to 215 mm), the long segment (from 215 mm to 405 mm) and the nozzle (from 405 mm to 439.1 mm),

- first two segments were only regeneratively cooled, no film coolant was present,

- long segment and nozzle were cooled with both regeneratively and film cooling,

- film cooling was achieved injecting kerosene Jet-A1 at the beginning of the long segment, in order to be sure that almost all chemical reaction were completed. In this way one of the possible sources of error would not be taken into account,

- combustion chamber burned gaseous oxygen and kerosene Jet-A1.

Experimental heat fluxes are presented, in table 5.5, as integral values along each of the four segments with their respective standard deviation. These values come from averaging the heat fluxes of several tests and they are also time-averaged.

ID	Heat fluxes $[W/m^2]$			
	Segment 1	Segment 2	Long Segment	Nozzle
20-322-0	$7.802 \cdot 10^6 \pm 2.5\%$	$8.457 \cdot 10^6 \pm 1.6\%$	$6.397 \cdot 10^6 \pm 2.0\%$	$1.0489 \cdot 10^7 \pm 10.2\%$
20-288-10	$6.276 \cdot 10^6 \pm 2.0\%$	$8.219 \cdot 10^6 \pm 0.4\%$	$4.730 \cdot 10^6 \pm 2.0\%$	$1.097 \cdot 10^7 \pm 0.5\%$
20-341-20	$8.865 \cdot 10^6 \pm 1.7\%$	$8.302 \cdot 10^6 \pm 0.6\%$	$3.556 \cdot 10^6 \pm 12.3\%$	$1.019 \cdot 10^7 \pm 9.3\%$
20-307-20	$8.865 \cdot 10^6 \pm 1.7\%$	$8.302 \cdot 10^6 \pm 0.6\%$	$3.556 \cdot 10^6 \pm 12.3\%$	$1.019 \cdot 10^7 \pm 9.3\%$
40-322-0	$1.292 \cdot 10^7 \pm 4.1\%$	$1.556 \cdot 10^7 \pm 1.7\%$	$1.211 \cdot 10^7 \pm 1.0\%$	$1.792 \cdot 10^7 \pm 20.1\%$
40-288-5	$1.089 \cdot 10^7 \pm 2.9\%$	$1.495 \cdot 10^7 \pm 1.2\%$	$9.139 \cdot 10^6 \pm 7.1\%$	$1.659 \cdot 10^7 \pm 10.7\%$
40-322-15	$1.289 \cdot 10^7 \pm 1.5\%$	$1.545 \cdot 10^7 \pm 1.1\%$	$7.468 \cdot 10^6 \pm 12.0\%$	$1.561 \cdot 10^7 \pm 14.4\%$
40-290-15	$1.289 \cdot 10^7 \pm 1.5\%$	$1.545 \cdot 10^7 \pm 1.1\%$	$7.468 \cdot 10^6 \pm 12.0\%$	$1.561 \cdot 10^7 \pm 14.4\%$
60-288-0	$1.287 \cdot 10^7 \pm 6.8\%$	$2.095 \cdot 10^7 \pm 4.3\%$	$1.662 \cdot 10^7 \pm 4.4\%$	$3.453 \cdot 10^7 \pm 15.9\%$
60-322-10	$1.592 \cdot 10^7 \pm 2.8\%$	$2.088 \cdot 10^7 \pm 2.1\%$	$1.104 \cdot 10^7 \pm 3.3\%$	$2.974 \cdot 10^7 \pm 11.1\%$
60-322-15	$1.567 \cdot 10^7 \pm 5.2\%$	$2.095 \cdot 10^7 \pm 0.3\%$	$9.139 \cdot 10^6 \pm 3.4\%$	$3.092 \cdot 10^7 \pm 3.6\%$
60-290-10	$1.592 \cdot 10^7 \pm 2.8\%$	$2.088 \cdot 10^7 \pm 2.1\%$	$1.104 \cdot 10^7 \pm 3.3\%$	$2.974 \cdot 10^7 \pm 11.1\%$
80-288-0	$1.545 \cdot 10^7 \pm 6.7\%$	$2.537 \cdot 10^7 \pm 2.2\%$	$2.018 \cdot 10^7 \pm 2.9\%$	$4.555 \cdot 10^7 \pm 10.8\%$
80-305-10	$1.574 \cdot 10^7 \pm 1.5\%$	$2.495 \cdot 10^7 \pm 1.4\%$	$1.330 \cdot 10^7 \pm 6.4\%$	$4.358 \cdot 10^7 \pm 11.8\%$
80-322-15	$1.753 \cdot 10^7 \pm 3.3\%$	$2.538 \cdot 10^7 \pm 1.9\%$	$1.156 \cdot 10^7 \pm 8.4\%$	$4.361 \cdot 10^7 \pm 9.1\%$
80-275-10	$1.574 \cdot 10^7 \pm 1.5\%$	$2.495 \cdot 10^7 \pm 1.4\%$	$1.330 \cdot 10^7 \pm 6.4\%$	$4.358 \cdot 10^7 \pm 11.8\%$

Table 5.5: Experimental heat fluxes

5.2 Numerical results

This paragraph provides plots and histograms of the numerical results obtained running several simulation with Thermtest.

The inputs that Thermtest need to simulate correctly one load point are:

- chamber pressure,

- mixture ratio,

- type of fluid and oxidizer,

- length of the simulation (for these numerical results 60 *s* was always used),

- pressure, temperature and mass flux of the cooling fluid, water in our cases, used for the convective cooling of the combustion chamber,

- pressure, temperature, mass flux and type of film coolant,

- type of mesh file, that describes the geometry of the combustion chamber[1],

- film cooling model,

---

[1]This is due to different rooting of the convective cooling channels in the 20 bar test cases compared to 40, 60 and 80 bar load points. A different geometry mesh file is also used in no film cooling load points: in these cases the film cooling applicator is replaced by a dummy disk.

- hot wall heat transfer coefficient model.

Regarding the film cooling model, NASA B model for liquid film cooling (see 4.2.2) is considered as the baseline; Stechman film cooling model (see 2.4.1) was also investigated.

For hot wall heat transfer coefficient, instead, it is possible to choose between the six different correlation presented in 2.3; in addition to these, as a reference point, simulation were also conducted with the standard hot wall heat transfer correlation developed by Cinjarew [42] declined into two different connotations: first one is Cinjarew model modified with a custom TUM-LFA correction and second one is the pure Cinjarew model without any modification.

TUM-LFA correction consists firstly in correlate experimental data figuring that they depend only by mixture ratio and combustion chamber pressure [25]:

$$q = a \cdot OF^b \cdot PCC^c \tag{5.3}$$

After that also the error Δq between correlated heat flux and Thermtest results is expressed in the same form. An optimization is carried on to find the constants x, y and z that minimize the error.

$$\Delta q = x \cdot OF^y \cdot PCC^z \tag{5.4}$$

5.2.1   NASA B liquid film cooling model

5.2.1.1   Qualitative assessment of the local hot wall heat fluxes

In this section the qualitative assessment of the hot wall heat fluxes for all the analyzed load points will be presented. In each plot the results from the eight different hot wall heat transfer models are shown and also the experimental values are plotted as a comparison.

20 bar

Figures 5.1, 5.2, 5.3 and 5.4 show the simulated hot wall heat fluxes for the load points presented in table 5.1.

Figure 5.1: Punctual hot wall heat flux - 20-322-0

Figure 5.2: Punctual hot wall heat flux - 20-288-10

Figure 5.3: Punctual hot wall heat flux - 20-341-20

Figure 5.4: Punctual hot wall heat flux - 20-307-20

As it is possible to see in these pictures in the first two segments ($0 < z < 0.2\ m$) simulated heat fluxes are more or less closer to the experimental values. After that there is a modelling issue due to the presence of the gap between the hot lip and the film applicator; in the load point without film cooling we have a significantly lower peak because the film applicator is replaced with a dummy disk. In the third and nozzle segment the models begin to differ from each others: Cinjarew model is the closest to the experimental values, Swenson is the worst one, badly overpredicting the experimental heat fluxes; all the other models are in the middle but still overpredicting. Moreover comparing the last two figures it is possible to note that although the simulated heat fluxes are closer to the experimental values in the case with the OF reduction (figure 5.4), the new heat transfer models are still overestimating them. The variable length plateau, that is noticeable just after the film applicator, is the liquid film cooled length; as expected it increases as the film coolant mass flow rate increases.

40 bar

Figures 5.5, 5.6, 5.7 and 5.8 show the simulated hot wall heat fluxes for the load points presented in table 5.2.
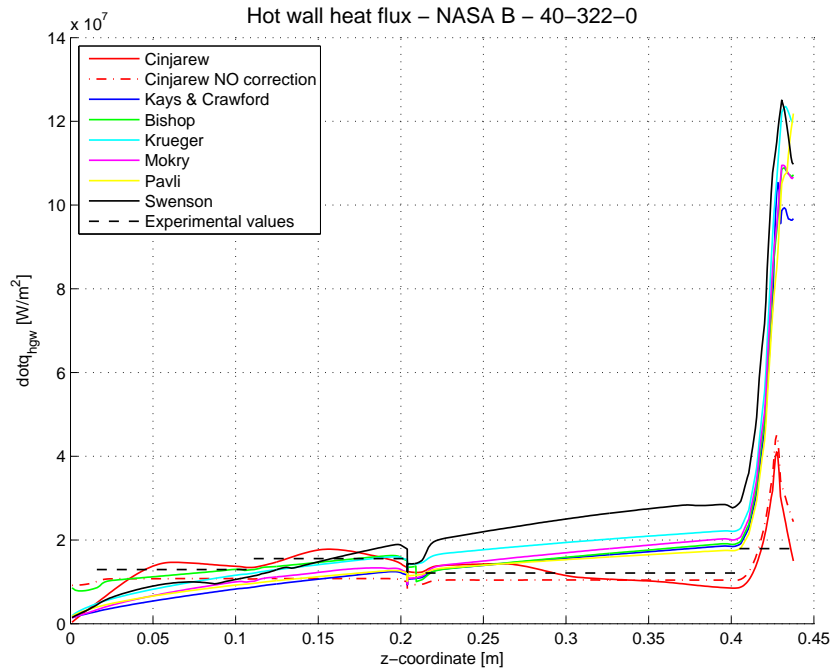
Figure 5.5: Punctual hot wall heat flux - 40-322-0
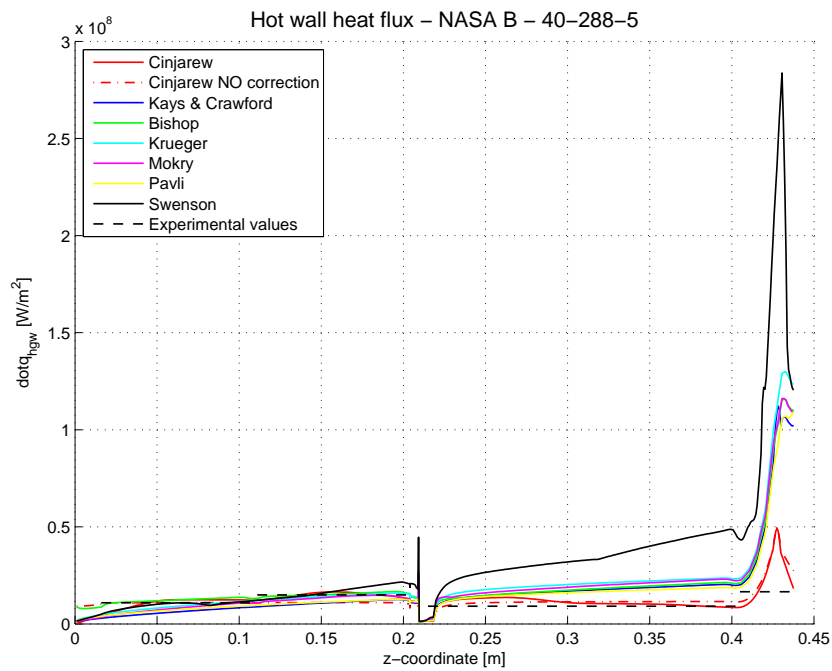
Figure 5.6: Punctual hot wall heat flux - 40-288-5
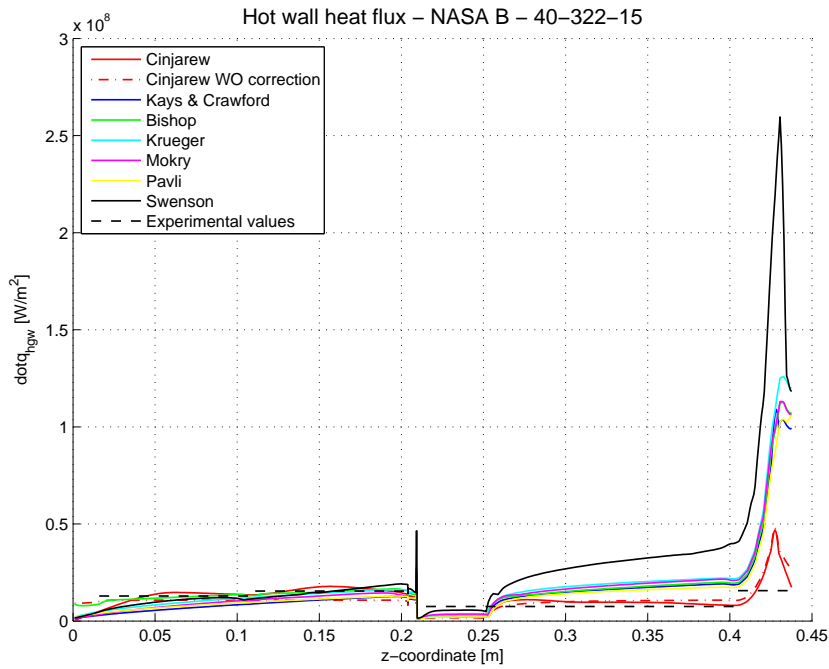
Figure 5.7: Punctual hot wall heat flux - 40-322-15
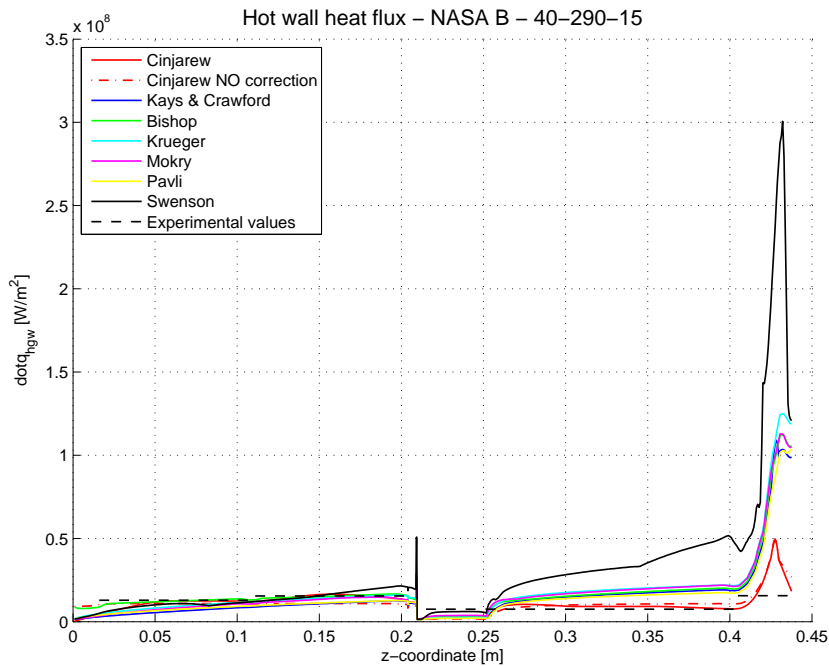
Figure 5.8: Punctual hot wall heat flux - 40-290-15

In these graphs it is possible to see a slight underprediction in the first two segments, the modelling issue with the corresponding heat flux peak in correspondence of the film applicator and an overprediction of all the models in the third and nozzle segments. The 10% reduction of the mixture ratio bring the simulated heat fluxes closer to the experimental values but, except from Cinjarew model, they are still overpredicting the heat fluxes. Also in this cases is possible to note the liquid film cooled length shown by the plateau after the film applicator.

60 bar

Figures 5.9, 5.10, 5.11 and 5.12 show the simulated hot wall heat fluxes for the load points presented in table 5.3.
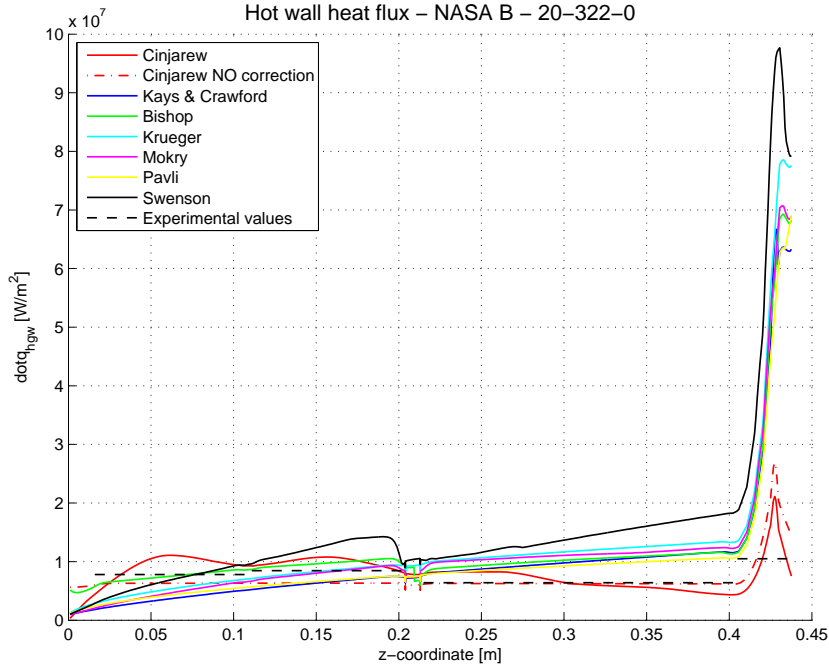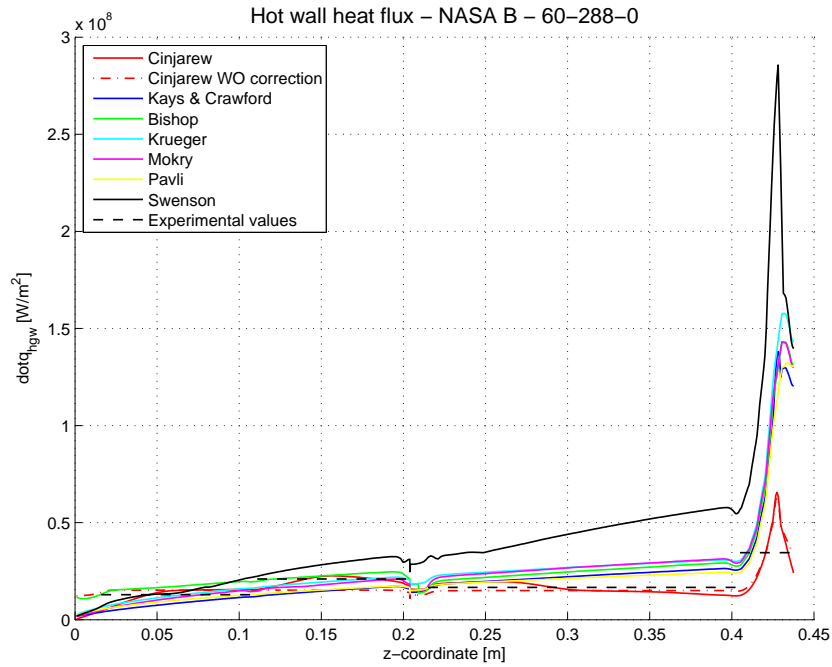

Figure 5.9: Punctual hot wall heat flux - 60-288-0
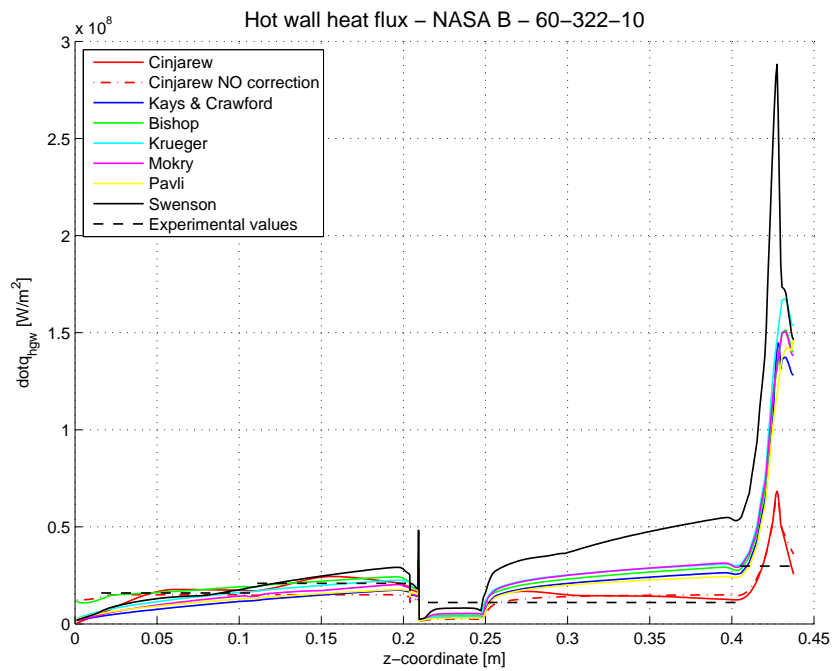
Figure 5.10: Punctual hot wall heat flux - 60-322-10
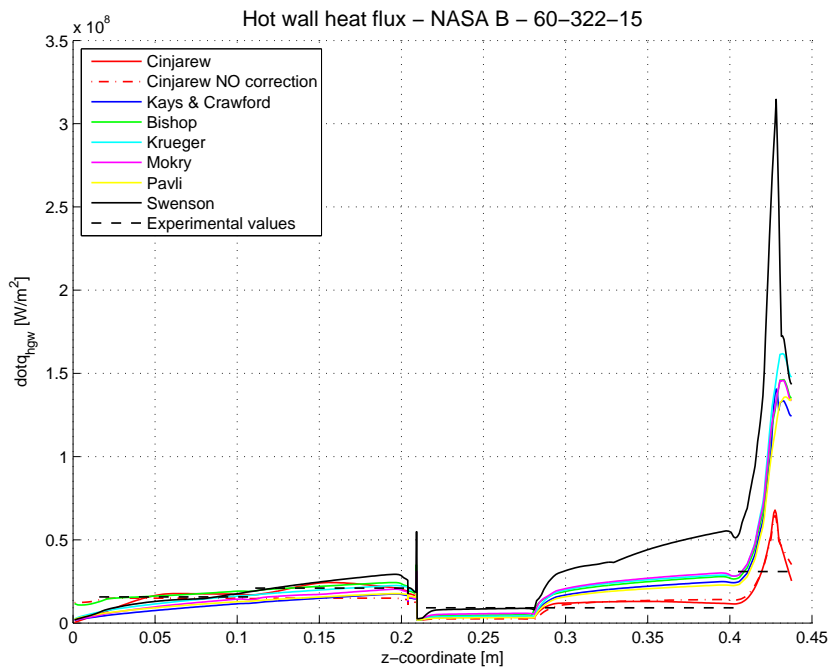
Figure 5.11: Punctual hot wall heat flux - 60-322-15
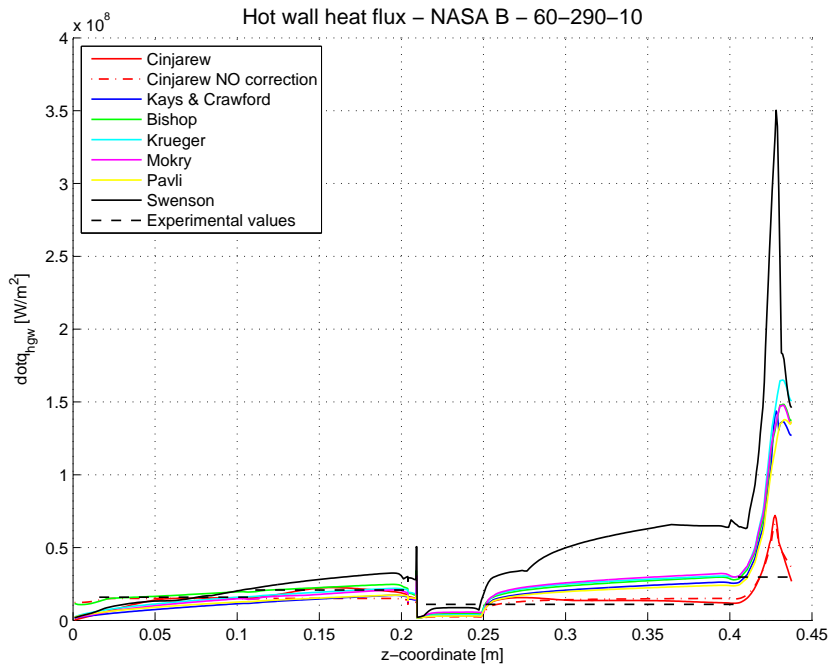
Figure 5.12: Punctual hot wall heat flux - 60-290-10

Even in these cases the prediction seems to be quite accurate in the first two segments before the film cooling application. After that it is possible to notice that Cinjarew model is quite accurate, the other models, except Swenson that badly overestimates the heat fluxes, slightly overpredict them. The mixture ratio reduction does not seem to improve the results.

80 bar

Figures 5.13, 5.14, 5.15 and 5.16 show the simulated hot wall heat fluxes for the load points presented in table 5.4.
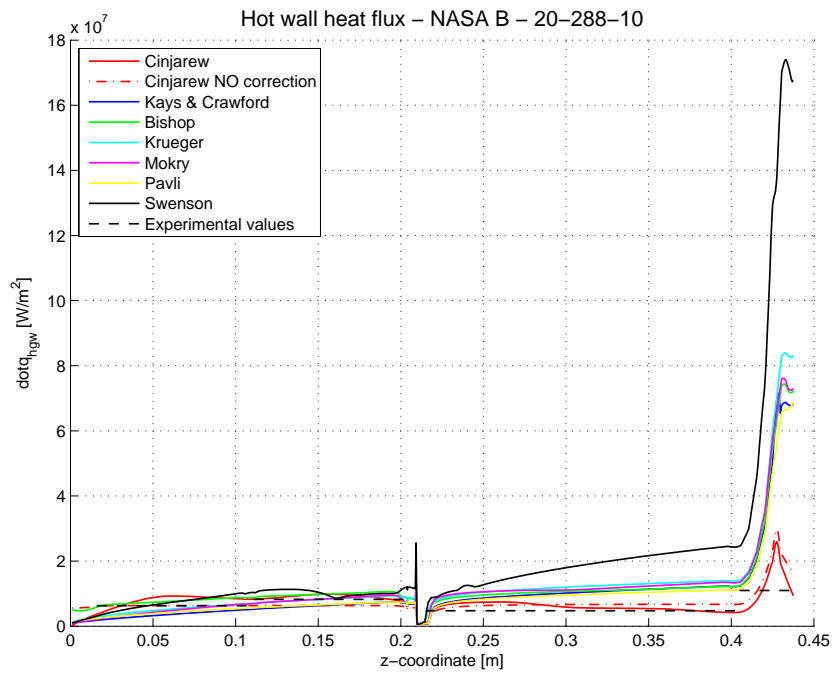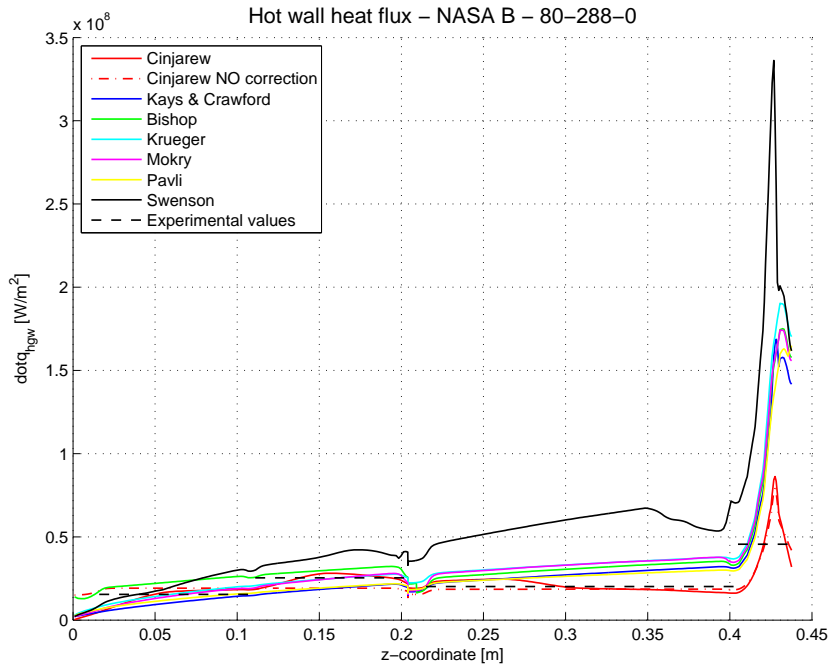

Figure 5.13: Punctual hot wall heat flux - 80-288-0
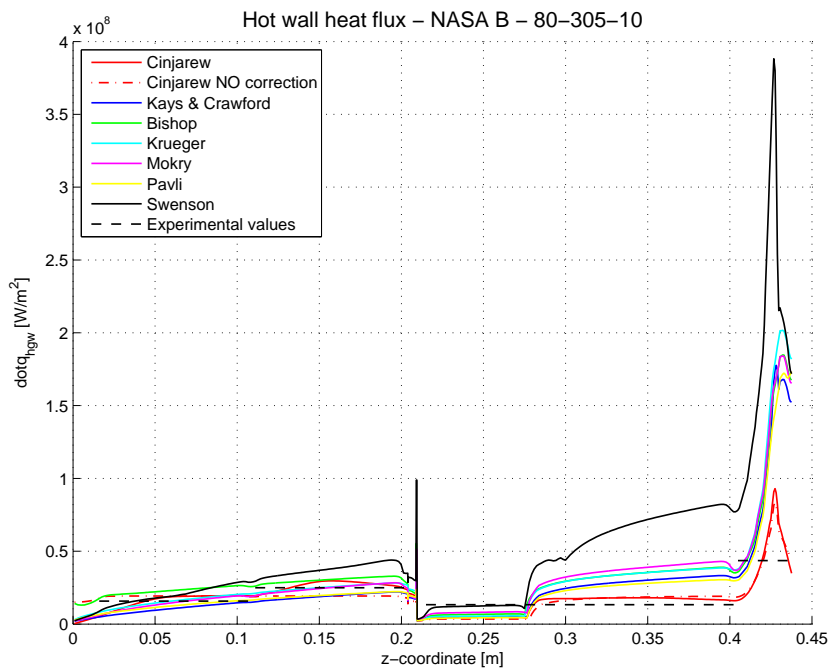
Figure 5.14: Punctual hot wall heat flux - 80-305-10
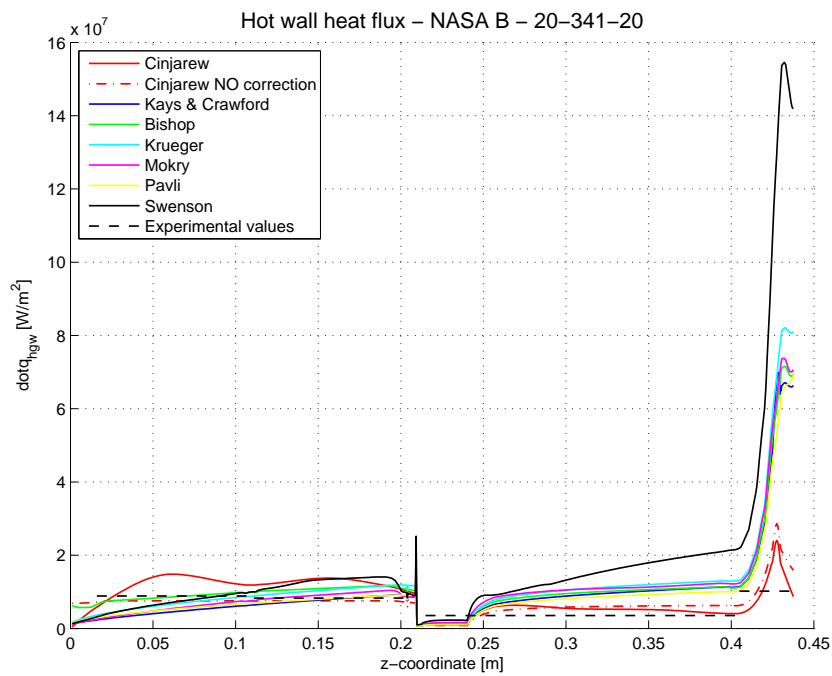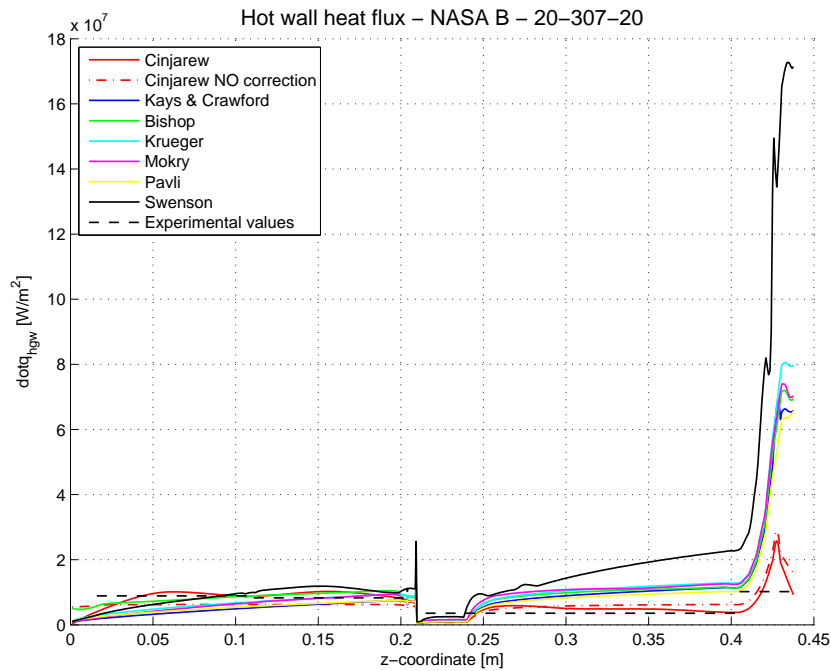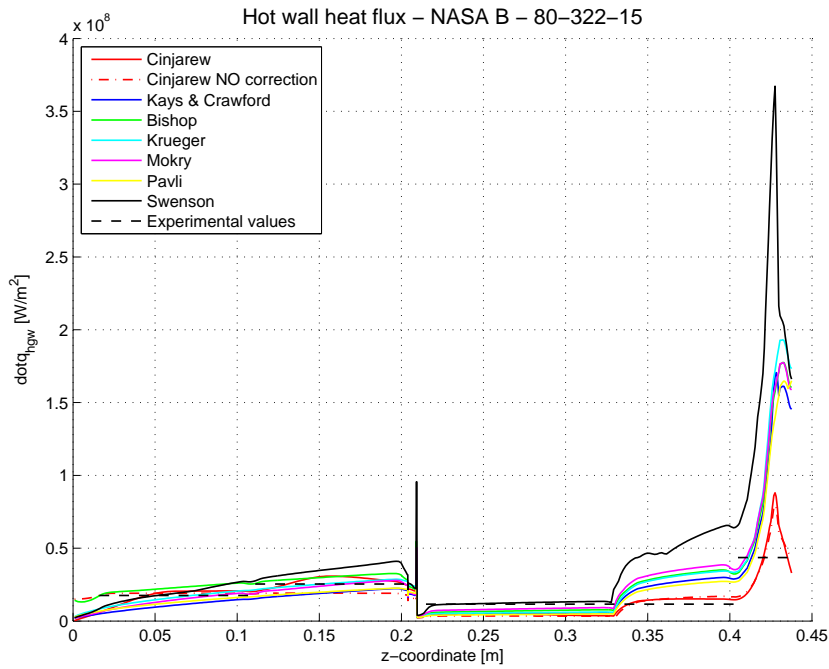
Figure 5.15: Punctual hot wall heat flux - 80-322-15
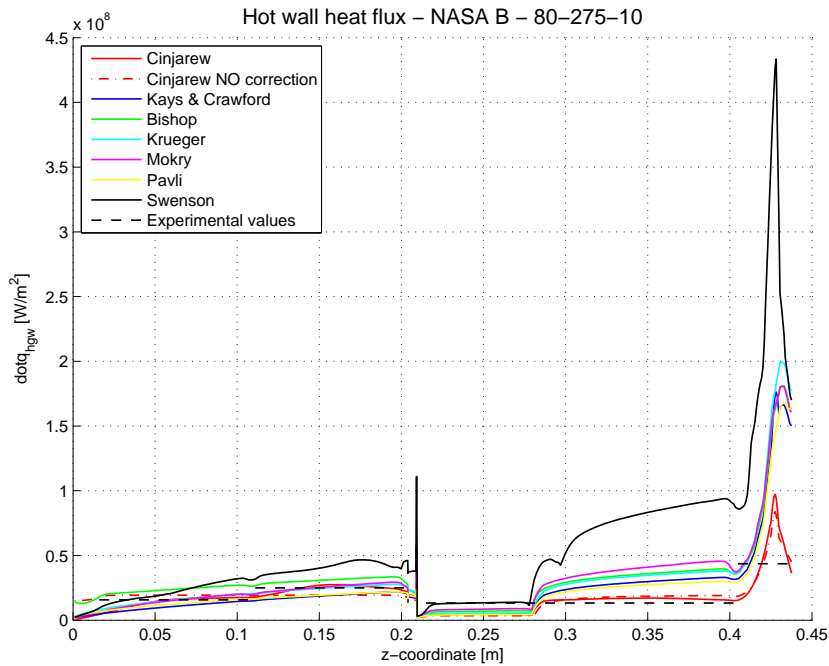
Figure 5.16: Punctual hot wall heat flux - 80-275-10

As we saw in the previous lower pressure load points simulation, the hot wall heat fluxes remain higher than the experimental values for all the new heat transfer coefficient correlation in the third and nozzle segment. In the first two segments, except for Swenson, the simulated values seem to be closer to the experimental values. The mixture ratio reduction does not result in a significant improvement of the accuracy of the solution.

5.2.1.2 Qualitative assessment of integral hot wall heat fluxes

To have a better understanding of the error between the experimental heat flux and the numerical one, heat flux integral values were calculated to show, segment wise, whether a model gives an over- or an underprediction.

Results are presented by pressure as in the previous section, each bar is one of the eight heat transfer models under investigation and, aside of each plot, there is a table showing the percentage error (calculated with equation 5.5); in these tables each row is one of the four segment and each column is one of the heat transfer model in this order: Cinjarew with TUM-LFA correction, Cinjarew without correction, Kays and Crawford, Bishop, Krueger, Mokry, Pavli and Swenson.

$$error = \frac{q_{calc} - q_{exp}}{q_{exp}} \cdot 100 \tag{5.5}$$

20 bar

Figures 5.17, 5.18, 5.19 and 5.20 show the integral hot wall heat fluxes for the load points of table 5.1.
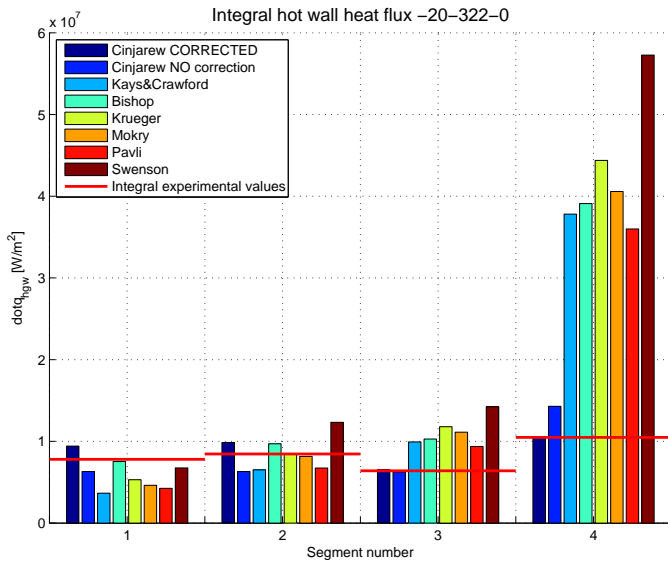
	Segment number			
	1	2	3	4
	20.74	16.56	1.82	-0.81
	-19.22	-25.39	-2.47	36.21
	-53.17	-23.00	55.26	260.5
	-3.56	14.74	60.80	272.9
	-32.14	-0.09	84.37	323.2
	-40.83	-3.52	73.93	286.9
	-45.49	-20.30	46.51	243.2
	-13.43	45.79	122.3	446.1

Table 5.6: Error 20-322-0

Figure 5.17: Integral hot wall heat flux - 20-322-0
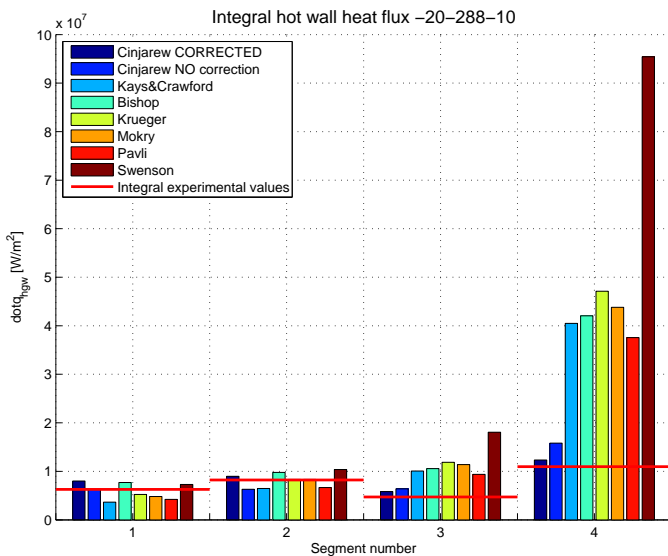
	Segment number			
	1	2	3	4
	27.72	9.29	23.20	12.52
	0.60	-23.29	35.53	44.33
	-41.69	-21.23	113.0	269.1
	22.79	19.11	123.5	283.4
	-16.65	1.38	150.9	329.5
	-23.13	1.52	140.7	299.4
	-32.68	-19.01	98.1	242.5
	16.29	26.15	281.9	770.0

Table 5.7: Error 20-288-10

Figure 5.18: Integral hot wall heat flux - 20-288-10

Figure 5.19: Integral hot wall heat flux - 20-341-20
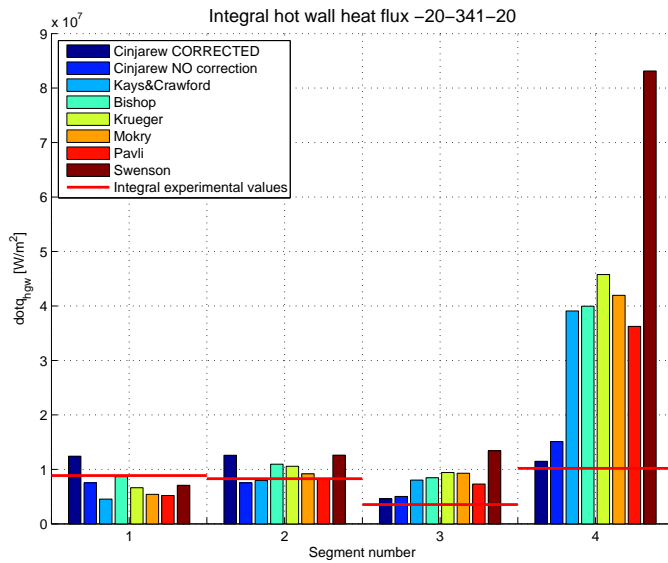
	Segment number			
	1	2	3	4
	40.14	51.71	29.81	12.66
	-15.03	-9.36	41.41	48.10
	-48.63	-4.13	126.3	283.4
Error [%]	-2.33	31.94	137.9	291.9
	-25.20	27.46	164.7	349.1
	-38.95	10.75	161.7	311.5
	-41.19	-1.62	105.5	255.6
	-20.07	52.07	277.4	715.5

Table 5.8: Error 20-341-20

Figure 5.20: Integral hot wall heat flux - 20-307-20
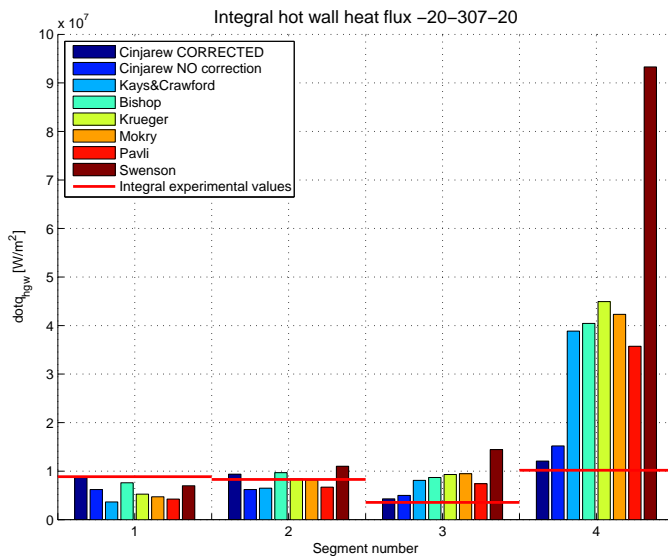
	Segment number			
	1	2	3	4
	-2.12	12.97	20.50	18.36
	-29.88	-25.18	40.40	49.00
	-58.65	-21.86	127.7	281.3
Error [%]	-14.29	16.78	144.4	296.6
	-40.59	1.13	161.9	340.9
	-46.84	-1.23	166.4	315.0
	-52.05	-19.30	108.4	250.5
	-21.09	32.78	306.4	815.2

Table 5.9: Error 20-307-20

It is possible to notice that, presenting the results in this way, it is easier to make a comparison between different models. For the 20 bar load points two clear trends are visible: in the first two segments the models underpredict the experimental values, while in the last two segments the new models give a great overprediction. In particular in the second segment is possible to note that Bishop, Krueger and Mokry are closer to the experimental results than all the other models. However in the third segment these three models have really high errors that can exceed 100%. Swenson model is the worst one, especially in the nozzle segment, having errors always above 120%.

40 bar

Figures 5.21, 5.22, 5.23 and 5.24 show the integral hot wall heat fluxes for the load points of table 5.2.
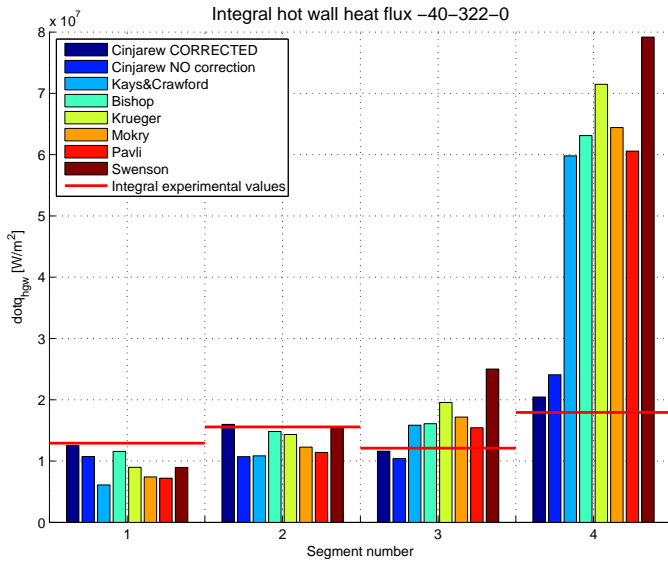
	Segment number			
	1	2	3	4
	-2.90	2.64	-4.16	14.07
	-16.91	-31.14	-14.00	34.38
	-52.79	-30.24	30.86	233.5
	-10.36	-4.77	32.90	252.0
Error [%]	-30.53	-7.93	61.48	298.7
	-42.62	-21.16	41.86	259.2
	-44.28	-26.70	27.53	237.9
	-30.70	-0.93	106.5	341.6

Table 5.10: Error 40-322-0

Figure 5.21: Integral hot wall heat flux - 40-322-0
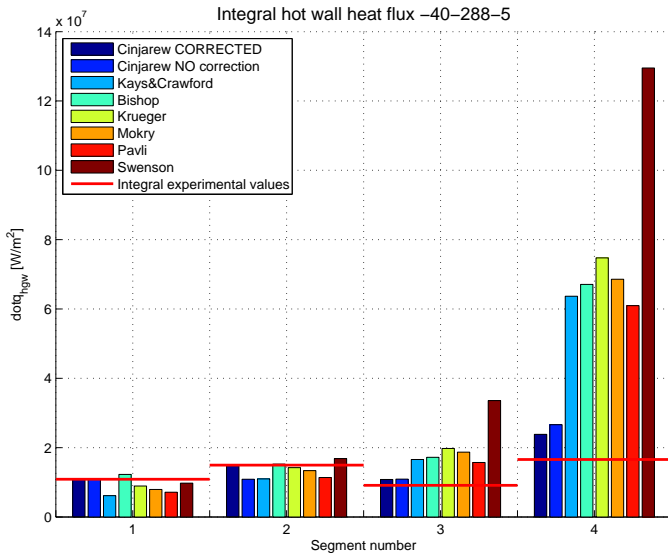
	Segment number			
	1	2	3	4
	-0.25	-1.10	18.31	43.65
	0.11	-27.15	19.24	60.31
	-43.62	-26.65	81.50	283.7
	12.56	1.92	88.31	304.3
Error [%]	-18.16	-4.76	116.3	350.5
	-27.26	-10.55	104.5	313.4
	-34.31	-24.00	71.86	267.4
	-10.58	12.66	267.3	680.7

Table 5.11: Error 40-288-5

Figure 5.22: Integral hot wall heat flux - 40-288-5
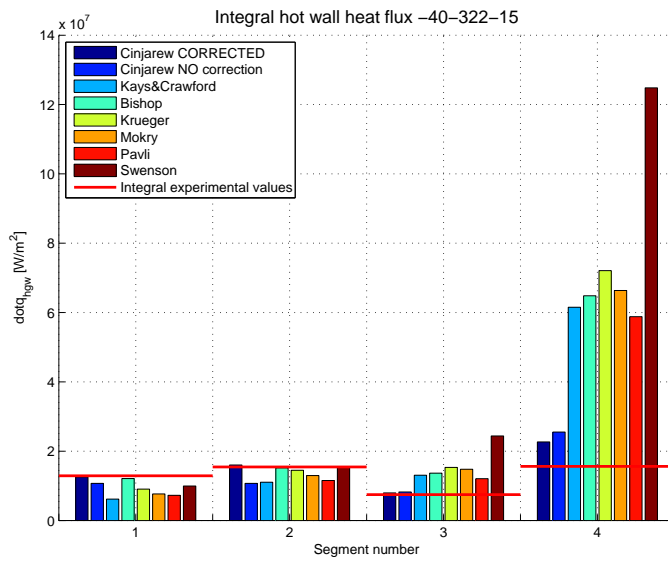
Figure 5.23: Integral hot wall heat flux - 40-322-15

Segment number			
1	2	3	4
-2.54	3.72	6.71	45.12
-16.77	-30.59	10.10	63.53
-52.04	-28.46	74.78	294.1
-6.00	-1.81	82.86	315.2
-29.70	-6.13	104.9	361.7
-40.48	-16.09	97.85	325.0
-43.71	25.33	61.68	276.6
-22.88	-0.05	226.8	699.3

Table 5.12: Error 40-322-15
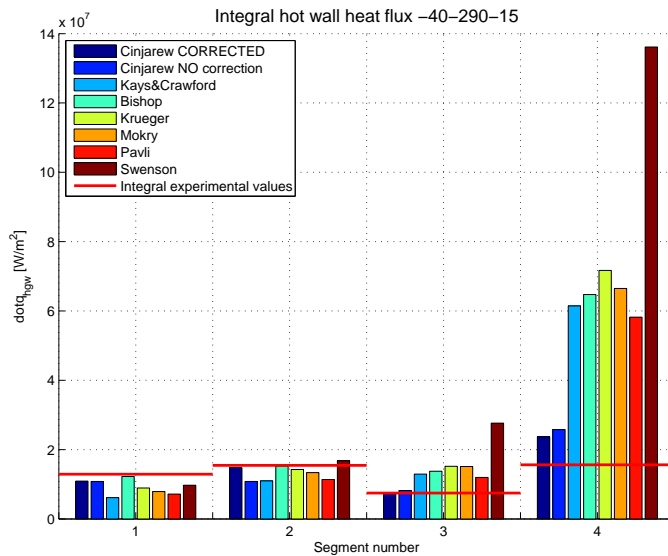
Figure 5.24: Integral hot wall heat flux - 40-290-15

Segment number			
1	2	3	4
-15.45	-4.28	1.91	51.68
-16.00	-29.95	9.92	65.19
-52.36	-28.97	73.14	293.7
-5.04	-1.38	84.35	314.6
-30.81	-7.73	103.4	359.0
-38.70	-13.60	102.3	325.8
-44.47	-26.40	60.41	272.7
-24.50	8.51	269.9	772.0

Table 5.13: Error 40-290-15

As we can see from the figures, increasing the combustion chamber pressure does not imply a change in the models behavior: in the first two segments they underpredict the experimental heat fluxes and in the other two there is a general overprediction. It can be pointed out that, especially in the second segment, when the influence of the injector and of the chemical reaction is not so dominant anymore, Bishop, Krueger and Mokry models provide quite good agreement with experimental results even if in the film cooled segment the overestimation is really high. Even with 40 bar load points Swenson model turns out to give the worst prediction with errors exceeding 200% in the last two segments.

60 bar

Figures 5.25, 5.26, 5.27 and 5.28 show the integral hot wall heat fluxes for the load points of table 5.3.

Figure 5.25: Integral hot wall heat flux - 60-288-0
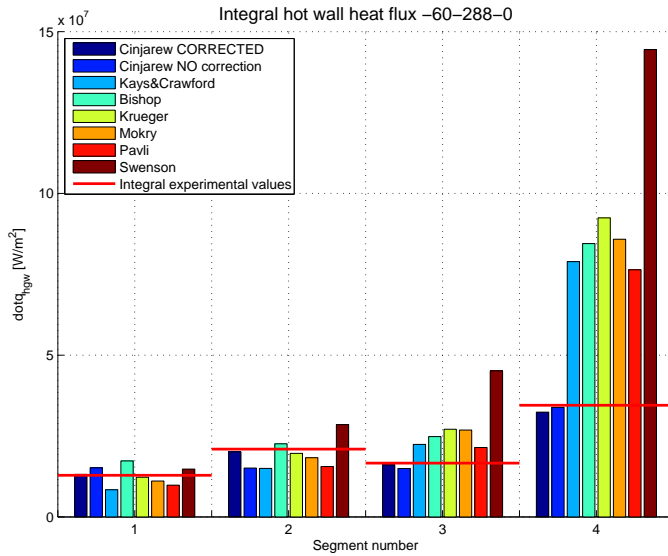
	Segment number			
	1	2	3	4
	2.29	-4.06	-3.43	-6.25
	17.87	-27.88	-10.08	-1.88
	-34.75	-28.52	34.86	128.5
Error [%]	34.45	7.81	49.39	144.7
	-4.63	-6.30	63.01	167.7
	-13.93	-12.62	61.52	148.6
	-23.89	-25.76	29.04	121.3
	14.90	36.10	171.5	318.4

Table 5.14: Error 60-288-0

Figure 5.26: Integral hot wall heat flux - 60-322-10
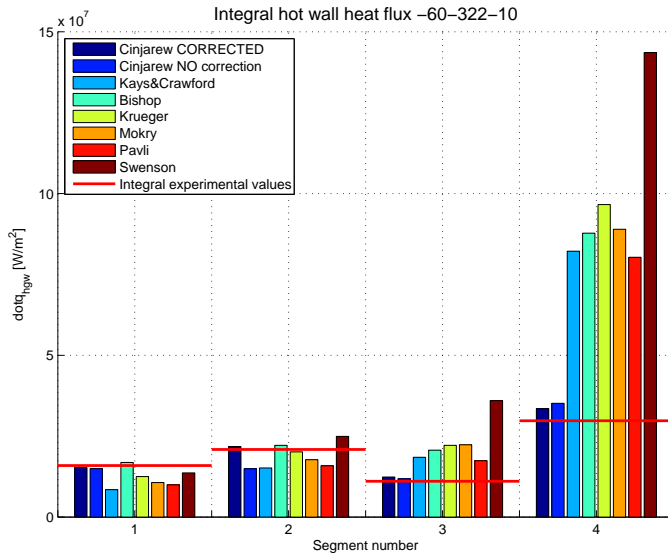
	Segment number			
	1	2	3	4
	-4.09	4.21	11.90	12.55
	-6.10	-28.56	6.84	18.12
	-46.72	-27.32	67.29	176.3
Error [%]	5.99	6.12	87.41	195.0
	-21.32	-3.60	100.6	224.7
	-32.92	-15.05	102.3	199.0
	-37.42	-24.05	57.65	170.0
	-14.32	19.42	226.0	382.6

Table 5.15: Error 60-322-10

Figure 5.27: Integral hot wall heat flux - 60-322-15
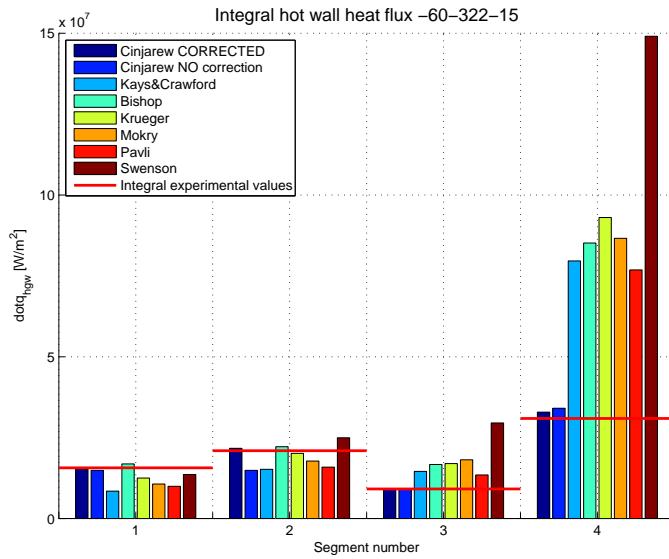
	Segment number			
	1	2	3	4
	-2.89	3.55	-0.91	6.38
	-4.93	-29.01	-1.94	10.24
	-45.90	-27.50	59.23	157.6
	7.63	5.93	82.52	175.5
Error [%]	-20.07	-3.86	85.98	200.8
	-31.93	-15.24	98.76	180.2
	-36.45	-24.26	47.55	148.5
	-13.06	19.23	223.1	382.1

Table 5.16: Error 60-322-15

Figure 5.28: Integral hot wall heat flux - 60-290-10
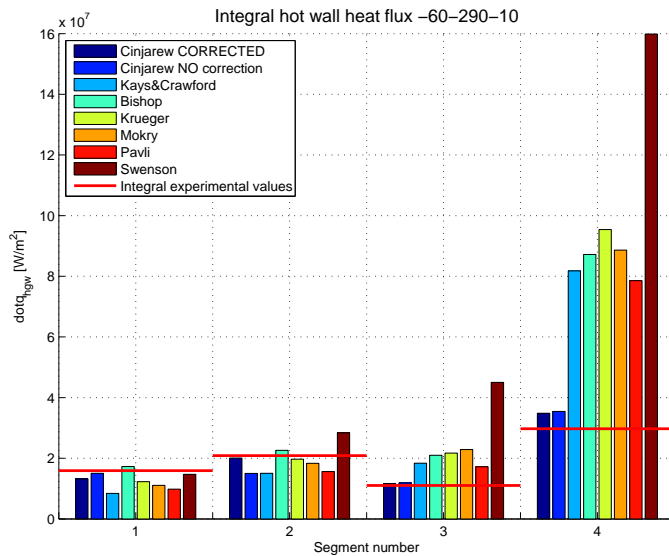
	Segment number			
	1	2	3	4
	-17.13	-3.77	5.50	17.11
	-5.46	-28.08	7.62	19.20
	-47.19	-28.01	66.57	174.9
	8.65	8.40	90.24	193.2
Error [%]	-22.78	-5.64	96.65	220.8
	-30.46	-12.09	107.2	197.9
	-38.38	-25.27	55.85	164.2
	-7.53	35.99	308.0	437.5

Table 5.17: Error 60-290-10

The 60 bar load points show a similar behavior to the lower pressure load points. In the first two segments the models underestimates the experimental heat fluxes except for Bishop that exhibit a good agreement with the reference heat fluxes. It can be stated also that in these segments also Krueger and Mokry give acceptable prediction. In the third and fourth segment a generally high overprediction is visible and the worst model is, as in the previous case, Swenson that has an error of more then 200%.

80 bar

Figures 5.29, 5.30, 5.31 and 5.32 show the integral hot wall heat fluxes for the load points of table 5.4.

Figure 5.29: Integral hot wall heat flux - 80-288-0
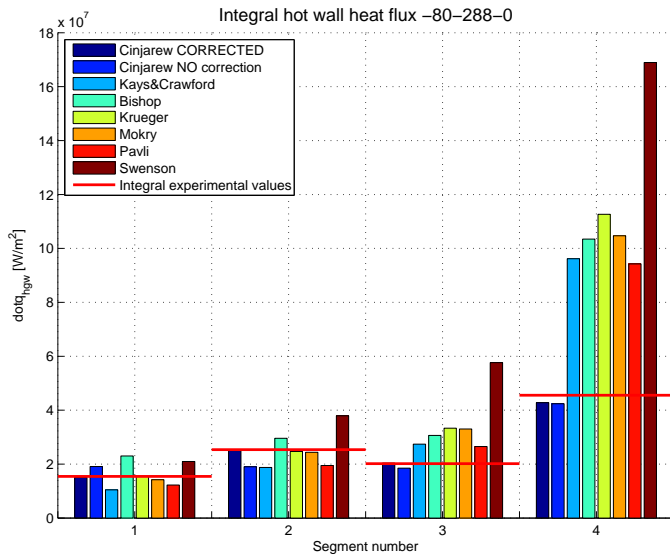
	Segment number			
	1	2	3	4
	-2.56	-1.45	1.02	-6.05
	23.71	-24.97	-8.26	-6.95
	-32.22	-26.10	35.91	111.2
	48.83	16.52	51.93	127.1
Error [%]	-0.04	-2.72	65.14	147.3
	-7.99	-3.97	63.63	129.9
	-20.82	-23.15	31.34	107.0
	35.66	49.57	185.7	270.9

Table 5.18: Error 80-288-0

Figure 5.30: Integral hot wall heat flux - 80-305-10
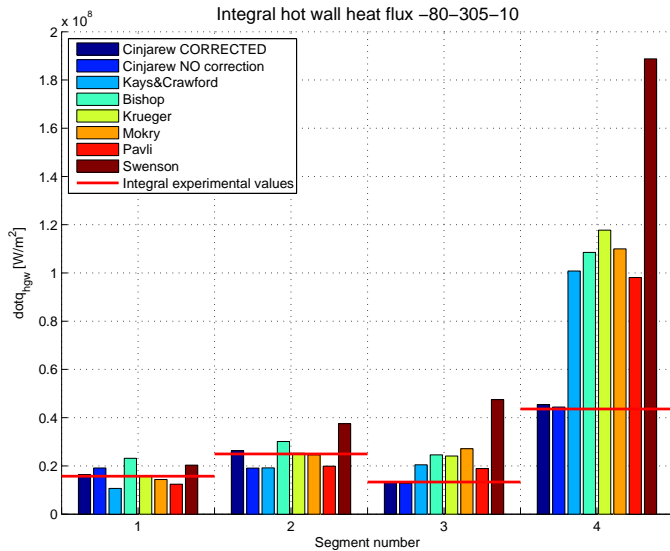
	Segment number			
	1	2	3	4
	4.17	5.51	-1.51	4.29
	21.66	-23.42	-3.93	1.88
	-32.24	-23.08	53.88	131.3
	47.06	20.72	84.80	149.0
Error [%]	-0.12	1.25	81.19	170.2
	-8.67	-1.46	103.9	152.4
	-20.99	-20.24	42.17	125.1
	29.18	50.21	257.0	333.1

Table 5.19: Error 80-305-10

Figure 5.31: Integral hot wall heat flux - 80-322-15
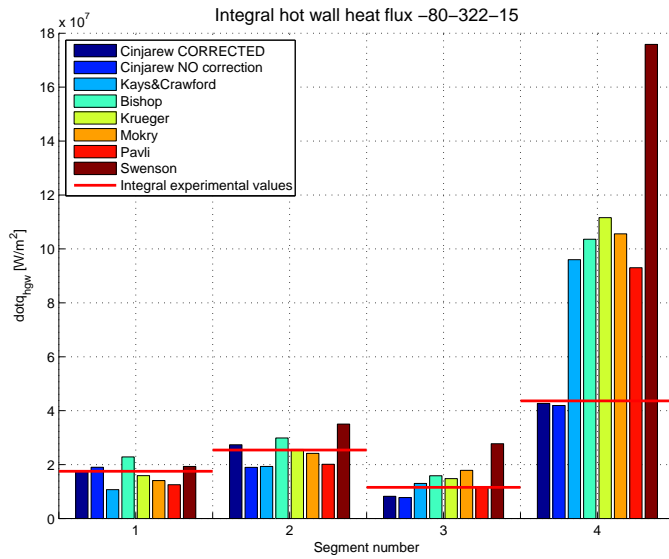
Segment number			
1	2	3	4
0.64	7.76	-28.81	-2.07
8.50	-25.20	-32.77	-3.91
-38.89	-23.88	12.63	120.1
30.29	17.67	37.30	137.5
-9.31	0.88	27.96	155.8
-19.67	-4.84	54.70	142.1
-28.46	-20.80	1.49	113.3
10.14	38.00	140.1	303.2

Table 5.20: Error 80-322-15

Figure 5.32: Integral hot wall heat flux - 80-275-10
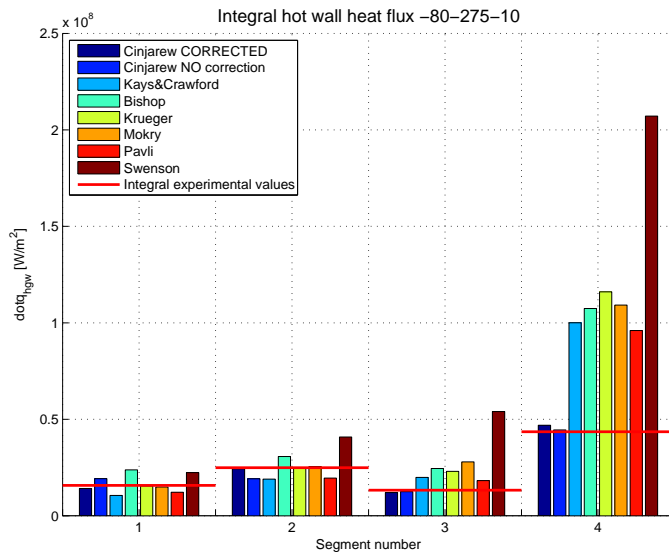
Segment number			
1	2	3	4
-10.09	-2.48	-9.58	7.66
22.19	-23.09	-5.85	2.16
-32.88	-23.84	49.79	129.5
51.14	23.25	84.23	146.5
-1.91	-0.58	73.34	166.2
-5.12	2.35	110.1	150.5
-22.25	-21.60	37.15	120.3
42.25	63.58	306.0	375.3

Table 5.21: Error 80-275-10

As we can see, even at the highest pressure, the behavior of the heat transfer coefficient models do not change. In the first two segments, on one hand, the models by Bishop, Krueger and Mokry show a quite good agreement with heat flux experimental values, but on the other hand Kays and Crawford and Pavli underestimate the experimental values and Swenson overpredicts them. In the third and nozzle segment, instead, all the analyzed models give a bad overprediction, especially in the nozzle segment.

5.2.1.3 Conclusions

The results from the implementation of the new hot wall heat transfer coefficient model together with NASA B film cooling model, give some interesting indications.

First of all it is possible to see a common behavior: the new models constantly overestimate the experimental heat fluxes in the third and nozzle segment for all the load points considered. In particular Swenson model gives the worst results with error peak of more than 700%.

In the first two segment, with the exception of Bishop and Swenson models, there is a constant underprediction of the heat fluxes. In the first two segments, however, three models predict the heat fluxes very close to the target, they are Bishop, Krueger and Mokry.

Another remark is that mixture ratio reduction does not give significant improvements in lowering the error between experimental and numerical results. In that load points numerical heat fluxes are closer to the experimental heat fluxes than other load points, but not in a so significant way as expected.

5.2.2 Stechman liquid film cooling model

In this section the film cooling model will be changed from NASA B to Stechman liquid film cooling model, which is described in 2.4.1. The hot wall heat transfer models will be the same investigated with NASA B and at the end of this section a comparison between NASA B and Stechman results will be presented.

As for NASA B model results are presented, in an histogram, in integral form; each bar is one of the eight heat transfer model under investigation and aside of each plot there is a table showing the percentage error (calculated, as in the previous case, with equation 5.5); in these tables each row is one of the four segment and each column is one of the heat transfer model in this order: Cinjarew with TUM-LFA correction, Cinjarew without correction, Kays and Crawford, Bishop, Krueger, Mokry, Pavli and Swenson.

For Stechman model only four out of sixteen load points are presented, one for each pressure, in order to not burden the discussion. These load points are, in fact, enough to have a feeling of the behavior of the model.

Figures 5.33, 5.34, 5.35 and 5.36 show the integral hot wall heat fluxes for the following load points: 20-288-10, 40-288-5, 60-322-10 and 80-322-15.
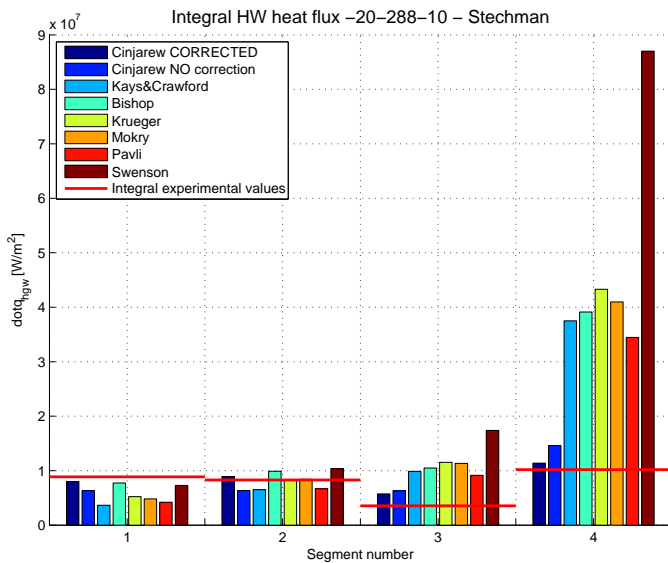
	Segment number			
	1	2	3	4
	-9.60	7.63	61.48	11.70
	-28.64	-23.82	77.37	43.30
	-58.85	-21.77	177.5	268.0
	-12.67	19.26	194.7	283.9
Error [%]	-40.99	0.37	224.0	324.7
	-45.62	1.55	218.8	302.0
	-52.48	-19.69	157.3	238.1
	-17.66	24.92	388.8	753.6

Table 5.22: Error 20-288-10 - Stechman

Figure 5.33: Integral HW heat flux - 20-288-10 - Stechman

Figure 5.34: Integral HW heat flux - 40-288-5 - Stechman
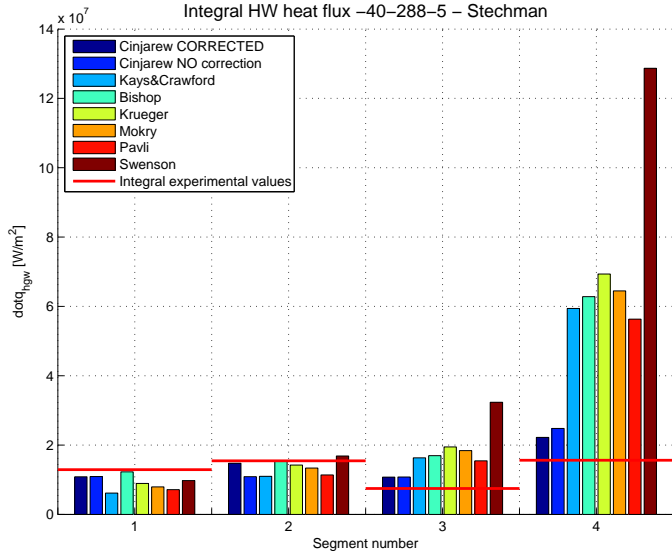
	Segment number			
	1	2	3	4
Error [%]	-15.75	-4.47	43.81	42.31
	-15.45	-29.53	44.26	58.76
	-52.38	-29.03	118.6	280.5
	-4.92	-1.40	126.7	302.2
	-30.87	-7.85	160.6	344.1
	-38.56	-13.45	146.4	313.0
	-44.51	-26.47	106.7	260.8
	-24.46	8.99	333.1	724.2

Table 5.23: Error 40-288-5 - Stechman

Figure 5.35: Integral HW heat flux - 60-322-10 - Stechman
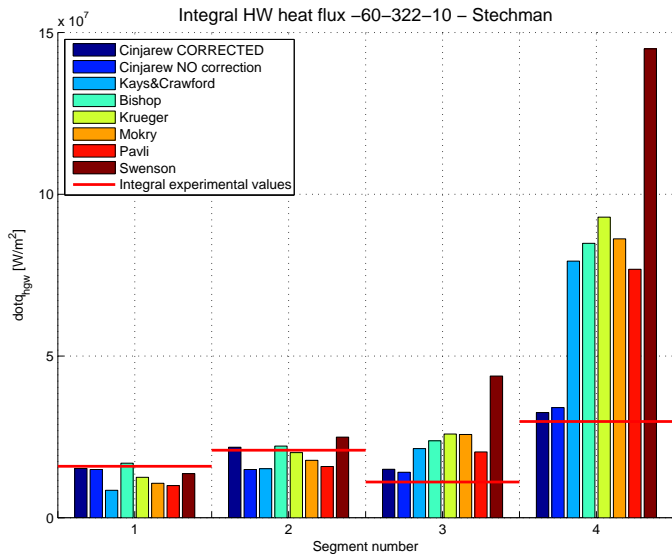
	Segment number			
	1	2	3	4
Error [%]	-4.15	4.48	35.97	9.31
	-6.16	-28.60	27.47	14.47
	-46.7	-27.29	93.82	166.7
	6.00	6.15	115.5	185.2
	-21.3	-3.57	134.6	212.5
	-32.92	-15.01	133.3	189.8
	-37.42	-24.03	84.3	158.2
	-14.31	19.48	296.9	387.3

Table 5.24: Error 60-322-10 - Stechman
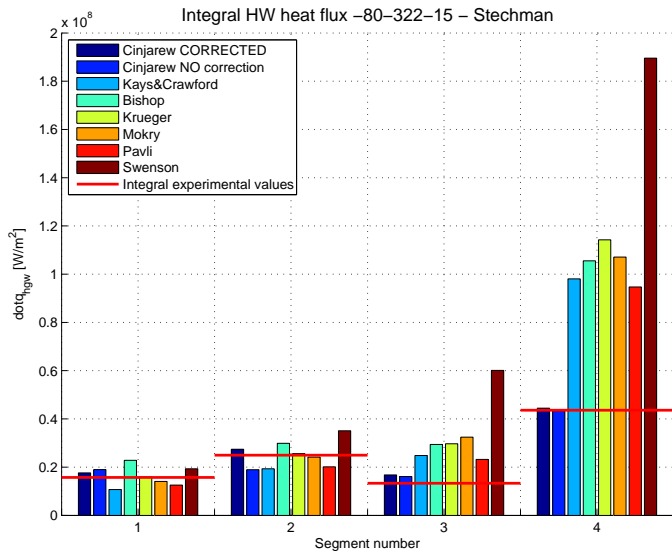
	Segment number			
	1	2	3	4
	11.89	9.91	25.98	1.98
	20.64	-24.00	20.93	-0.53
	-31.90	-22.50	86.63	125.0
Error [%]	45.15	19.80	120.9	142.1
	1.04	2.69	123.2	162.2
	-10.52	-3.11	143.9	145.7
	-20.31	-19.37	74.5	117.3
	22.71	40.56	351.7	335.0

Table 5.25: Error 80-322-15 - Stechman

Figure 5.36: Integral HW heat flux - 80-322-15 - Stechman

It is possible to see that the difference between the two models are, obviously, in the third and fourth segment. Here a general overestimation of the experimental heat fluxes for all the heat transfer coefficient model, as for NASA B, is visible. In the next section a comparison between NASA B and Stechman is carried out.

5.2.2.1   NASA B vs Stechman Model

In this section, NASA B and Stechman predictions are compared in order to establish which of the two is closer to the experimental heat fluxes. Each figure is one of the heat transfer coefficient model under investigation and for each load point the first bar is related to NASA B model, the second one to Stechman; magenta lines indicates the integral experimental value for that load point.
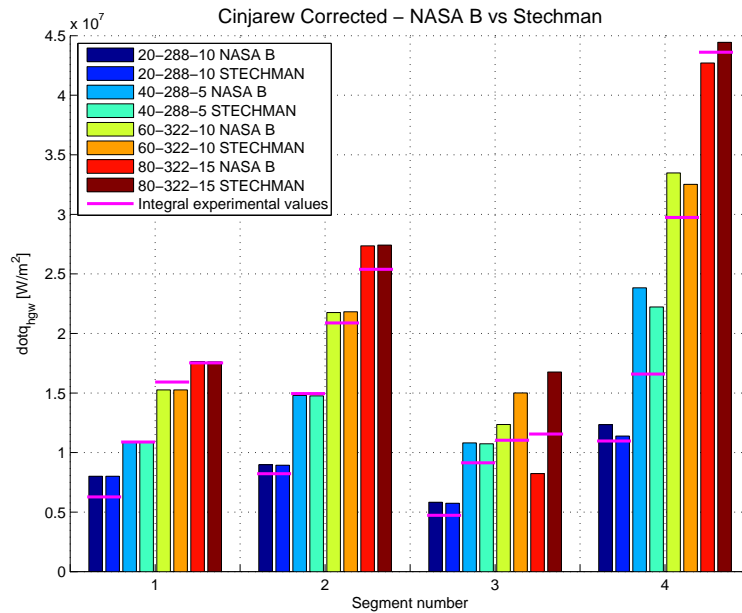
Figure 5.37: NASA B vs Stechman - Cinjarew Corrected
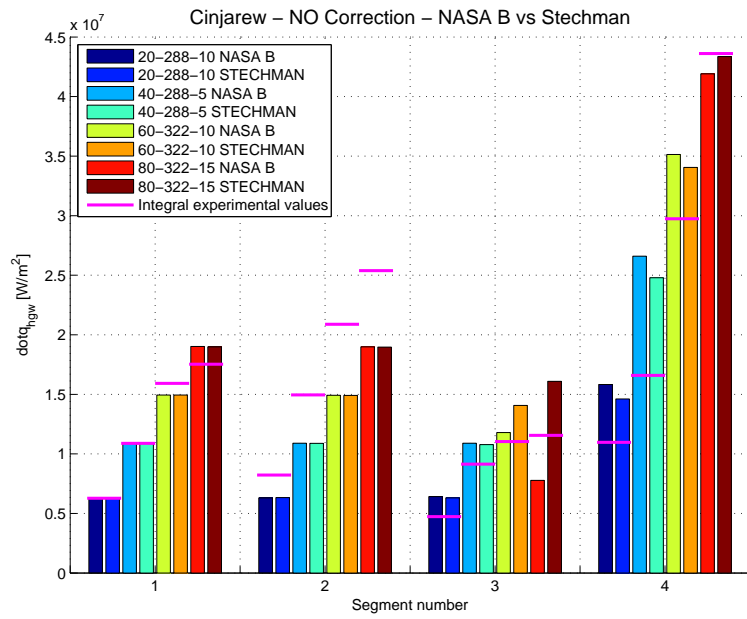
Figure 5.38: NASA B vs Stechman - Cinjarew without correction
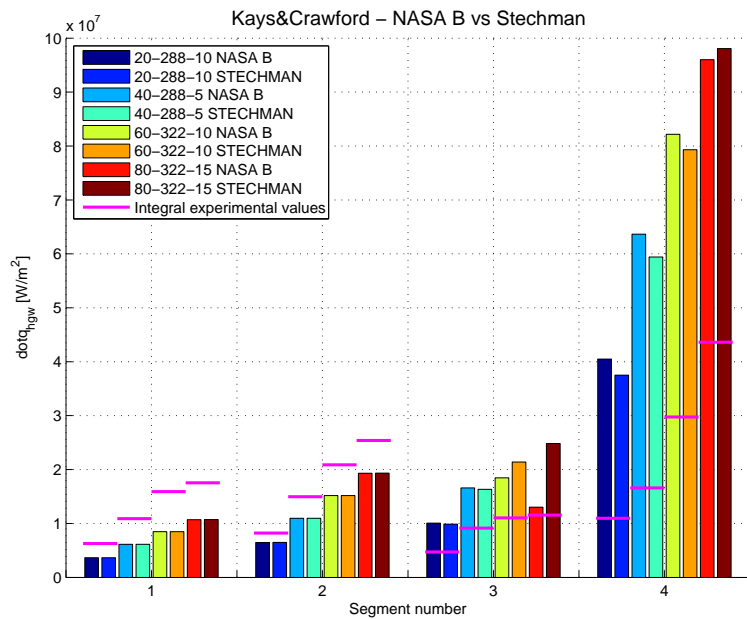
Figure 5.39: NASA B vs Stechman - Kays and Crawford
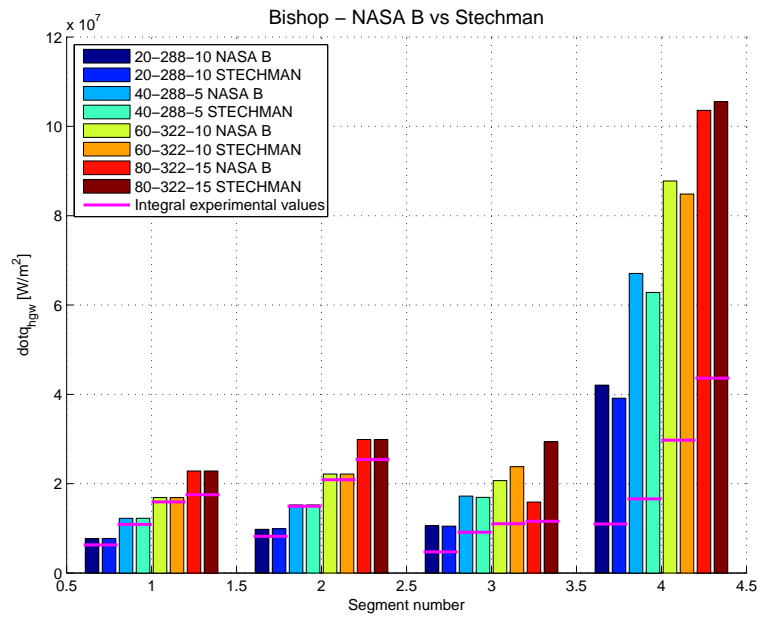
Figure 5.40: NASA B vs Stechman - Bishop
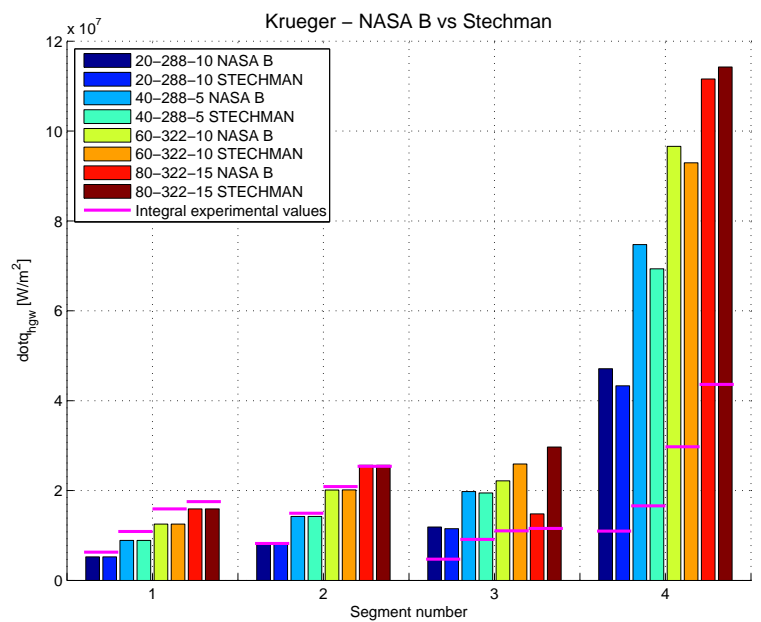
Figure 5.41: NASA B vs Stechman - Krueger
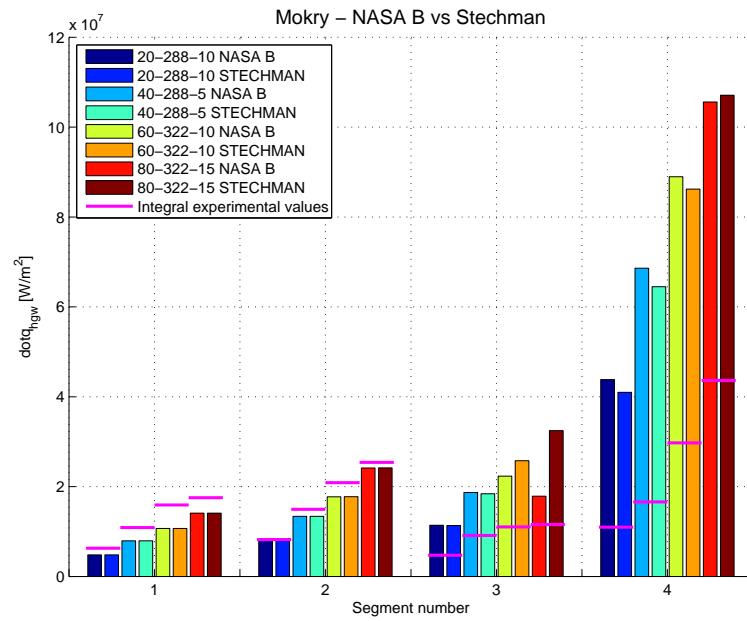
Figure 5.42: NASA B vs Stechman - Mokry
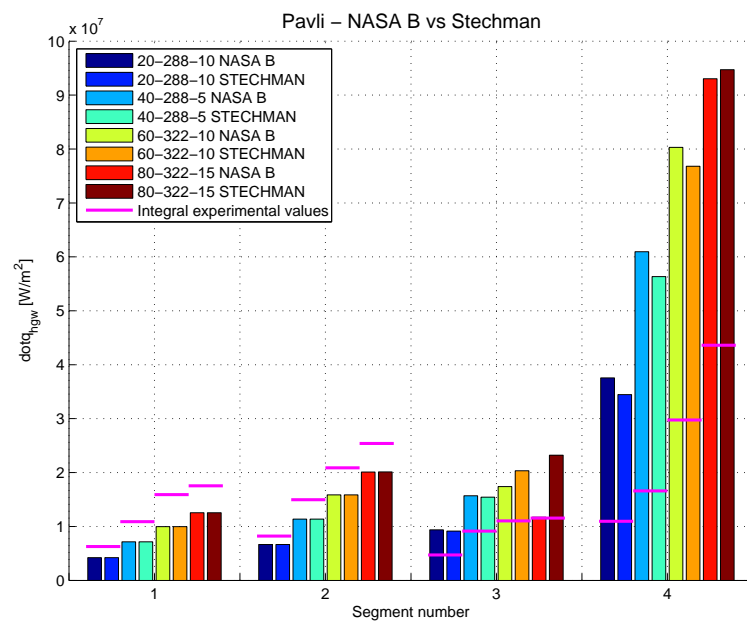
Figure 5.43: NASA B vs Stechman - Pavli
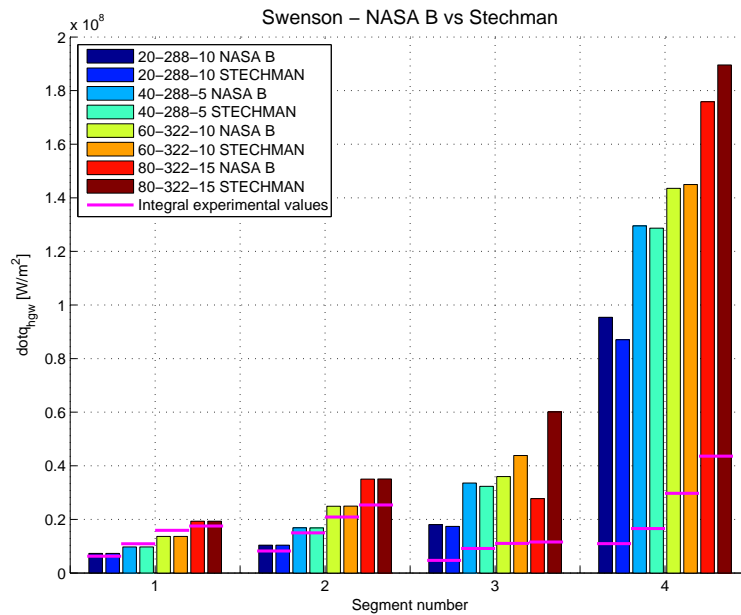
Figure 5.44: NASA B vs Stechman - Swenson

In these figures it is possible to note that, obviously, the influence of the film cooling model manifests itself only on the last two segments and therefore predicted hot wall heat fluxes in the first two segments are the same of the simulation carried out with NASA B model. Differences can be found in the last two segment where a general overprediction can be seen. In particular, for all the heat transfer coefficient model analyzed, Stechman model gives a lower prediction, with respect to NASA B model, at low pressure (20 and 40 bar) and a higher estimation at high pressure (60 and 80 bar).

5.2.3 Conclusions

After simulating the hot wall heat fluxes for different pressures and with different film cooling and heat transfer coefficient models it is possible to draw some conclusions. With NASA B all the new heat transfer coefficient models give general overprediction in the third and second segment. In particular Kays and Crawford, Pavli and Swenson give the worst predictions, with really high errors, even in the first two segments and for this reasons they will not be investigated further. The other three remaining, Bishop, Krueger and Mokry, display high errors in the third and fourth segment, too. These, however, are less high than the previous models and their predictions in the first two segments are characterized by good agreement with experimental results. Therefore only these last three models will be optimized for the TUM-LFA combustion chamber in the next chapter.

Regarding Stechman film cooling model is possible to notice that it gives generally not better results than NASA B model. Error reduction at low pressure, in fact, is not so significant and, in the meantime, at high pressure the difference between numerical and experimental has increased. This is because this film cooling model was developed for rockets characterized by low combustion chamber pressure and for this reason is not fully applicable to TUM-LFA combustion chamber that operates as well at high pressure. For this reasons Stechman model will not be investigated further and NASA B will be the film cooling model for the optimization of the next chapter.

Chapter 6

Optimization

In this chapter the description of the optimization of the three heat transfer model chosen in chapter 5 will be carried out. After that each correction will be applied to the analyzed load points to check its behavior and finally find out which corrected heat transfer model will be the designated one to predict the heat fluxes in Thermtest.

6.1 Heat flux against mixture ratio

Once chosen the three heat transfer coefficient models to optimize, Bishop, Krueger and Mokry, the first thing to understand is if a correlation subsist between the experimental and the calculated heat fluxes. In this section experimental and numerical heat fluxes will be plotted against mixture ratio, with and without film and for each segment and heat transfer coefficient model, in order to find that correlation on which we will operate to improve the numerical prediction of the experimental heat fluxes.

In all the graphs numerical simulation are identified by markers: red circles for 20 bar, blue diamonds for 40 bar, magenta squares for 60 bar and black triangle for 80 bar; dashed lines characterized, instead, the experimental results and a marker is provided for each of the load points investigated.

6.1.1 Bishop
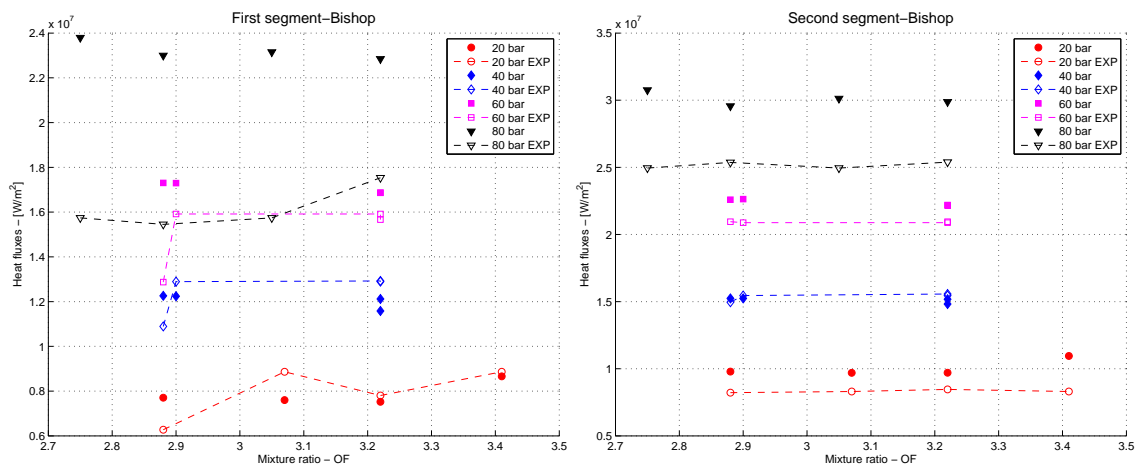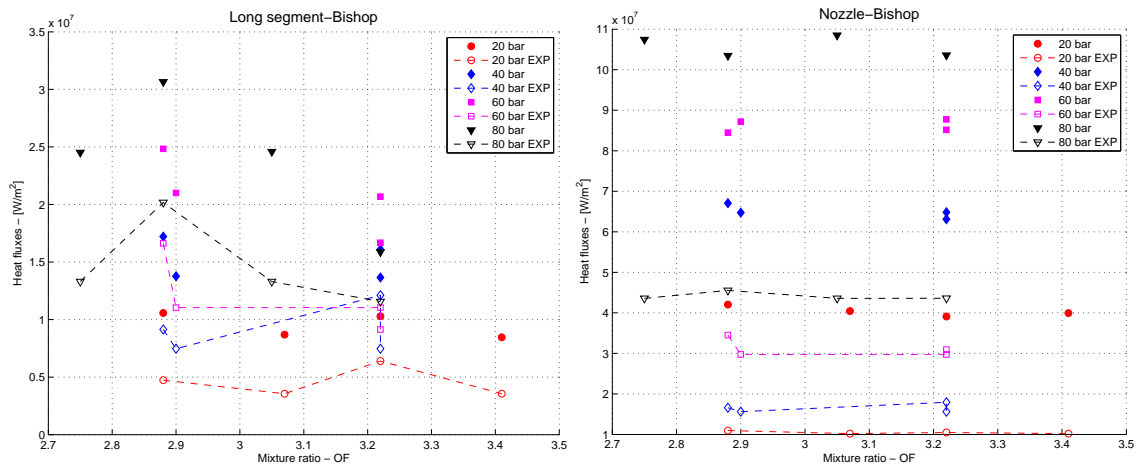
Figure 6.1: Heat fluxes vs mixture ratio - Bishop

From figure 6.1 it is possible to note, especially for the second and the third/long segment, that a constant shift between experimental and numerical results exists. This shift is more visible in the third segment where numerical results are almost constantly higher then the correspondent experimental value by $1 \cdot 10^7$ W/m^2. In the first two segments, instead, the constant shift is more visible at high pressure than at low pressure. The results of the first segments must be considered with caution because combustion, chemical reaction and turbulent mixing are predominant and are not taken into account in any of the models investigated. Also nozzle segment results must be handled with care; in fact the models do not implement tools that contemplate accelerations and overspeeds of the combustion gases caused, inter alia, by the curvature of the throat.

6.1.2   Krueger

In figure 6.2 Krueger heat fluxes against mixture ratio are presented. Same remarks made for the first and nozzle segment for Bishop can be carried out also here. Furthermore the second segment is quite peculiar because simulations are really close to the experimental results. Focusing on the third segment, a constant shift of about $1 \cdot 10^7$ W/m^2 is visible, especially for high pressures.
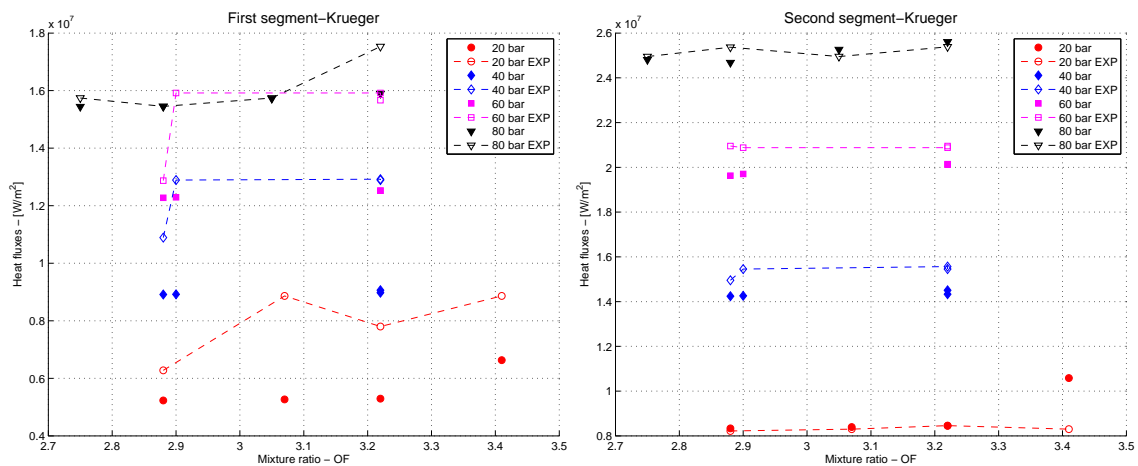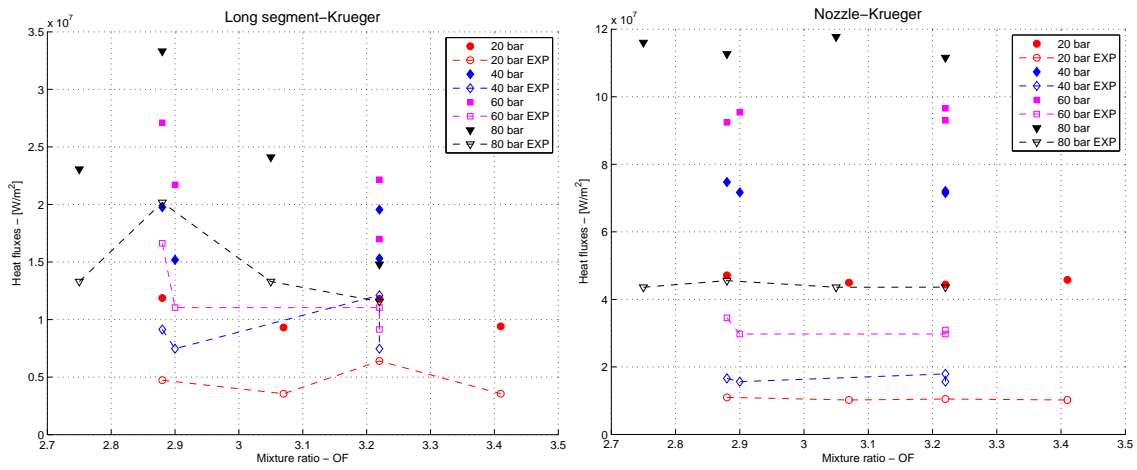
Figure 6.2: Heat fluxes vs mixture ratio - Krueger

6.1.3 Mokry
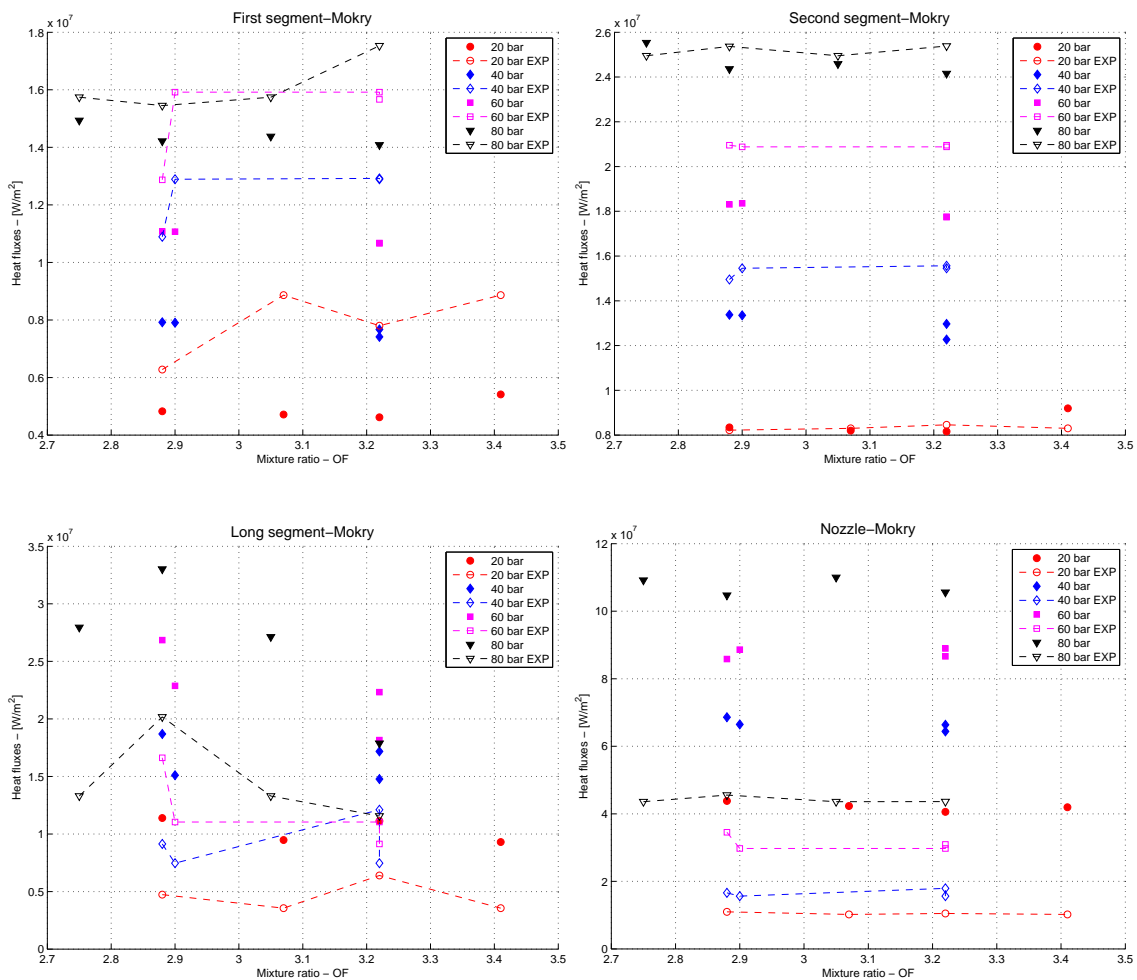
Figure 6.3: Heat fluxes vs mixture ratio - Mokry

Regarding Mokry model, presented in figure 6.3, the same remarks of the previous model, for the first and the nozzle segments, can be done. Second segment is characterized by a constant

shift for 40 and 60 bar, meanwhile for 20 and 80 bar simulated and experimental heat fluxes are quite close to each other. Even for Mokry heat transfer coefficient model there is a shift of about $1 \cdot 10^7$ W/m^2 between experimental and numerical results. This shift is a little bit higher for 80 bar load points.

6.2   Correlation

After noticing, at least in the third segment, a constant shift in the heat fluxes, it is possible to work on that to correct the numerical results. The aim of the optimization is to describe test data by an easy-to-handle correlation in order to obtain, in the end, a correction factor that will be applied in Thermtest.

First of all every experimental load point without film cooling available at TUM-LFA has been correlated by equation 6.1.

$$q_{correlation} = a \cdot OF^b \cdot PCC^c \tag{6.1}$$

Equation 6.1 uses three parameters to describe the heat flux as function of only mixture ratio and combustion chamber pressure. The three constants a, b and c were found minimizing the error between the experimental and the correlated heat fluxes (calculated with equation 6.1). In particular a is a multiplier, b describes the influence of mixture ratio and c the influence of combustion chamber pressure. The values of these constants are presented in table 6.1.

	Segment 1	Segment 2	Segment 3	Nozzle
a	128469.5	332159.9	315499.2	413545.7
b	2.127	0.892	0.573	-0.307
c	0.581	0.777	0.815	1.141

Table 6.1: Values of the constant for Equation 6.1

After that a correction factor with equation 6.2 was defined and even this Δq was supposed to be described as only a function of mixture ratio and combustion chamber pressure. Now the corrected heat fluxes could be calculated with equation 6.3.

$$\Delta q = \frac{q_{Thermtest} - q_{correlation}}{q_{correlation}} = x \cdot OF^y \cdot PCC^z \tag{6.2}$$

$$q_{corrected} = \Delta q \cdot q_{Thermtest} \tag{6.3}$$

	Segment 1	Segment 2	Segment 3	Nozzle	Model
x	0.1947	0.4552	0.1502	0.0660	
y	2.0159	0.7005	0.8180	-0.1334	Bishop
z	-0.1880	-0.0116	0.1893	0.4533	
x	0.2966	0.5306	0.1420	0.0566	
y	1.9902	0.6804	0.5689	-0.1678	Krueger
z	-0.2015	-0.0099	0.2598	0.4783	
x	0.3090	0.4707	0.1340	0.0792	
y	2.0941	0.7291	0.9036	-0.3370	Mokry
z	-0.2122	0.0240	0.1734	0.4584	

Table 6.2: Values of the constant for Equation 6.2

Table 6.2 lists the value of the constants of equation 6.2. These three parameters were found minimizing, segmentwise and for each heat transfer coefficient model, the error expressed in equation 6.4.

$$error = \frac{|q_{corrected} - q_{correlation}|}{q_{correlation}} \cdot 100 \tag{6.4}$$

All the calculation that have been carried out to obtain the values of the constants are shown in appendix A.

6.3 Results

Now the heat fluxes will be updated with the calculated correction. In each graph two adjacent bars identify the same heat transfer coefficient model: left for the plain model, right for the corrected one. Each row of the table is relative to one heat transfer coefficient model according to the legend.

6.3.1 20 bar
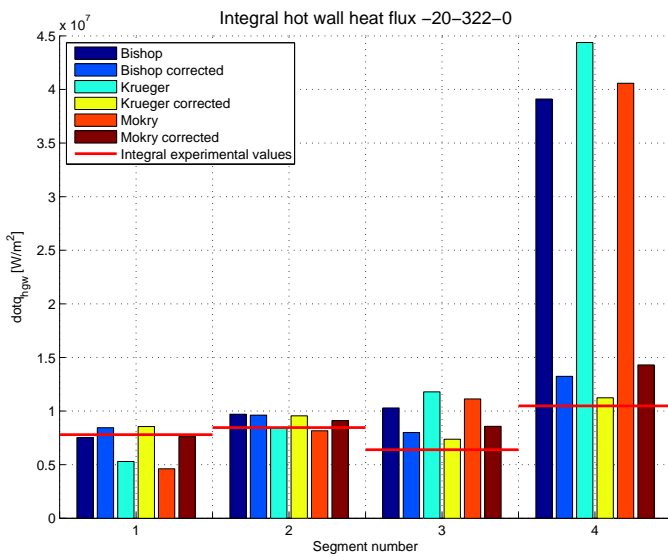
Figure 6.4: Integral hot wall heat flux - 20-322-0
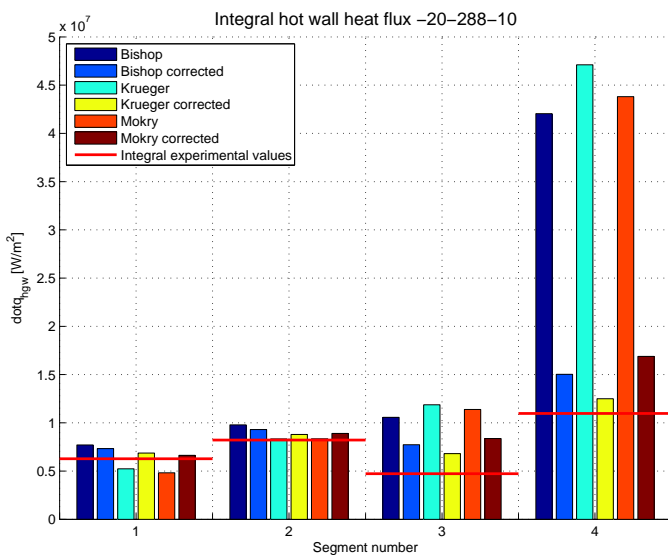
	Segment number			
	1	2	3	4
	-3.56	14.7	60.8	272.9
	8.31	13.8	25.1	26.2
	-32.1	-0.09	84.4	323.2
Error [%]	9.61	12.9	15.3	7.2
	-40.8	-3.5	73.9	286.9
	-2.36	7.8	34.0	36.4

Table 6.3: Error 20-322-0

Figure 6.5: Integral hot wall heat flux - 20-288-10

	Segment number			
	1	2	3	4
	22.8	19.1	123.5	283.4
	16.8	13.2	63.5	37.0
	-16.6	1.4	150.9	329.5
Error [%]	9.3	6.9	43.9	13.9
	-23.1	1.5	140.7	299.4
	5.6	8.3	76.9	54.0

Table 6.4: Error 20-288-10

Figure 6.6: Integral hot wall heat flux - 20-341-20
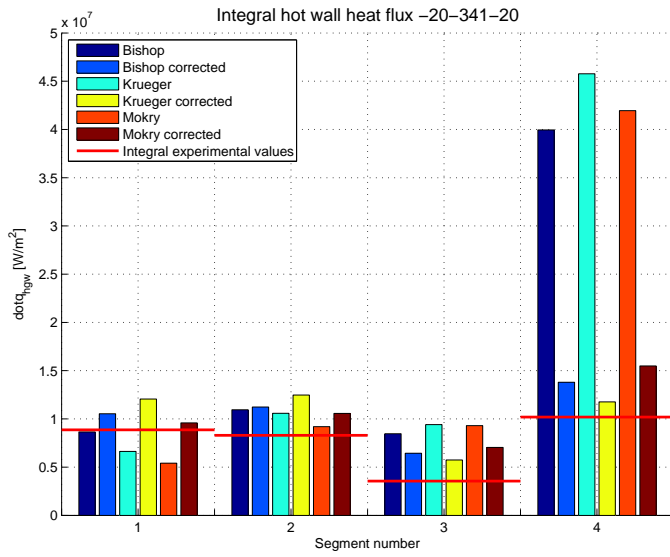
	Segment number			
	1	2	3	4
	-2.3	31.9	137.9	291.9
	18.8	35.3	81.2	35.4
	-25.2	27.5	164.7	349.1
Error [%]	36.0	50.3	61.6	15.4
	38.9	10.8	161.7	311.5
	8.2	27.3	98.2	52.0

Table 6.5: Error 20-341-20

For the 20 bar load points it is possible to note that the impact of the correction of the heat fluxes is clearly visible; all the heat fluxes, in fact, are closer to the experimental results than the plain heat transfer coefficient model, even in the nozzle segment, where the errors were the highest. In the 20-322-0 load point there is a better agreement with the experimental heat fluxes because the correction was tailored on all the load points without film cooling; so it is normal that gives better results with such load points. However in the load points with film cooling the correction has a good behavior too. Moreover Krueger model seems to be the one that better meets the correction: in two out of three load points gives the lowest errors.

6.3.2   40 bar

Figure 6.7: Integral hot wall heat flux - 40-322-0
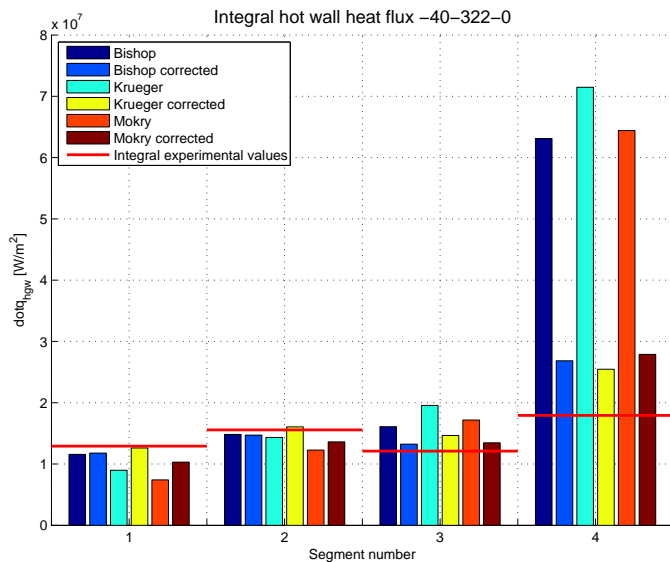
	Segment number			
	1	2	3	4
	-10.4	-4.8	32.9	252.0
	-8.8	-5.4	9.4	49.7
	-30.5	-7.9	61.5	298.7
Error [%]	-2.4	3.2	21.1	42.1
	-42.6	-21.2	41.9	259.2
	-20.3	-12.5	11.2	55.5

Table 6.6: Error 40-322-0

Figure 6.8: Integral hot wall heat flux - 40-288-5
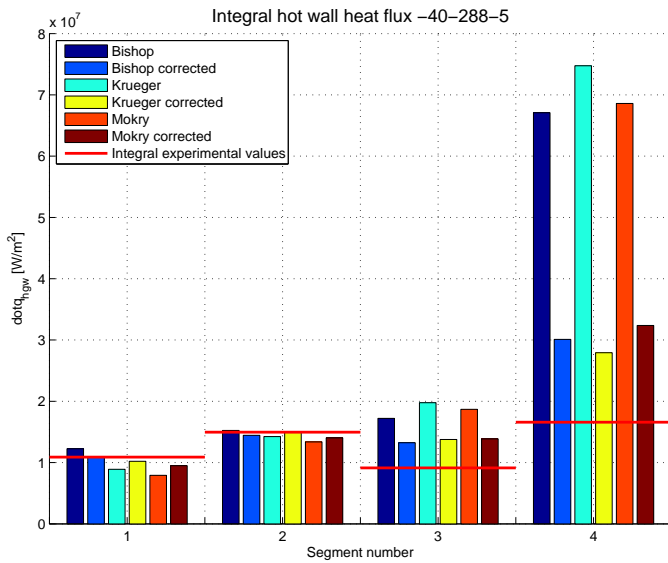
Segment number			
1	2	3	4
12.6	1.9	88.3	304.3
-0.48	-3.3	44.9	81.5
-18.2	-4.8	116.3	350.5
-6.2	-0.4	50.7	68.4
-27.3	-10.6	104.5	313.4
-12.9	-6.2	51.6	95.1

Table 6.7: Error 40-288-5

Figure 6.9: Integral hot wall heat flux - 40-322-15
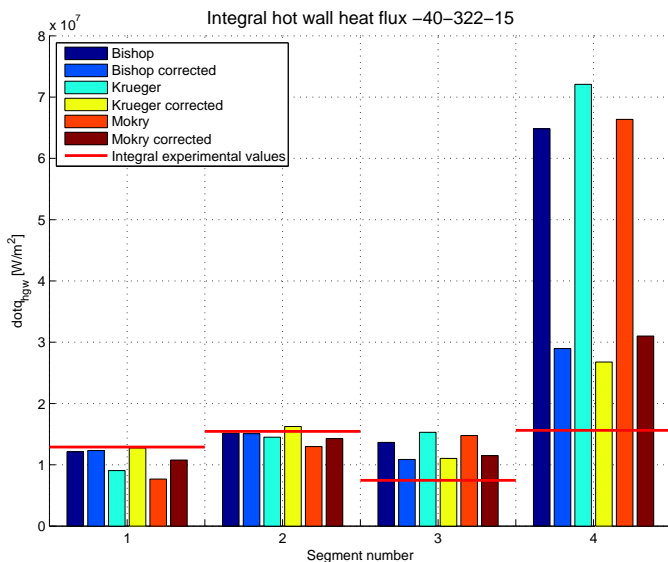
Segment number			
1	2	3	4
-6.0	-1.8	82.9	315.1
-4.3	-2.5	45.6	85.5
-29.7	-6.1	104.9	361.7
-1.1	5.1	47.9	71.4
-40.5	-16.1	97.8	325.0
-16.4	-7.7	54.0	98.6

Table 6.8: Error 40-322-15

Also for 40 bar load points it is possible to see a strong reduction of the errors between experimental and numerical heat fluxes in all the four segments. As in the previous case, the agreement in the no film cooling case is better than in the other load points for the same reasons explained before. The other two load points continue to show unfortunately high error in the range of 50%. In the 40 bar load points, the best simulation of the heat fluxes is the one by Bishop.

6.3.3 60 bar

For the 60 bar load points the same observations of the lower pressure load points can be drawn: even in these cases it is possible to see the important reduction of the heat fluxes especially in the third and fourth segment. The 60-288-0 load point has a better agreement with experimental results than the other load points. in this case the best simulation of heat fluxes is given by Kruger.
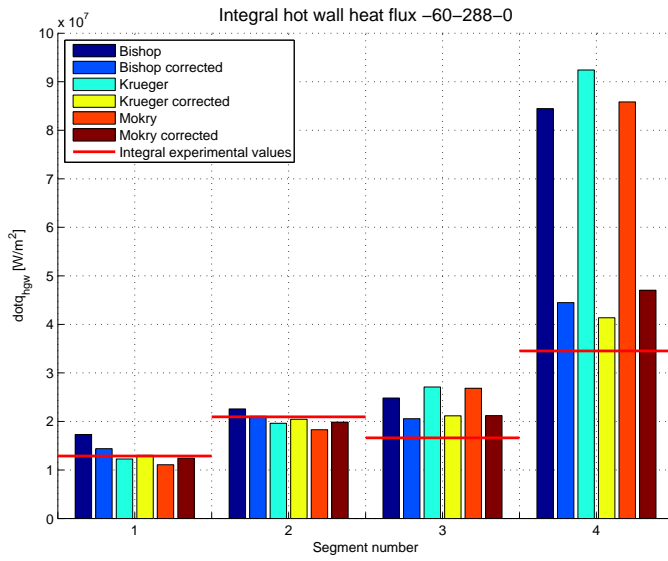
Figure 6.10: Integral hot wall heat flux - 60-288-0

Segment number			
1	2	3	4
34.4	7.8	49.4	144.7
11.9	0.6	23.7	28.8
-4.6	-6.3	63.0	167.7
1.3	-2.3	27.4	19.8
-13.9	-12.6	61.5	148.6
-3.4	-5.2	27.6	36.2

Table 6.9: Error 60-288-0
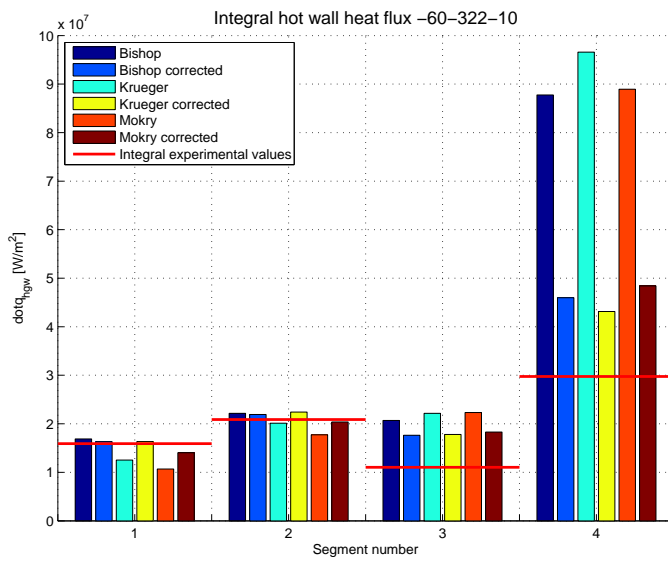
Figure 6.11: Integral hot wall heat flux - 60-322-10

Segment number			
1	2	3	4
6.0	6.1	87.4	195.0
2.4	4.9	59.8	54.6
-21.3	-3.6	100.6	224.7
2.7	7.4	61.3	45.0
-32.9	-15.1	102.3	19.0
-11.8	-2.4	65.7	62.8

Table 6.10: Error 60-322-10

Figure 6.12: Integral hot wall heat flux - 60-322-15
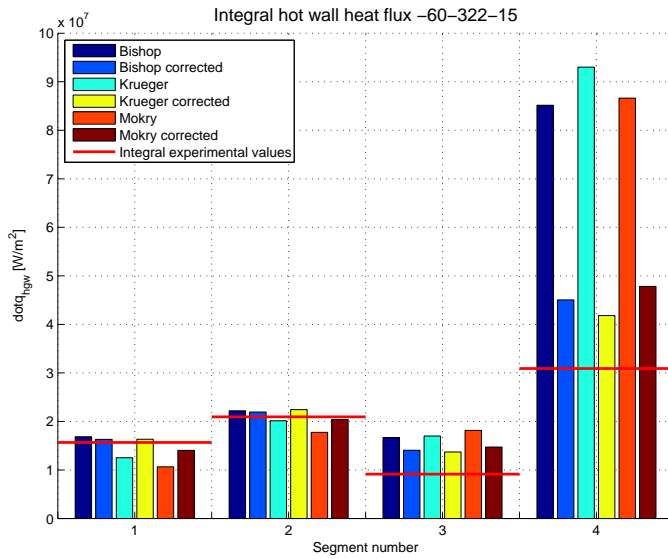
| | Segment number | | | |
---	1	2	3	4
Error [%]	7.6	5.9	82.5	175.5
	4.1	4.7	53.8	45.7
	-20.1	-3.9	86.0	200.8
	4.3	7.1	50.0	35.2
	-31.9	-15.2	99.0	180.2
	-10.4	-2.6	61.1	54.7

Table 6.11: Error 60-322-15

6.3.4 80 bar

Regarding the highest pressure load points it is possible to say that, also in these cases, the correction works in a good way reducing the errors between simulated and experimental heat fluxes. Even in this case the errors remain, however, a little bit high, especially in the third segment: mean errors is around 55%. Krueger is the model that gives the best agreement between experimental and numerical results.

Figure 6.13: Integral hot wall heat flux - 80-288-0
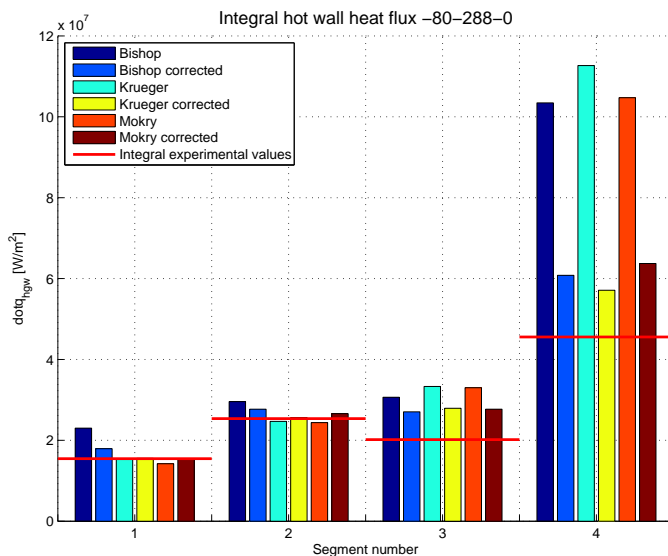
| | Segment number | | | |
---	1	2	3	4
Error [%]	48.8	16.5	51.9	127.1
	16.0	9.2	34.0	33.4
	-0.04	-2.7	65.1	147.3
	0.6	1.1	38.4	25.4
	-8.0	-4.0	63.6	129.9
	-0.6	4.8	37.2	39.2

Table 6.12: Error 80-288-0
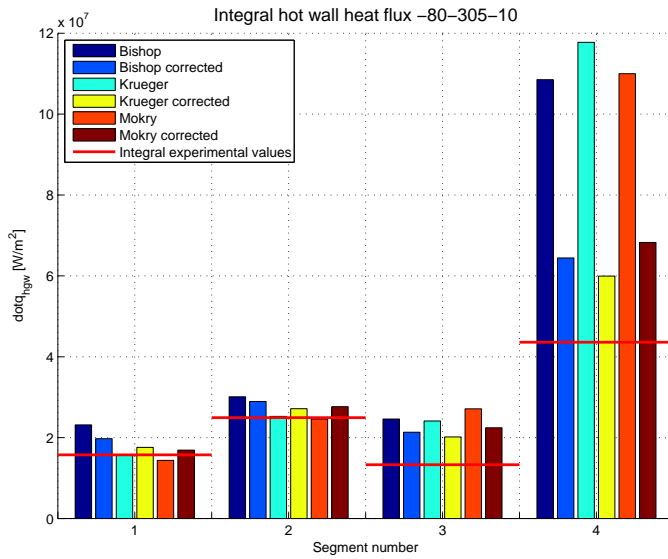
Figure 6.14: Integral hot wall heat flux - 80-305-10

Segment number			
1	2	3	4
47.1	20.7	84.8	148.9
25.5	16.0	60.4	47.8
-0.1	1.3	81.2	170.2
11.7	8.8	51.6	37.6
-8.7	-1.5	103.9	152.4
7.3	10.9	68.7	56.6

Table 6.13: Error 80-305-10
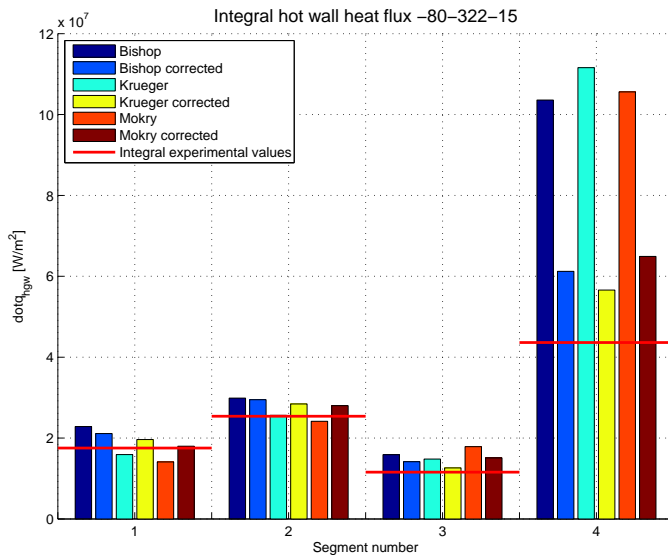
Figure 6.15: Integral hot wall heat flux - 80-322-15

Segment number			
1	2	3	4
30.3	17.7	37.3	137.5
20.5	16.2	22.3	40.4
-9.3	0.88	28.0	155.8
12.0	12.0	9.1	29.8
-19.7	-4.8	54.7	142.1
2.6	10.3	30.6	48.8

Table 6.14: Error 80-322-15

6.4 Conclusions

The implementation of the optimization in the form of heat transfer correction, reduced the errors between experimental and numerical results as expected. Three corrections were developed, one for each of the three heat transfer models left. The corrections do not always work in the same way for all the analyzed load points especially because they were derived only with the load points without film cooling and then applied also to the film cooled cases. Moreover the three corrections work a little bit different from each other: from the previous section it is possible to note that Krueger corrected gives lower error compared with the other models for almost all the analyzed load points. For these reasons Krueger, with its correction, is the model that eventually come out to be the best one to predict the heat fluxes.

Chapter 7

Sensibility analysis

In this chapter a sensibility analysis will be shown, varying some parameters to see the behavior of the heat transfer coefficient and of the film cooling model. First of all there will be the comparison between two different film cooling models: NASA A, which is a pure gaseous model, and NASA B, which is a pure liquid model (see section 4.2). After that the way in which Thermtest calculates the adiabatic wall temperature will be changed. The last analysis will be modify the thickness of the film coolant at its injection point in order to see how much this parameter is important.

7.1   NASA A vs NASA B
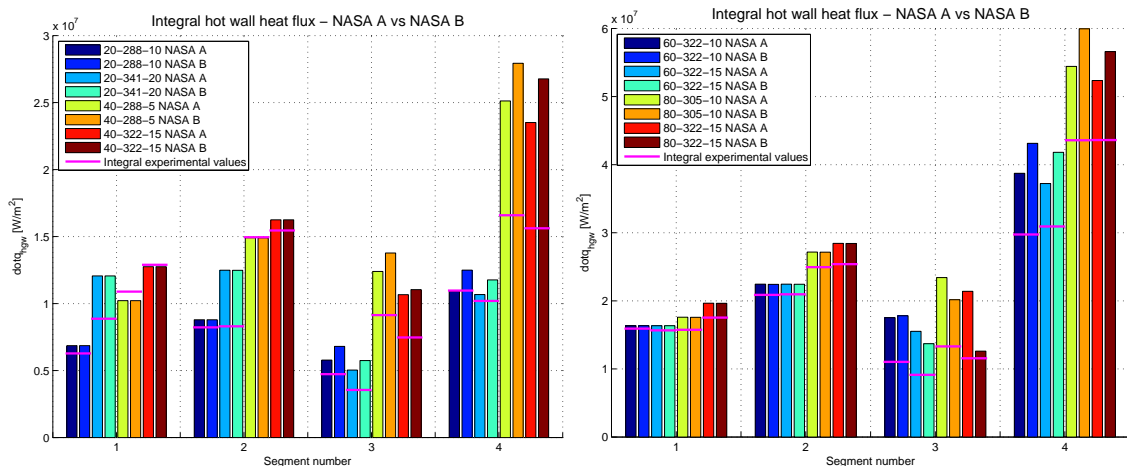
Figure 7.1: NASA A vs NASA B

Figure 7.1 shows the comparison between the NASA A, described in 4.2.1, and NASA B, described in 4.2.2, film cooling model. The important difference between the two is that the first one is a gaseous model while the second is a liquid one. From the graphs it is possible to note that, obviously, the first two segments do not notice the change in the film cooling model, because film cooling injection starts at the beginning of the third segment, while in the third and nozzle segments there are some changes. In particular, at 20 and 40 bar, NASA A gives slightly better results than NASA B; conversely at high pressure, 60 and 80 bar, it is NASA B that gives better agreement with experimental results.

7.2 Adiabatic wall temperature calculation

In NASA B model it is possible to choose two different ways to calculate the adiabatic wall temperature. First one is the so called "NASA B temperature", defined in [10], and shown in equation 7.1 for clarity; second one comes from the definition of film cooling effectiveness (equation 7.2) and for this reason referred to as "NASA B effectiveness temperature" .

$$T_{aw} = \frac{H_{aw} - \eta H_{c,sv} + \eta c_{p_v} T_{if} + (1 - \eta)\left(c_{p_e} T_{tot,e} - H_e\right)}{\eta c_{p_v} + (1 - \eta) c_{p_e}} \tag{7.1}$$

$$T_{aw} = T_{rec} - \eta\left(T_{rec} - T_{film}\right) \tag{7.2}$$
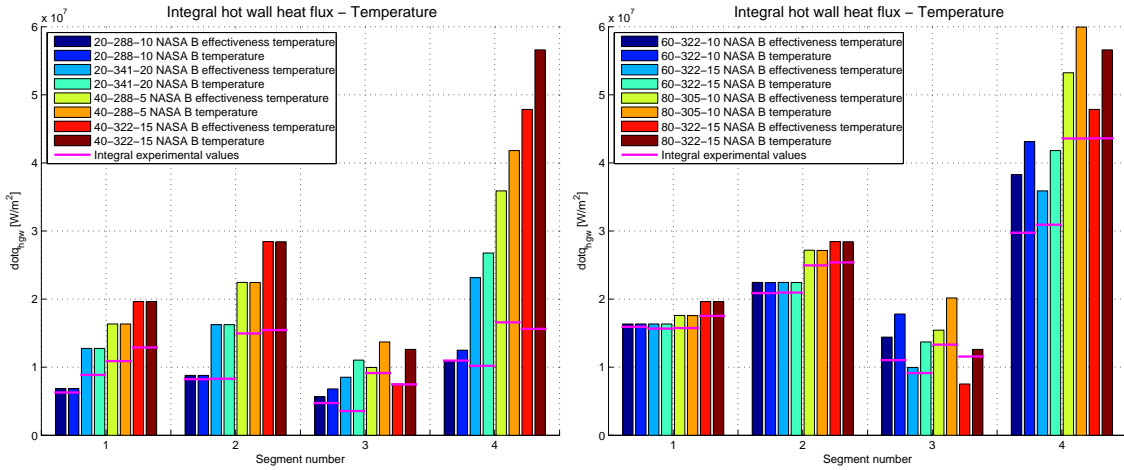
Figure 7.2: Adiabatic wall temperature comparison

In figure 7.2 there is the comparison between the heat fluxes calculated with the two different temperatures. First two segments are not affected by this change, instead the third and fourth segments show that for all the load points investigated the "NASA B effectiveness temperature" gives heat fluxes closer to the experimental results than the other way of calculate the temperature.

7.3 Film coolant thickness
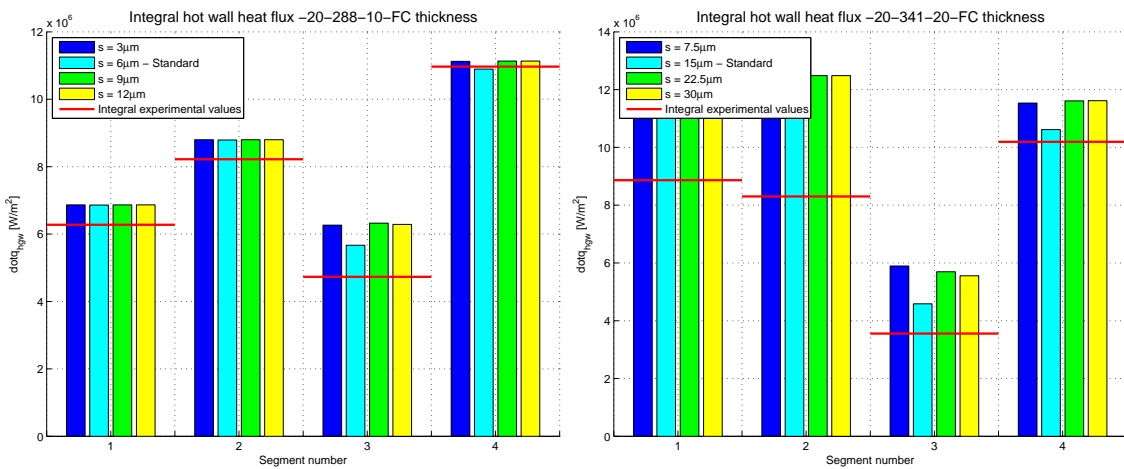
Figure 7.3: Film coolant thickness - 20 bar
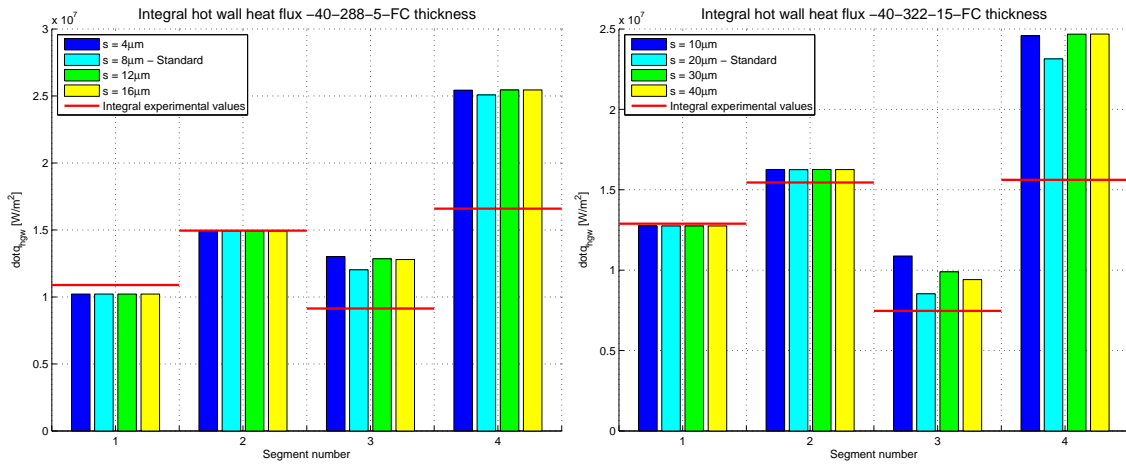
Figure 7.4: Film coolant thickness - 40 bar
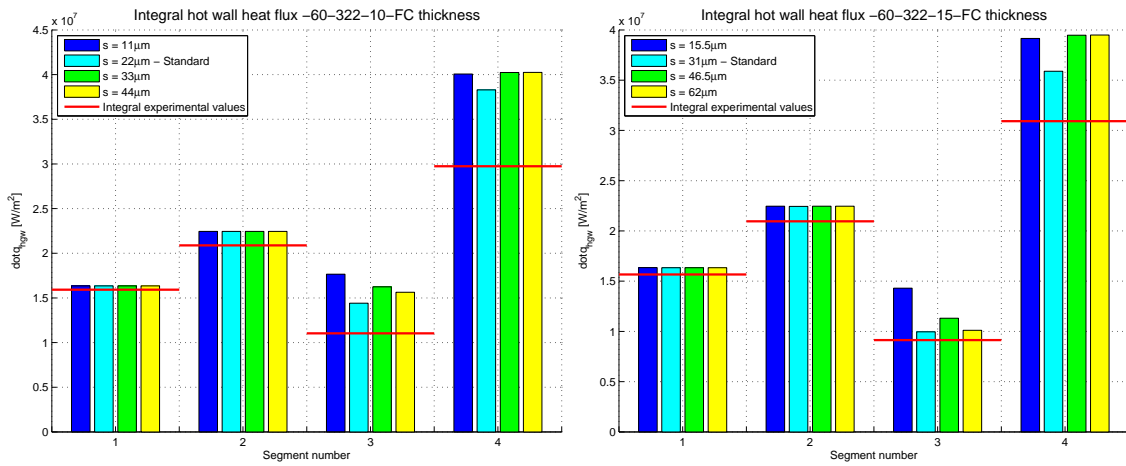
Figure 7.5: Film coolant thickness - 60 bar
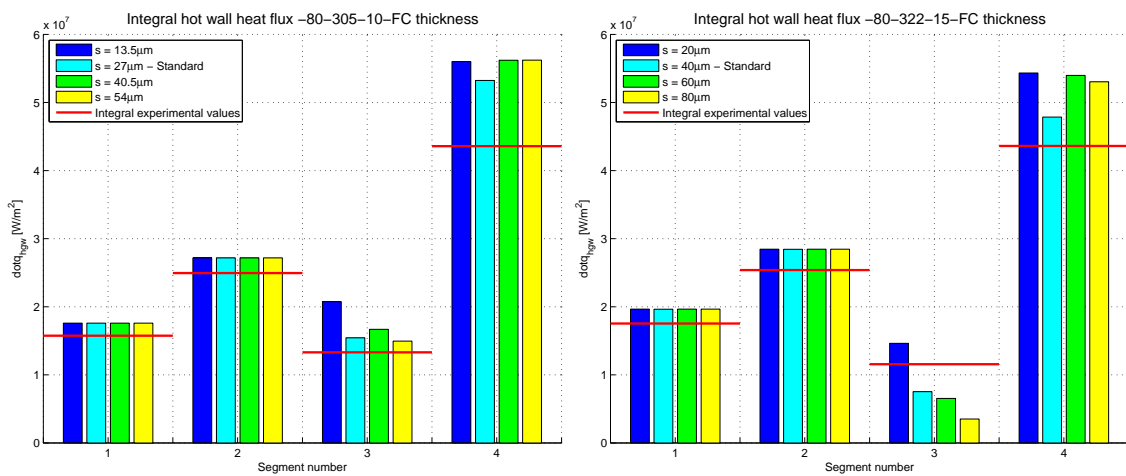
Figure 7.6: Film coolant thickness - 80 bar

Figures 7.3, 7.4, 7.5 and 7.6 show the sensibility of the hot wall heat fluxes to the change of the film coolant thickness. In each picture four different thicknesses are investigated: the cyan bar represent the standard thickness, automatically calculated thanks to a Thermtest feature, the blue bar is half, the green bar is one and a half time and the yellow bar is twice the standard thickness.

Obviously, because film cooling is not present, in the first two segments heat fluxes are the same for every thickness examined. In the third and fourth segment, instead, changing in film cooling thickness results in a change of the heat fluxes. The difference, however, are not so significant, except for 20-341-20 and 80-322-15 load points, and the standard thickness is the one that gives the best agreement with experimental results.

7.4 Conclusions

In this chapter a sensibility analysis to different parameter was conducted. Regarding the first parameter, the film cooling model, from the investigations conducted it is possible to say that at low pressure a gaseous film cooling model (NASA A) is more accurate than a liquid one; at high pressure, instead, NASA B model gives better agreement than NASA A. A possible explanation of this behavior is that injected kerosene is supercritical and both the models cannot reproduce correctly this situation. Moreover, after a certain length, the film cooled length, the coolant is not anymore liquid, but it is fully vaporized but NASA B model still consider the coolant liquid. It could be possible to have a better prediction if a mix of the two models, liquid and gaseous, will be implemented.

Concerning the second parameter, for all the load point investigated, calculating the adiabatic wall temperature with the film cooling effectiveness definition give better results than the other NASA B formula.

About the third parameter, film coolant thickness, it is possible to say that heat fluxes are not so sensitive to the changes of this parameter. An exception in the last load point (80-322-15) where the differences are significant; a possible explanation is that this load point is beyond the limits of applicability of film cooling and heat transfer coefficient model. This result also endorses the way film coolant thickness is calculated; Thermtest simulate the injection of the coolant from a slot but in TUM-LFA combustion chamber film coolant is applied by a film applicator and a proper slot height does not exists. Therefore even if Thermtest is not predicting correctly the film coolant thickness, this does not lead to significant errors in heat fluxes prediction.

Chapter 8

Water film cooling test simulation

In this chapter the results of the simulation of test with water as film coolant will be shown. First of all the equation to calculate important water properties that Thermtest needs as parameter will be presented. Then the results of this implementation are shown. In this chapter there will not be the comparison with experimental results because they are not available yet. These simulations were conducted in order to have an idea of which level of heat fluxes are to be expected during the experimental tests. At the end a comparison between kerosene and water as film coolant will be conducted.

8.1 Water properties

Before simulating the tests with water as film coolant, Thermtest has to be adjusted in order that it will be able to calculate water properties. Scrolling through the code it is possible to note that the three properties that need to be calculate are: saturation temperature, vaporization enthalpy and surface tension.

The equations describing this properties as a function of temperature or pressure were developed by the International Association for the Properties of Water and Steam (IAPWS). The IAPWS is an international non-profit association of nationals organizations concerned with the properties of water and steam, particularly thermophysical properties and other aspects of high temperature steam, water and aqueous mixture that are relevant to thermal power cycles and other industrial applications.

8.1.1 Saturation temperature

The correlation to calculate water saturation temperature is given in [23] and shown in equation 8.1; it allows the calculation of T_{sat} knowing only saturation pressure.

$$T_{sat} = \frac{n_{10} + D - \left[(n_{10} + D)^2 - 4 \cdot (n_9 + n_{10} \cdot D)\right]^{0.5}}{2} \tag{8.1}$$

where

$$D = \frac{2 \cdot G}{-F - (F^2 - 4 \cdot E \cdot G)^{0.5}} \tag{8.2a}$$

$$F = n_1 \beta^2 + n_4 \beta + n_7 \tag{8.2c}$$

$$G = n_2 \beta^2 + n_5 \beta + n_8 \tag{8.2d}$$

$$E = \beta^2 + n_3 \beta + n_6 \tag{8.2b}$$

$$\beta = P_{sat}^{0.25} \tag{8.2e}$$

The range of validity of these equations is: $611.213\,Pa \leq P \leq 22.064\,MPa$.

The values of the constants n_i are shown in table 8.1.

i	n_i	i	n_i
1	$0.11670521452767 \cdot 10^4$	6	$0.14915108613530 \cdot 10^2$
2	$-0.72421316703206 \cdot 10^6$	7	$-0.48232657361591 \cdot 10^4$
3	$-0.17073846940092 \cdot 10^2$	8	$0.40511340542057 \cdot 10^6$
4	$0.12020824702470 \cdot 10^5$	9	$-0.23855557567849 \cdot 10^0$
5	$-0.32325550322333 \cdot 10^7$	10	$0.65017534844798 \cdot 10^3$

Table 8.1: Numerical values of the coefficients for the calculation of saturation temperature

8.1.2   Vaporization enthalpy

Equation 8.3, derived in [20] and [22], allows the calculation of the water vaporization enthalpy between the triple point and the critical point of water ($273.16\,K \leq T \leq 647.096\,K$).

$$h_{vap} = h_{sv} - h_{s,\,liq} = \left(\frac{1}{\rho_{sv}} - \frac{1}{\rho_{s,\,liq}} \right) \cdot \frac{dP}{dT} \cdot T \tag{8.3}$$

where

$$\ln \left(\frac{P}{P_{crit}} \right) = \frac{T_{crit}}{T} \left(a_1 \tau + a_2 \tau^{1.5} + a_3 \tau^3 + a_4 \tau^{3.5} + a_5 \tau^4 + a_6 \tau^{7.5} \right) \tag{8.4}$$

$$\frac{\rho_{s,\,liq}}{\rho_{crit}} = 1 + b_1 \tau^{1/3} + b_2 \tau^{2/3} + b_3 \tau^{5/3} + b_4 \tau^{16/3} + b_5 \tau^{43/3} + b_6 \tau^{110/3} \tag{8.5}$$

$$\frac{\rho_{sv}}{\rho_{crit}} = c_1 \tau^{2/6} + c_2 \tau^{4/6} + c_3 \tau^{8/6} + c_4 \tau^{18/6} + c_5 \tau^{37/6} + c_6 \tau^{71/6} \tag{8.6}$$

with

$$T_{crit} = 647.096\,K \tag{8.7a}$$

$$\rho_{crit} = 322\,\frac{kg}{m^3} \tag{8.7c}$$

$$P_{crit} = 22.064\,MPa \tag{8.7b}$$

$$\tau = 1 - \frac{T}{T_{crit}} \tag{8.7d}$$

The values of the constants used in equations 8.4, 8.5 and 8.6 are shown in table 8.2.

i	a_i	b_i	c_i
1	-7.85951783	1.99274064	-2.03150240
2	1.84408259	1.09965342	-2.68302940
3	-11.7866497	-0.51083930	-5.38626492
4	22.6807411	-1.75493479	-17.2991605
5	-15.9618719	-45.5170352	-44.7586581
6	1.80122502	$-6.74694450 \cdot 10^5$	-63.9201063

Table 8.2: Numerical values of the coefficients for the calculation of vaporization enthalpy

8.1.3 Surface tension

Water surface tension is calculated with equation 8.8; it is an interpolating equation of the corrected 1975 experimental results, shown in [21].

$$\sigma = B \cdot \tau^{\mu} \cdot (1 + b\tau) \tag{8.8}$$

where

$$\tau = 1 - \frac{T}{T_{crit}} \tag{8.9a}$$

$$b = -0.625 \tag{8.9d}$$

$$T_{crit} = 647.096 \, K \tag{8.9b}$$

$$B = 235.8 \, \frac{mN}{m} \tag{8.9c}$$

$$\mu = 1.256 \tag{8.9e}$$

Equation 8.8 is valid between water triple point $(273.16 \, K)$ and reference temperature T_{crit}.

8.2 Results

In this section the results of the implementation of water as film coolant in Thermtest are shown. Figure 8.1 shows the results of foreseen load point because the experimental results are not available yet. Simulation were conducted at the same pressure, 20 *bar*, with three different mixture ratio focusing on what happen to the heat fluxes increasing the film coolant mass flow rate.

Because experimental values of the input parameters that Thermtest needs to run are not available, the same values of kerosene, for each load point investigated, were used; the only modification, of course, was changing the film coolant from kerosene to water.
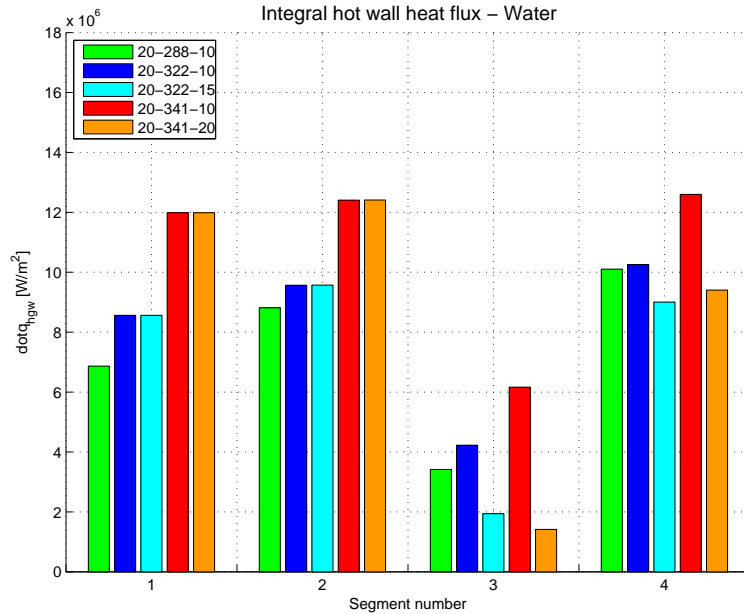
Figure 8.1: Integral hot wall heat flux - Water

Figure 8.1 shows that heat fluxes increase when increasing the mixture ratio; in the first two segments modifications in the film coolant mass flow do not results in a reduction of the heat fluxes. In the third and fourth segments, as expected, an increase in heat capacity results in a decrease in the heat fluxes.

8.2.1   Comparison with kerosene

In this section two of the fictitious load points will be compared with their respective kerosene load points, analyzed in chapter 5. Figure 8.2 shows this comparison.
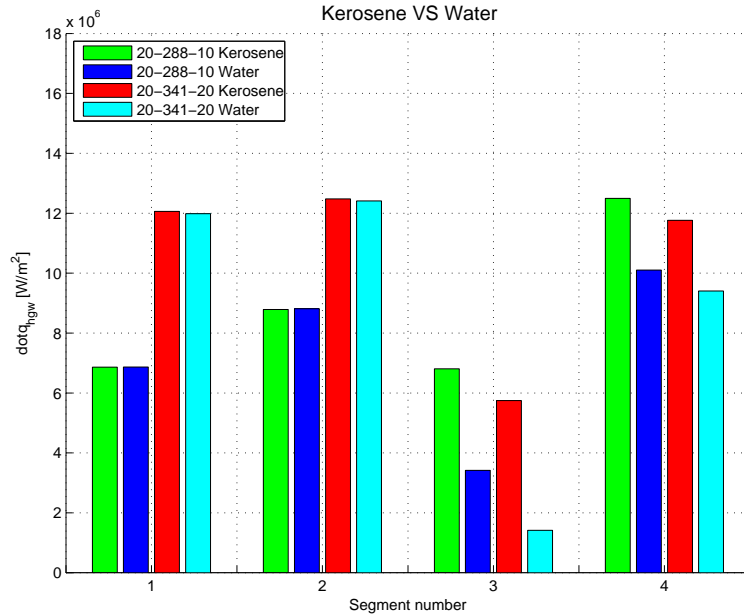
Figure 8.2: Integral hot wall heat flux - Kerosene vs Water

In the first two segments heat fluxes are not affected by the type of the film coolant, this is correct because the first two segments are not film cooled. In the third and nozzle segments water load points show constantly lower heat fluxes than kerosene. In particular table 8.3 shows the percentage reduction of the heat fluxes changing film coolant from kerosene to water.

ID	% reduction	
	Segment 3	Segment 4
20-288-10	-49.80	-19.14
20-341-20	-75.34	-20.05

Table 8.3: Heat fluxes percentage reduction

8.3   Conclusions

In this chapter simulation of the tests with water as film coolant were presented. Thermtest was adjusted in order to calculate the correct values of water properties. From the implementation it is clear that heat flux levels, when water is used as film coolant, are lower than in the case with kerosene. Therefore water has a better cooling power than kerosene, in fact, water's heat capacity is higher than kerosene so water is capable to receive a high amount of heat than kerosene before being completely vaporized.

Chapter 9

Conclusions and future developments

9.1 Conclusions

Within this thesis work an analysis of the main film cooling aspects has been performed, different papers and previous works about this technique, either experimental or theoretical have been reviewed. Six new turbulent heat transfer models and one liquid film cooling model were implemented and compared to the already implemented Cinjarew heat transfer model and NASA B film cooling model.

The Stechman film cooling model do not give better results than the old NASA B model, so it was discarded. New heat transfer coefficient models were investigated in order to have more than one model that correctly predicts the heat fluxes so that prediction can be more reliable. Moreover Cinjarew model was developed by Russians specifically for kerosene and it could be possible that, in view of changing the type of fuel (from kerosene to methane) and film coolant (from kerosene to water or argon), it will not give anymore so precise simulations.

However, none of the plain heat transfer coefficient models gave satisfactory results especially in the film cooled segments. The highest errors were in the nozzle segments, where the wall curvature, the high speed involved and thus the complex mixing phenomena, lead to high overprediction of the experimental results for all the models investigated. Even in the third segment the experimental heat fluxes where constantly overestimated and so a correction and a optimization of the three models that gave better agreement in the first two segments were developed.

Bishop, Krueger and Mokry model were corrected and optimized for mixture ratio and combustion chamber pressure. The corrected model were then compared again with experimental results and Krueger turns out to be the best model to predict the heat fluxes in the TUM-LFA combustion chamber, even if the errors remain sometimes above 20%.

After that, a sensibility analysis to some parameters, as film cooling model, adiabatic wall temperature calculation and film cooling thickness, was conducted. Regarding film cooling model, conflicting results were found: at low pressure NASA A, a gaseous model, gives the best results, at high pressure, instead, the closer prediction to the experimental results is the one made by NASA B, a liquid model. It could be possible that a mix between liquid and gaseous film cooling model could give better agreement with experimental results. Comparing the two ways of calculating adiabatic wall temperature was found out that determining adiabatic wall temperature with effectiveness definition gives always better results than "NASA B temperature". Finally film coolant injection thickness does not play a so important role in hot wall heat flux determination: halving and doubling that thickness leads to almost the same results as the reference thickness.

So even if in Thermtest the film coolant is supposed to be injected by a slot but in reality the film coolant applicator imposes a swirl motion in TUM-LFA combustion chamber, this does not imply big differences in heat fluxes levels.

Finally Kruger model corrected was used to simulate tests with water as film coolant and, as expected, water is confirmed to have a better cooling power than kerosene, especially because of its higher heat capacity.

9.2   Future developments

From the numerical point of view improvements in heat flux prediction could be achieved studying and implementing a peculiar film cooling model in the nozzle, implementing a mixed liquid and gaseous film cooling model and start to consider chemical reaction.

The distinctive feature of a nozzle flow are the significant acceleration in the convergent part, high levels of heat fluxes in the throat region, high curvature and effect due to the compressibility in the supersonic tract. A nozzle film cooling model could be found and then implemented to improve prediction in the fourth segment of the combustion chamber.

Another enhancement of heat transfer predictions could be the implementation of a pure liquid film cooling model and then, after a certain length, the film cooled length, when the coolant will be completely vaporized, start with a gaseous film cooling model; in this way what is actually happening in the combustion chamber will be modeled: after a certain length liquid film coolant is, in fact, completely evaporated.

Finally, implementing chemical reaction will lead to an improvement of the prediction even if this could cause the increase of the implementation complexity and the running time.

Appendix A

Optimization

In the next pages the calculations for obtaining the corrections described in chapter 6 are shown. In the upper left part of the page the name of the heat transfer coefficient under investigation is given and in the upper right part there are the values for the constants a, b, and c, coming out from a regression with all the experimental load points without film cooling, to calculate the correlated heat fluxes $q_{correlation}$. These particular heat fluxes are the base over which the corrections were calculated. All the matrices show the values described in the subsequent list for each pressure, film cooling percentage and segmentwise.

1. *Correlation*: this matrix shows the values of the heat fluxes calculated with $q_{correlation} = a \cdot OF^b \cdot PCC^c$;

2. $q_{Thermtest}$: this matrix shows the values of the simulated heat fluxes calculated with thermtest with one of these heat transfer coefficient model: Bishop, Krueger and Mokry;

3. Δq: this matrix shows the values of the error between Thermtest and correlated heat fluxes. Under this matrix there are the values of the constants, calculated minimizing *error* (see point 7 of this list) that are used to calculate the actual correction that modifies the heat fluxes in Thermtest implementation.

4. *Deviation*: this matrix shows the values of the error Δq in terms of percentuals;

5. $\Delta q_{regression}$: this matrix shows the the values of Δq calculated with: $\Delta q_{regression} = x \cdot OF^y \cdot PCC^z$;

6. q: this matrix shows the values of the corrected Thermtest heat fluxes.

7. *error*: This matrix shows, in percentage, the error between the corrected and the correlaeted heat fluxes. This is the error that it is minimized to obtain the values of the canstant x, y and z used to calculate Δq;

8. *Standard deviation of experimental values*: this matrix shows the standard deviation of experimantal values, in order to have a comparison between this deviation and the one calculated after the correction.

Bishop

Factors		Segment 1	Segment 2	Segment 3	Nozzle
	a	128469.503	332159.890	315499.222	413545.713
	b	2.127	0.892	0.573	-0.307
	c	0.581	0.777	0.815	1.141

$$\dot{q}_{correlation} = a \cdot OF^b \cdot PCC^c$$

Correlation · $\dot{q}_{Thermtest}$ · $\Delta\dot{q} = \dfrac{|\dot{q}_{Thermtest} - \dot{q}_{correlation}|}{\dot{q}_{correlation}}$ · Deviation (%)

OF [-]	PCC [bar]	μ [%]	QAK1 [W/m²]	QAK2 [W/m²]	QAK3 [W/m²]	QAD [W/m²]	QAK1 [W/m²]	QAK2 [W/m²]	QAK3 [W/m²]	QAD [W/m²]	ΔQAK1 [W/m²]	ΔQAK2 [W/m²]	ΔQAK3 [W/m²]	ΔQAD [W/m²]	ΔQAK1 [%]	ΔQAK2 [%]	ΔQAK3 [%]	ΔQAD [%]
2.88	20	10	6.9486E+06	8.7619E+06	6.6518E+06	9.1346E+06	7.707E+06	9.790E+06	1.057E+07	4.205E+07	0.1092	0.1173	0.5895	3.6034	10.92	11.73	58.95	360.34
3.07	20	20	7.9597E+06	9.2757E+06	6.8997E+06	8.9574E+06	7.598E+06	9.695E+06	8.690E+06	4.043E+07	0.0454	0.0452	0.2595	3.5137	4.54	4.52	25.95	351.37
3.41	20	20	9.9519E+06	1.0187E+07	7.3274E+06	8.6736E+06	8.659E+06	1.095E+07	8.458E+06	3.995E+07	0.1300	0.0753	0.1543	3.6059	13.00	7.53	15.43	360.59
3.22	20	0	8.8096E+06	9.6788E+06	7.0908E+06	8.8274E+06	7.524E+06	9.703E+06	1.029E+07	3.910E+07	0.1459	0.0025	0.4506	3.4299	14.59	0.25	45.06	342.99
2.88	40	5	1.0396E+07	1.5019E+07	1.1706E+07	2.0151E+07	1.226E+07	1.524E+07	1.721E+07	6.707E+07	0.1791	0.0146	0.4701	2.3286	17.91	1.46	47.01	232.86
2.9	40	15	1.0550E+07	1.5112E+07	1.1752E+07	2.0108E+07	1.224E+07	1.524E+07	1.377E+07	6.474E+07	0.1604	0.0084	0.1715	2.2196	16.04	0.84	17.15	221.96
3.22	40	15	1.3180E+07	1.6591E+07	1.2478E+07	1.9473E+07	1.212E+07	1.517E+07	1.366E+07	6.482E+07	0.0805	0.0854	0.0945	2.3288	8.05	8.54	9.45	232.88
3.22	40	0	1.3180E+07	1.6591E+07	1.2478E+07	1.9473E+07	1.158E+07	1.482E+07	1.609E+07	6.312E+07	0.1212	0.1067	0.2897	2.2413	12.12	10.67	28.97	224.13
2.9	60	10	1.3353E+07	2.0713E+07	1.6357E+07	3.1942E+07	1.729E+07	2.263E+07	2.100E+07	8.720E+07	0.2951	0.0927	0.2838	1.7299	29.51	9.27	28.38	172.99
3.22	60	10	1.6682E+07	2.2740E+07	1.7368E+07	3.0933E+07	1.687E+07	2.216E+07	2.069E+07	8.775E+07	0.0113	0.0256	0.1912	1.8368	1.13	2.56	19.12	183.68
3.22	60	15	1.6682E+07	2.2740E+07	1.7368E+07	3.0933E+07	1.686E+07	2.219E+07	1.668E+07	8.516E+07	0.0108	0.0240	0.0396	1.7532	1.08	2.40	3.96	175.32
2.88	60	0	1.3158E+07	2.0585E+07	1.6293E+07	3.2010E+07	1.730E+07	2.259E+07	2.483E+07	8.448E+07	0.3150	0.0972	0.5242	1.6391	31.50	9.72	52.42	163.91
2.75	80	10	1.4098E+07	2.4706E+07	2.0063E+07	4.5086E+07	2.379E+07	3.075E+07	2.451E+07	1.074E+08	0.6877	0.2446	0.2217	1.3831	68.77	24.46	22.17	138.31
3.05	80	10	1.7570E+07	2.7096E+07	2.1288E+07	4.3677E+07	2.315E+07	3.012E+07	2.459E+07	1.085E+08	0.3175	0.1115	0.1549	1.4842	31.75	11.15	15.49	148.42
3.22	80	15	1.9719E+07	2.8439E+07	2.1960E+07	4.2957E+07	2.284E+07	2.987E+07	1.587E+07	1.036E+08	0.1585	0.0504	0.2772	1.4109	15.85	5.04	27.72	141.09
2.88	80	0	1.5553E+07	2.5745E+07	2.0600E+07	4.4452E+07	2.300E+07	2.956E+07	3.065E+07	1.034E+08	0.4786	0.1480	0.4880	1.3272	47.86	14.80	48.80	132.72

x	0.1947	0.4552	0.1502	0.0660
y	2.0159	0.7005	0.8180	-0.1334
z	-0.1880	-0.0116	0.1893	0.4533

$$\Delta\dot{q} = x \cdot OF^y \cdot PCC^z$$

$\Delta\dot{q}_{regression}$ · $\dot{q} = \Delta\dot{q}_{regression} \cdot \dot{q}_{Thermtest}$ · $error = \dfrac{|\dot{q} - \dot{q}_{correlation}|}{\dot{q}_{correlation}} \cdot 100$ · Standard deviation of experimental values

OF [-]	PCC [bar]	μ [%]	QAK1 [W/m²]	QAK2 [W/m²]	QAK3 [W/m²]	QAD [W/m²]	QAK1 [W/m²]	QAK2 [W/m²]	QAK3 [W/m²]	QAD [W/m²]	QAK1 [%]	QAK2 [%]	QAK3 [%]	QAD [%]	QAK1 [%]	QAK2 [%]	QAK3 [%]	QAD [%]
2.88	20	10	9.3496E-01	9.2241E-01	6.2922E-01	2.2284E-01	7.2058E+06	9.0300E+06	6.6529E+06	9.3705E+06	3.70	3.06	0.02	2.58	2.00	0.40	2.00	0.50
3.07	20	20	1.0635E+00	9.6463E-01	6.6297E-01	2.2095E-01	8.0804E+06	9.3517E+06	5.7613E+06	8.9333E+06	1.52	0.82	16.50	0.27	1.70	0.60	12.30	9.30
3.41	20	20	1.3143E+00	1.0383E+00	7.2246E-01	2.1787E-01	1.1380E+07	1.1372E+07	6.1107E+06	8.7040E+06	14.35	11.64	16.60	0.35	1.70	0.60	12.30	9.30
3.22	20	0	1.1708E+00	9.9741E-01	6.8936E-01	2.1955E-01	8.8096E+06	9.6779E+06	7.0908E+06	8.5853E+06	0.00	0.01	0.00	2.74	2.50	1.60	2.00	10.20
2.88	40	5	8.2070E-01	9.1505E-01	7.1743E-01	3.0510E-01	1.0060E+07	1.3944E+07	1.2346E+07	2.0464E+07	3.23	7.16	5.47	1.56	2.90	1.20	7.10	10.70
2.9	40	15	8.3223E-01	9.1949E-01	7.2150E-01	3.0482E-01	1.0188E+07	1.4013E+07	9.9336E+06	1.9734E+07	3.43	7.27	15.48	1.86	1.50	1.10	12.00	14.40
3.22	40	15	1.0277E+00	9.8945E-01	7.8600E-01	3.0059E-01	1.2455E+07	1.5014E+07	1.0735E+07	1.9485E+07	5.50	9.51	13.97	0.06	1.50	1.10	12.00	14.40
3.22	40	0	1.0277E+00	9.8945E-01	7.8600E-01	3.0059E-01	1.1903E+07	1.4665E+07	1.2649E+07	1.8973E+07	9.69	11.61	1.37	2.57	4.10	1.70	1.00	20.10
2.9	60	10	7.7113E-01	9.1520E-01	7.7905E-01	3.6632E-01	1.3336E+07	2.0713E+07	1.6360E+07	3.1942E+07	0.13	0.00	0.02	0.00	2.80	2.10	3.30	11.10
3.22	60	10	9.5229E-01	9.8482E-01	8.4869E-01	3.6124E-01	1.6065E+07	2.1821E+07	1.7558E+07	3.1699E+07	3.70	4.04	1.09	2.47	2.80	2.10	3.30	11.10
3.22	60	15	9.5229E-01	9.8482E-01	8.4869E-01	3.6124E-01	1.6057E+07	2.1858E+07	1.4157E+07	3.0764E+07	3.75	3.88	18.49	0.55	5.20	0.30	3.40	3.60
2.88	60	0	7.6045E-01	9.1077E-01	7.7465E-01	3.6666E-01	1.3158E+07	2.0572E+07	1.9237E+07	3.0974E+07	0.00	0.07	18.07	3.24	6.80	4.30	4.40	15.80
2.75	80	10	6.5635E-01	8.7885E-01	7.8767E-01	4.2031E-01	1.5616E+07	2.7023E+07	1.9306E+07	4.5160E+07	10.77	9.38	3.77	0.16	1.50	1.40	6.40	11.80
3.05	80	10	8.0870E-01	9.4496E-01	8.5729E-01	4.1454E-01	1.8721E+07	2.8461E+07	2.1078E+07	4.4979E+07	6.55	5.04	0.99	2.98	1.50	1.40	6.40	11.80
3.22	80	15	9.0214E-01	9.8155E-01	8.9619E-01	4.1155E-01	2.0608E+07	2.9320E+07	1.4224E+07	4.2623E+07	4.51	3.10	35.22	0.78	3.30	1.90	8.40	9.10
2.88	80	0	7.2040E-01	9.0775E-01	8.1800E-01	4.1772E-01	1.6567E+07	2.6830E+07	2.5074E+07	4.3212E+07	6.52	4.21	21.72	2.79	6.70	2.20	2.90	10.80
							Sum				77.33	80.79	168.78	24.96				

Krueger

Factors	Segment 1	Segment 2	Segment 3	Nozzle
a	128469.503	332159.890	315499.222	413545.713
b	2.127	0.892	0.573	-0.307
c	0.581	0.777	0.815	1.141

$$\dot{q}_{correlation} = a \cdot OF^b \cdot PCC^c$$

Correlation | $\dot{q}_{Thermtest}$ | $\Delta\dot{q} = \dfrac{|\dot{q}_{Thermtest} - \dot{q}_{correlation}|}{\dot{q}_{correlation}}$ | Deviation (%)

OF [-]	PCC [bar]	μ [%]	QAK1 [W/m²]	QAK2 [W/m²]	QAK3 [W/m²]	QAD [W/m²]	QAK1 [W/m²]	QAK2 [W/m²]	QAK3 [W/m²]	QAD [W/m²]	ΔQAK1 [W/m²]	ΔQAK2 [W/m²]	ΔQAK3 [W/m²]	ΔQAD [W/m²]	ΔQAK1 [%]	ΔQAK2 [%]	ΔQAK3 [%]	ΔQAD [%]
2.88	20	10	6.9486E+06	8.7619E+06	6.6518E+06	9.1346E+06	5.231E+06	8.332E+06	1.187E+07	4.711E+07	0.2471	0.0490	0.7845	4.1569	24.71	4.90	78.45	415.69
3.07	20	20	7.9597E+06	9.2757E+06	6.8997E+06	8.9574E+06	5.267E+06	8.396E+06	9.312E+06	4.495E+07	0.3383	0.0949	0.3497	4.0176	33.83	9.49	34.97	401.76
3.41	20	20	9.9519E+06	1.0187E+07	7.3274E+06	8.6736E+06	6.631E+06	1.058E+07	9.412E+06	4.578E+07	0.3337	0.0388	0.2845	4.2777	33.37	3.88	28.45	427.77
3.22	20	0	8.8096E+06	9.6788E+06	7.0908E+06	8.8274E+06	5.295E+06	8.449E+06	1.179E+07	4.438E+07	0.3990	0.1270	0.6633	4.0273	39.90	12.70	66.33	402.73
2.88	40	5	1.0396E+07	1.5019E+07	1.1706E+07	2.0151E+07	8.913E+06	1.424E+07	1.976E+07	7.475E+07	0.1427	0.0519	0.6884	2.7094	14.27	5.19	68.84	270.94
2.9	40	15	1.0550E+07	1.5112E+07	1.1752E+07	2.0108E+07	8.920E+06	1.426E+07	1.519E+07	7.168E+07	0.1545	0.0565	0.2923	2.5645	15.45	5.65	29.23	256.45
3.22	40	15	1.3180E+07	1.6591E+07	1.2478E+07	1.9473E+07	9.063E+06	1.451E+07	1.531E+07	7.208E+07	0.3124	0.1256	0.2266	2.7017	31.24	12.56	22.66	270.17
3.22	40	0	1.3180E+07	1.6591E+07	1.2478E+07	1.9473E+07	8.975E+06	1.433E+07	1.955E+07	7.148E+07	0.3190	0.1364	0.5670	2.6707	31.90	13.64	56.70	267.07
2.9	60	10	1.3353E+07	2.0713E+07	1.6357E+07	3.1942E+07	1.229E+07	1.970E+07	2.171E+07	9.541E+07	0.0795	0.0488	0.3271	1.9870	7.95	4.88	32.71	198.70
3.22	60	10	1.6682E+07	2.2740E+07	1.7368E+07	3.0933E+07	1.252E+07	2.013E+07	2.215E+07	9.659E+07	0.2493	0.1149	0.2752	2.1225	24.93	11.49	27.52	212.25
3.22	60	15	1.6682E+07	2.2740E+07	1.7368E+07	3.0933E+07	1.252E+07	2.014E+07	1.700E+07	9.301E+07	0.2494	0.1141	0.0214	2.0068	24.94	11.41	2.14	200.68
2.88	60	0	1.3158E+07	2.0585E+07	1.6293E+07	3.2010E+07	1.227E+07	1.963E+07	2.710E+07	9.242E+07	0.0672	0.0465	0.6631	1.8871	6.72	4.65	66.31	188.71
2.75	80	10	1.4098E+07	2.4706E+07	2.0063E+07	4.5086E+07	1.544E+07	2.481E+07	2.306E+07	1.160E+08	0.0953	0.0040	0.1494	1.5738	9.53	0.40	14.94	157.38
3.05	80	10	1.7570E+07	2.7096E+07	2.1288E+07	4.3677E+07	1.572E+07	2.526E+07	2.411E+07	1.178E+08	0.1051	0.0677	0.1324	1.6960	10.51	6.77	13.24	169.60
3.22	80	15	1.9719E+07	2.8439E+07	2.1960E+07	4.2957E+07	1.590E+07	2.561E+07	1.479E+07	1.116E+08	0.1936	0.0996	0.3264	1.5973	19.36	9.96	32.64	159.73
2.88	80	0	1.5553E+07	2.5745E+07	2.0600E+07	4.4452E+07	1.545E+07	2.468E+07	3.332E+07	1.127E+08	0.0069	0.0415	0.6174	1.5343	0.69	4.15	61.74	153.43

	Segment 1	Segment 2	Segment 3	Nozzle
x	0.2966	0.5306	0.1420	0.0566
y	1.9902	0.6804	0.5689	-0.1678
z	-0.2015	-0.0099	0.2598	0.4783

$$\Delta\dot{q} = x \cdot OF^y \cdot PCC^z$$

$\Delta\dot{q}_{regression}$ | $\dot{q} = \Delta\dot{q}_{regression} \cdot \dot{q}_{Thermtest}$ | $error = \dfrac{|\dot{q} - \dot{q}_{correlation}|}{\dot{q}_{correlation}} \cdot 100$ | Standard deviation of experimental values

OF [-]	PCC [bar]	μ [%]	QAK1 [W/m²]	QAK2 [W/m²]	QAK3 [W/m²]	QAD [W/m²]	QAK1 [W/m²]	QAK2 [W/m²]	QAK3 [W/m²]	QAD [W/m²]	QAK1 [%]	QAK2 [%]	QAK3 [%]	QAD [%]	QAK1 [%]	QAK2 [%]	QAK3 [%]	QAD [%]
2.88	20	10	1.3314E+00	1.0578E+00	5.6422E-01	1.9866E-01	6.9653E+06	8.8139E+06	6.6974E+06	9.3584E+06	0.24	0.59	0.68	2.45	2.00	0.40	2.00	0.50
3.07	20	20	1.5120E+00	1.1048E+00	5.8511E-01	1.9655E-01	7.9637E+06	9.2757E+06	5.4486E+06	8.8338E+06	0.05	0.00	21.03	1.38	1.70	0.60	12.30	9.30
3.41	20	20	1.8635E+00	1.1866E+00	6.2113E-01	1.9311E-01	1.2357E+07	1.2557E+07	5.8463E+06	8.8401E+06	24.17	23.27	20.21	1.92	1.70	0.60	12.30	9.30
3.22	20	0	1.6625E+00	1.1412E+00	6.0120E-01	1.9498E-01	8.8026E+06	9.6426E+06	7.0905E+06	8.6528E+06	0.08	0.37	0.00	1.98	2.50	1.60	2.00	10.20
2.88	40	5	1.1578E+00	1.0505E+00	6.7554E-01	2.7675E-01	1.0319E+07	1.4960E+07	1.3351E+07	2.0686E+07	0.73	0.39	14.05	2.66	2.90	1.20	7.10	10.70
2.9	40	15	1.1739E+00	1.0555E+00	6.7820E-01	2.7643E-01	1.0471E+07	1.5050E+07	1.0301E+07	1.9813E+07	0.75	0.41	12.35	1.47	1.50	1.10	12.00	14.40
3.22	40	15	1.4458E+00	1.1334E+00	7.1981E-01	2.7162E-01	1.3103E+07	1.6442E+07	1.1018E+07	1.9579E+07	0.59	0.90	11.71	0.55	1.50	1.10	12.00	14.40
3.22	40	0	1.4458E+00	1.1334E+00	7.1981E-01	2.7162E-01	1.2976E+07	1.6240E+07	1.4075E+07	1.9415E+07	1.55	2.11	12.79	0.30	4.10	1.70	1.00	20.10
2.9	60	10	1.0818E+00	1.0513E+00	7.5353E-01	3.3559E-01	1.3297E+07	2.0712E+07	1.6357E+07	3.2019E+07	0.42	0.00	0.00	0.24	2.80	2.10	3.30	11.10
3.22	60	10	1.3323E+00	1.1289E+00	7.9976E-01	3.2975E-01	1.6686E+07	2.2720E+07	1.7713E+07	3.1850E+07	0.02	0.08	1.99	2.96	2.80	2.10	3.30	11.10
3.22	60	15	1.3323E+00	1.1289E+00	7.9976E-01	3.2975E-01	1.6682E+07	2.2740E+07	1.3593E+07	3.0670E+07	0.00	0.00	21.73	0.85	5.20	0.30	3.40	3.60
2.88	60	0	1.0670E+00	1.0463E+00	7.5057E-01	3.3598E-01	1.3096E+07	2.0538E+07	2.0338E+07	3.1050E+07	0.47	0.23	24.83	3.00	6.80	4.30	4.40	15.80
2.75	80	10	9.1846E-01	1.0110E+00	7.8783E-01	3.8854E-01	1.4182E+07	2.5079E+07	1.8168E+07	4.5086E+07	0.60	1.51	9.44	0.00	1.50	1.40	6.40	11.80
3.05	80	10	1.1286E+00	1.0848E+00	8.3563E-01	3.8184E-01	1.7746E+07	2.7405E+07	2.0144E+07	4.4964E+07	1.00	1.14	5.38	2.95	1.50	1.40	6.40	11.80
3.22	80	15	1.2573E+00	1.1256E+00	8.6182E-01	3.7839E-01	1.9991E+07	2.8825E+07	1.2748E+07	4.2217E+07	1.38	1.35	41.95	1.72	3.30	1.90	8.40	9.10
2.88	80	0	1.0069E+00	1.0433E+00	8.0881E-01	3.8554E-01	1.5552E+07	2.5746E+07	2.6948E+07	4.3433E+07	0.00	0.00	30.82	2.29	6.70	2.20	2.90	10.80
		Sum									32.06	32.38	228.98	26.71				

Mokry

Factors		Segment 1	Segment 2	Segment 3	Nozzle
	a	128469.503	332159.890	315499.222	413545.713
	b	2.127	0.892	0.573	-0.307
	c	0.581	0.777	0.815	1.141

$$\dot{q}_{correlation} = a \cdot OF^b \cdot PCC^c$$

Correlation · $\dot{q}_{Thermtest}$ · $\Delta\dot{q} = \dfrac{|\dot{q}_{Thermtest} - \dot{q}_{correlation}|}{\dot{q}_{correlation}}$ · Deviation (%)

OF [-]	PCC [bar]	μ [%]	QAK1 [W/m²]	QAK2 [W/m²]	QAK3 [W/m²]	QAD [W/m²]	QAK1 [W/m²]	QAK2 [W/m²]	QAK3 [W/m²]	QAD [W/m²]	ΔQAK1 [W/m²]	ΔQAK2 [W/m²]	ΔQAK3 [W/m²]	ΔQAD [W/m²]	ΔQAK1 [%]	ΔQAK2 [%]	ΔQAK3 [%]	ΔQAD [%]
2.88	20	10	6.9486E+06	8.7619E+06	6.6518E+06	9.1346E+06	4.825E+06	8.344E+06	1.139E+07	4.381E+07	0.3057	0.0477	0.7119	3.7962	30.57	4.77	71.19	379.62
3.07	20	20	7.9597E+06	9.2757E+06	6.8997E+06	8.9574E+06	4.713E+06	8.200E+06	9.474E+06	4.230E+07	0.4080	0.1160	0.3731	3.7227	40.80	11.60	37.31	372.27
3.41	20	20	9.9519E+06	1.0187E+07	7.3274E+06	8.6736E+06	5.412E+06	9.195E+06	9.304E+06	4.195E+07	0.4562	0.0974	0.2697	3.8364	45.62	9.74	26.97	383.64
3.22	20	0	8.8096E+06	9.6788E+06	7.0908E+06	8.8274E+06	4.617E+06	8.159E+06	1.113E+07	4.057E+07	0.4760	0.1571	0.5691	3.5964	47.60	15.71	56.91	359.64
2.88	40	5	1.0396E+07	1.5019E+07	1.1706E+07	2.0151E+07	7.921E+06	1.337E+07	1.869E+07	6.859E+07	0.2380	0.1095	0.5965	2.4039	23.80	10.95	59.65	240.39
2.9	40	15	1.0550E+07	1.5112E+07	1.1752E+07	2.0108E+07	7.902E+06	1.335E+07	1.511E+07	6.648E+07	0.2510	0.1164	0.2856	2.3061	25.10	11.64	28.56	230.61
3.22	40	15	1.3180E+07	1.6591E+07	1.2478E+07	1.9473E+07	7.673E+06	1.297E+07	1.478E+07	6.636E+07	0.4179	0.2184	0.1842	2.4078	41.79	21.84	18.42	240.78
3.22	40	0	1.3180E+07	1.6591E+07	1.2478E+07	1.9473E+07	7.413E+06	1.227E+07	1.718E+07	6.441E+07	0.4375	0.2605	0.3766	2.3074	43.75	26.05	37.66	230.74
2.9	60	10	1.3353E+07	2.0713E+07	1.6357E+07	3.1942E+07	1.107E+07	1.835E+07	2.287E+07	8.862E+07	0.1711	0.1139	0.3982	1.7744	17.11	11.39	39.82	177.44
3.22	60	10	1.6682E+07	2.2740E+07	1.7368E+07	3.0933E+07	1.068E+07	1.774E+07	2.233E+07	8.895E+07	0.3600	0.2200	0.2856	1.8755	36.00	22.00	28.56	187.55
3.22	60	15	1.6682E+07	2.2740E+07	1.7368E+07	3.0933E+07	1.066E+07	1.776E+07	1.816E+07	8.662E+07	0.3608	0.2191	0.0458	1.8002	36.08	21.91	4.58	180.02
2.88	60	0	1.3158E+07	2.0585E+07	1.6293E+07	3.2010E+07	1.108E+07	1.831E+07	2.685E+07	8.584E+07	0.1581	0.1107	0.6480	1.6816	15.81	11.07	64.80	168.16
2.75	80	10	1.4098E+07	2.4706E+07	2.0063E+07	4.5086E+07	1.494E+07	2.553E+07	2.795E+07	1.092E+08	0.0594	0.0335	0.3932	1.4216	5.94	3.35	39.32	142.16
3.05	80	10	1.7570E+07	2.7096E+07	2.1288E+07	4.3677E+07	1.438E+07	2.459E+07	2.713E+07	1.100E+08	0.1817	0.0927	0.2742	1.5185	18.17	9.27	27.42	151.85
3.22	80	15	1.9719E+07	2.8439E+07	2.1960E+07	4.2957E+07	1.408E+07	2.416E+07	1.788E+07	1.056E+08	0.2858	0.1506	0.1856	1.4581	28.58	15.06	18.56	145.81
2.88	80	0	1.5553E+07	2.5745E+07	2.0600E+07	4.4452E+07	1.422E+07	2.436E+07	3.301E+07	1.047E+08	0.0859	0.0538	0.6026	1.3553	8.59	5.38	60.26	135.53

x	0.3090	0.4707	0.1340	0.0792
y	2.0941	0.7291	0.9036	-0.3370
z	-0.2122	0.0240	0.1734	0.4584

$$\Delta\dot{q} = x \cdot OF^y \cdot PCC^z$$

$\Delta\dot{q}_{regression}$ · $\dot{q} = \Delta\dot{q}_{regression} \cdot \dot{q}_{Thermtest}$ · $error = \dfrac{|\dot{q} - \dot{q}_{correlation}|}{\dot{q}_{correlation}} \cdot 100$ · Standard deviation of experimental values

OF [-]	PCC [bar]	μ [%]	QAK1 [W/m²]	QAK2 [W/m²]	QAK3 [W/m²]	QAD [W/m²]	QAK1 [W/m²]	QAK2 [W/m²]	QAK3 [W/m²]	QAD [W/m²]	QAK1 [%]	QAK2 [%]	QAK3 [%]	QAD [%]	QAK1 [%]	QAK2 [%]	QAK3 [%]	QAD [%]
2.88	20	10	1.4997E+00	1.0936E+00	5.8591E-01	2.1888E-01	7.2355E+06	9.1252E+06	6.6721E+06	9.5894E+06	4.13	4.15	0.30	4.98	2.00	0.40	2.00	0.50
3.07	20	20	1.7144E+00	1.1458E+00	6.2073E-01	2.1422E-01	8.0790E+06	9.3950E+06	5.8810E+06	9.0622E+06	1.50	1.29	14.76	1.17	1.70	0.60	12.30	9.30
3.41	20	20	2.1361E+00	1.2370E+00	6.8253E-01	2.0677E-01	1.1560E+07	1.1373E+07	6.3502E+06	8.6736E+06	16.16	11.65	13.34	0.00	1.70	0.60	12.30	9.30
3.22	20	0	1.8945E+00	1.1863E+00	6.4807E-01	2.1080E-01	8.7459E+06	9.6788E+06	7.2106E+06	8.5530E+06	0.72	0.00	1.69	3.11	2.50	1.60	2.00	10.20
2.88	40	5	1.2946E+00	1.1120E+00	6.6075E-01	3.0074E-01	1.0254E+07	1.4872E+07	1.2348E+07	2.0628E+07	1.36	0.98	5.49	2.37	2.90	1.20	7.10	10.70
2.9	40	15	1.3135E+00	1.1176E+00	6.6489E-01	3.0004E-01	1.0379E+07	1.4923E+07	1.0046E+07	1.9946E+07	1.62	1.26	14.52	0.80	1.50	1.10	12.00	14.40
3.22	40	15	1.6354E+00	1.2062E+00	7.3085E-01	2.8964E-01	1.2548E+07	1.5641E+07	1.0799E+07	1.9221E+07	4.80	5.73	13.45	1.30	1.50	1.10	12.00	14.40
3.22	40	0	1.6354E+00	1.2062E+00	7.3085E-01	2.8964E-01	1.2123E+07	1.4799E+07	1.2555E+07	1.8655E+07	8.02	10.80	0.61	4.20	4.10	1.70	1.00	20.10
2.9	60	10	1.2052E+00	1.1285E+00	7.1333E-01	3.6133E-01	1.3339E+07	2.0713E+07	1.6314E+07	3.2020E+07	0.11	0.00	0.26	0.24	2.80	2.10	3.30	11.10
3.22	60	10	1.5006E+00	1.2180E+00	7.8409E-01	3.4880E-01	1.6021E+07	2.1602E+07	1.7507E+07	3.1026E+07	3.97	5.00	0.80	0.30	2.80	2.10	3.30	11.10
3.22	60	15	1.5006E+00	1.2180E+00	7.8409E-01	3.4880E-01	1.6002E+07	2.1629E+07	1.4242E+07	3.0213E+07	4.08	4.89	18.00	2.33	5.20	0.30	3.40	3.60
2.88	60	0	1.1879E+00	1.1228E+00	7.0888E-01	3.6217E-01	1.3158E+07	2.0555E+07	1.9034E+07	3.1088E+07	0.00	0.15	16.82	2.88	6.80	4.30	4.40	15.80
2.75	80	10	1.0145E+00	1.0931E+00	7.1469E-01	4.1970E-01	1.5152E+07	2.7913E+07	1.9976E+07	4.5823E+07	7.47	12.98	0.43	1.64	1.50	1.40	6.40	11.80
3.05	80	10	1.2601E+00	1.1789E+00	7.8478E-01	4.0531E-01	1.8118E+07	2.8983E+07	2.1288E+07	4.4585E+07	3.12	6.96	0.00	2.08	1.50	1.40	6.40	11.80
3.22	80	15	1.4117E+00	1.2264E+00	8.2420E-01	3.9797E-01	1.9880E+07	2.9624E+07	1.4739E+07	4.2024E+07	0.82	4.17	32.88	2.17	3.30	1.90	8.40	9.10
2.88	80	0	1.1175E+00	1.1306E+00	7.4515E-01	4.1322E-01	1.5887E+07	2.7541E+07	2.4601E+07	4.3264E+07	2.15	6.97	19.42	2.67	6.70	2.20	2.90	10.80
Sum											60.02	76.96	152.79	32.24				

Bibliography

[1] R. Arnold, D.I. Suslov, and O. J. Haidn. Experimental investigation of film cooling with tangential slot injection in a LOX/CH4 subscale rocket combustion chamber. *Transactions of the Japan society for aeronautical and space sciences, space technology Japan*, Vol. 1:81–86, 2008.

[2] R. Arnold, D.I. Suslov, and O. J. Haidn. Circumferential film cooling effectiveness in a LOX/H2 subscale combustion chamber. *Journal of propulsion and power*, Vol. 25:760–770, 2009.

[3] R. Arnold, D.I. Suslov, and O. J. Haidn. Film cooling of accelerated flow in a subscale combustion chamber. *Journal of propulsion and power*, Vol. 25:443–451, 2009.

[4] R. Arnold, D.I. Suslov, and O. J. Haidn. Film cooling in a high-pressure subscale combustion chamber. *Journal of propulsion and power*, Vol. 26:428–438, 2010.

[5] D. R. Bartz. An approximate solution of compressible turbulent boundary layer development and convective heat transfer in convergent divergent nozzles. *Trans. ASME*, Vol. 7:549–568, 1955.

[6] D. R. Bartz. A simple equation for rapid estimation of rocket nozzle convective heat transfer coefficients. *Jet Propulsion*, Vol. 27(1):49–51, 1957.

[7] M. E. Crawford, W. M. Kays, and R. J. Moffat. Full-coverage film cooling on flat, isothermal surfaces: a summary report on data and predictions. *NASA CR 3219*, 1980.

[8] L. T. De Luca. *Problemi energetici in propulsione aerospaziale*. SPLab, 2007.

[9] R. G. Deissler and A. L. Loeffler, Jr. Analysis of turbulent flow and heat transfer on a flat plane at high Mach numbers with variable fluid properties. *NACA Technical Note 4262*, 1959.

[10] R. L. Ewen and H. M. Evensen. Liquid rocket engine self-cooled combustion chamber. *NASA space vehicle design criteria (chemical propulsion)*, NASA SP-8124, 1977.

[11] R. A. Gater and M. R. L'Ecuyer. A fundamental investigation on the phenomena that characterize liquid-film cooling. *TM-69-1, Jet Propulsion Center Purdue University*, Vol. 13:1925–1928, 1969.

[12] R. J. Goldstein and A. Haji-Sheikh. Prediction of film cooling effectiveness. *JSME: Proceedings of 1967 semi-international symposium*, Vol. 47:213–218, 1967.

[13] A. R. Grahm. An experimental and theoretical investigation of film cooling of rocket motors. *Rept. F 57-3, Purdue University, Lafayette, Indiana*, 1957.

[14] W. M. Grissom. Liquid film cooling in rocket engines. *Defence technical information center (DTIC)*, AEDC-TR-91-1:74, 1991.

[15] P. A. Haberlen, D. A. Greisen, and W. E. Anderson. A film cooling model for a RP-1/GOX staged combustion liquid rocket engine. *Journal of propulsion and power*, page 31, 2007.

[16] O. J. Haidn. Advanced rocket engines. *Advances on propulsion technology for high-speed aircraft*, RTO-EN-AVT-150:1–40, 2008. http://www.rto.nato.int.

[17] J. E. Hatch and S. S. Papell. Use of a theoretical flow model to correlate data for film cooling or heating an adiabatic wall by tangential injection of gases of different fluid properties. *NASA Technical Note D-130*, page 43, 1959.

[18] J. R. Howell and S. H. Lee. Convective heat transfer in the entrance region of a vertical tube for water near the thermodynamic critical point. *International journal of heat and mass transfer*, Vol. 42:1177–1187, 1999.

[19] D. K. Huzel and D. H. Huang. Design of liquid propellant rocket engines. *NASA SP-125, Scientific and thechnical information division*, page 460, 1971.

[20] IAPWS. Revised supplementary release on saturation properties of ordinary water substance. 1992. http://www.iapws.org.

[21] IAPWS. IAPWS release on surface tension of ordinary water substance. 1994. http://www.iapws.org.

[22] IAPWS. Uncertainties in enthalpy for the IAPWS formulation 1995 for the thermodynamic properties of ordinary water substance for general and scientific use (IAPWS-95) and the IAPWS industrial formulation 1997 for the thermodynamic properties of water and steam (IAPWS-IF97). 2003. http://www.iapws.org.

[23] IAPWS. Revised release on the IAPWS industrial formulation 1997 for the thermodynamic properties of water and steam. 2007. http://www.iapws.org.

[24] W. M. Kays. *Convective heat and mass transfer (1st Ed).* New York: McGraw-Hill, 1966.

[25] C. Kirchberger. ATTLAS Deliverable D4.1.10 - Final report: heat transfer characterization with video data analysis. 2009.

[26] C. Kirchberger, A. Hupfer, H. P. Kau, S. Soller, P. Martin, M. Bouchez, and E. Dufour. Improved prediction of heat transfer in a rocket combustor for GOX/Kerosene. *AIAA-2009-1214, 47th AIAA Aerospace Sciences Meeting and Exhibit, Orlando, FL, USA*, 2009.

[27] C. Kirchberger, G. Schlieben, A. Hupfer, H. P. Kau, and S. Soller. Film cooling investigations in a Kerosene/GOX combustion chamber. *JPC: 2011*, 2011.

[28] C. Kirchberger, R. Wagner, Prof. H. P. Kau, S. Soller, P. Martin, M. Bouchez, and C. Bonzom. Prediction and analysis of heat transfer in small rocket chambers. *AIAA-2008-1260, 46th AIAA Aerospace Sciences Meeting and Exhibit,Reno, USA*, 2008.

[29] J. Klein and M. Tribus. Forced convection fron nonisothermal surfaces. page 18, 1952.

[30] R. C. Krueger and A. N. Curren. Some factors influencing heat transfer to liquid propellant rocket thrust chamber coolant channels. *NASA TN D-3671*, 1966.

[31] J. G. Lucas and R. L. Golladay. Gaseous film cooling of a rocket motor with injection near the throat. *NASA TN D-3836*, 1967.

[32] D. Marty. *Conception des véhicules spatiaux.* Masson, 1985.

[33] B. J. McBride and S. Gordon. Computer program for calculation of complex chemical equilibrium compositions and applications. *NASA Reference Publication 1311*, 1996.

[34] S. Mokry, A. Farah, K. King, S. Gupta, I. Pioro, and P. Kirillov. Development of supercritical water heat-transfer correlation for vertical bare tubes. *Proceedings of the Nuclear Energy for New Europe 2009 international conference, 14 - 17 September 2009*, 2009.

[35] A. J. Pavli, J. K. Curley, P. A. Masters, and R. M. S. Design and cooling performance of a dump cooled rocket engine. *NASA TN D-3532*, 1966.

[36] I. Pioro and S. Mokry. Heat transfer to fluids at supercritical pressures. *Heat Transfer - Theoretical Analysis, Experimental, Investigations and Industrial Systems*, Vol. 241:1126–1136, 2011.

[37] M. Rachner. Die Stoffeigenschaften von Kerosin Jet A-1. *DGLR Mitteilung 98-01*, 1998.

[38] R. L. Schacht and R. J. Quentmeyer. Axial and circumferential variations of hot gas side heat transfer rates in a hydrogen-oxigen rocket. *NASA TN D-6396*, 1971.

[39] G. Schlieben and C. Kirchberger. Test plan for cold flow characterization of baseline film applicator - Transregio SFB-TR40 - Deliverable number K1.1.1. 2009.

[40] G. Schlieben, C. Kirchberger, and O. J. Haidn. JPC 2012 - Using intra cooling channel measurements for film cooling investigations in a GOX/Kerosene rocket combustion chamber. *AIAA JPC 2012*, 2012.

[41] G. Schlieben, C. Kirchberger, H. P. Kau, C. Höglauer, and O. Knab. Film cooling investigations within a GOX/Kerosene combustion chamber. *EUCASS-2011*, 2011.

[42] G. Schmidt. Technik der Flüssigkeits-Raketentriebwerke. *Daimler Chrisler Aerospace Münich*, 1999.

[43] L. Schoenmann. Hydrogen-Oxygen auxiliary propulsion for the Space Shuttle. Vol. 1: high pressure thrusters. *NASA CR-120895, Aerojet Liquid Rocket Co.*, 1972.

[44] T. R. Shembharkar and B. R. Pai. Prediction of film cooling with a liquid coolant. *International journal of heat and mass transfer*, Vol. 29:899–908, 1985.

[45] M. Sliphorst. Simple models for heat transfer esimation in rocket engine combustion chambers. Master's thesis, Technische Universiteit Delft, 2004.

[46] R. C. Stechman, J. Oberstone, and J. C. Howell. Film cooling design criteria for small rocket engines. *AIAA 4th Propulsion Joint Specialist Conference*, AIAA Paper 68-617:17, 1968.

[47] R. C. Stechman, J. Oberstone, and J. C. Howell. Design criteria for film cooling for small liquid-propellant rocket engines. *Journal of Spacecraft and Rocket*, Vol. 6:97–102, 1969.

[48] J. E. Terry and G. J. Caras. Transpiration and film cooling of liquid rocket nozzles. *RSIC-535*, 1966.

[49] W. Wagner and A. Pruss. The IAPWS formulation 1995 for the thermodynamic properties of ordinary water substance for general and scientific use. *J. Phys. Chem*, Vol. 31:387–535, 2002. http://www.iapws.org.

[50] B. Weigand, J. R. Ferguson, and M. E. Crawford. An extended Kays and Crawford turbulent Prandtl number model. *Journal of heat and mass transfer*, Vol. 40:4191–4196, 1997.

[51] Y. C. Yu, R. Z. Schuff, and W. E. Anderson. Liquid film cooling using swirl in rocket combustor. *40th AIAA Joint Propulsion Conference and Exhibit*, AIAA 2004-3360, 2004.

[52] H. Ziebland and R. C. Parkinson. Heat transfer in rocket engines. *AGARD-AG-148-71*, AGARDograph No. 148, 1971.